
**Università degli Studi di Firenze**

Facoltà di Scienze Matematiche, Fisiche e Naturali
Dottorato in Scienze Chimiche
(XXI Ciclo)

Settore disciplinare: CHIM-02

# Laser Tissue Welding: Study of the Mechanism and Optimization of the Technique

**Paolo Matteini**

Tutore: Prof. Andrea Goti

Co-Tutore: Dr. Roberto Pini

Coordinatore: Prof. Gianni Cardini

# Table of Contents

# SUMMARY

Lasers have become already a widespread tool in many operative and therapeutic applications in the surgical field. Minimally invasive laser techniques provide remarkable improvements in respect with conventional methods. The aim of these techniques is to improve the quality of life of patients, by decreasing healing times and the risk of postoperative complications. Since its first application in the seventies, laser tissue welding has been proposed and tested in several experimental models including blood vessels, skin, nerve, intestine, uterine tube and so on. Laser welding has progressively assumed increased relevance in the clinical setting, where it appears to be a valid alternative to standard surgical techniques.

Although laser tissue welding has been experimentally demonstrated on a large variety of tissues and by the use of different lasers, several aspects of its application remain to be elucidated. Firstly, the mechanism of laser welding - poorly understood up to these days - represents the first crucial question to be clarified. In fact, the development of a successful laser welding protocol is strictly dependent on the precise understanding of its biophysical and biochemical bases. Another poorly solved question is the ability to monitor semi-quantitatively the structural changes induced in the tissue during the laser application. This is of utmost importance in assessing the quality of surgical intervention and in preventing undesiderable thermal damage to the peripheral structures. Lastly, with the advent of nanotechnology, new classes of nanostructured chromophores are attracting much attention in view of several biomedical applications. Speaking of laser welding, the efficiency of these nano-chromophores to mediating the welding process once activated by laser light is an intriguing matter which remains to be investigated.

During my PhD work I examined some of these aspects focusing the attention, in particular, on the application of laser welding to ocular tissues. The study of the mechanism

of laser tissue welding was studied either from microscopic and chemical prospectives. The results pointed out a reorganization of the extracellular components of the tissue, among which proteoglycans were found to play a primary role. The question of the optimization of the laser welding technique was handled following a twofold route. The first relied on the setup of noninvasive imaging systems to examine the photothermal modifications induced in the tissue. The second was devoted to assess the effectiveness of new nanochromophores in assisting the laser welding technique.

This thesis is organized in three different parts. The first one (Chapter 1) is aimed at giving a short introduction on the laser tissue welding technique, with particular attention to laser welding of the ocular tissues. In Chapter 2 the work carried out in order to clarify the mechanism of laser welding of corneal tissue is presented. The last part (Chapters 3 and 4) has been devoted to propose new imaging methodologies for monitoring laser-induced modifications in the tissue and to explore the possibility of improving the laser welding technique by the use of gold nanoparticles as new chromophores.

# 1. INTRODUCTION

*This chapter firstly (§1.1) introduces the concept of laser tissue welding of biological tissues giving a brief description of the advantages offered by this technique with respect to traditional suturing of tissue. Then (§1.2), the attention is focused on laser welding applied to the ocular tissues. Diode laser technique and its application to the closure of corneal and lens capsule wounds is finally presented.*

## 1.1 - BACKGROUND

*This is a brief introduction aimed at presenting the laser welding technique. The advantages offered by this method as well as the main problems encountered with the early laser welding approaches, including the poor control of the dosimetry of laser irradiation and the lack of specificity are discussed. Then the innovative laser welding techniques, based on the use of exogenous chromophores, solders and photosensitizers are introduced.*

### 1.1.1 Laser welding technique

Lasers have become already a widespread tool in many operative and therapeutic applications in the surgical field. Minimally invasive laser techniques provide remarkable improvements: in these, laser surgery is performed inside the human body through small incisions by means of optical fibre probes and endoscopes, or laser tools are proposed as a replacement for conventional tools in order to minimize the surgical trauma, such as in the case of laser-induced suturing of biological tissues. The aim of these procedures is to

improve the quality of life of patients, by decreasing healing times and the risk of postoperative complications.

Joining tissue by applying laser irradiation was first reported at the end of the 1970s, when a neodymium:yttrium-aluminium-garnet (Nd:YAG) laser was used for the microvascular anastomosis of rat carotid and femoral arteries. Ever since, laser tissue welding has been evaluated in several experimental models including blood vessels, skin, nerve, intestine, uterine tube and so on [1, 2]. Laser welding has progressively assumed increased relevance in the clinical setting, where it appears to be a valid alternative to standard surgical techniques. At present there are many applications of tissue welding that are beginning to achieve widespread acceptance.

Many types of lasers have been proposed for laser tissue welding. Infrared and near-infrared sources include carbon dioxide ($CO_2$), thulium-holmium-chromium, holmium, thulium, and neodymium rare-earth-doped-garnets (THC:YAG, Ho:YAG, Tm:YAG, and Nd:YAG, respectively), and gallium aluminium arsenide diode (GaAlAs) lasers. Visible sources include potassium-titanyl phosphate (KTP) frequency-doubled Nd:YAG, and argon lasers. The laser energy is absorbed by water at the infrared wavelengths and by hemoglobin and melanin at the visible wavelengths, thereby producing heat within the target tissue. As the temperature rises, cellular and extracellular matrices of the connective tissue undergo thermal changes that lead to the welding of the wound.

Laser tissue welding has been shown to possess several advantages compared to conventional closure methods, such as reduced operation times, fewer skill requirements, decreased foreign-body reaction and therefore reduced inflammatory response, faster healing, increased ability to induce regeneration and an improved cosmetic appearance. Laser welding also has the potential to form complete closures, thus making possible an immediate watertight anastomosis which is particularly important in the case of vascular, genito-urinary tract and gastrointestinal repairs. Lastly, laser welding can be used endoscopically and laparoscopically to extend the range of its applications to cases in which sutures or staples cannot be used.

However, despite the large number of experimental studies reported in the literature, very few of them have reached the clinical phase. This is mainly because of the lack of clear evidence of the advantages of laser-assisted suturing against conventional methods, and because of a low reproducibility of results. The damage induced in tissues by direct laser heating and heat diffusion and the poor strength of the resulting welding are the main problems as far as future clinical applications of the laser-assisted procedure are concerned. In fact, since water, hemoglobin and melanin are the main absorbers of laser light within

tissue, the heating effect is not selectively limited to a target area, and all irradiated tissues are heated. For instance, the $CO_2$ laser has been used for laser repairs of thin tissues because of its short penetration depth (< 20 μm). However, for thicker tissues, welding has been achieved only by irradiating with high laser power and longer exposure times, thus inducing high levels of heat damage [3]. The emissions of other near-infrared lasers, such as Nd:YAG and diode lasers, are more suited to the welding of thicker tissues. In any case the control of the dosimetry of laser irradiation and of corresponding temperature rise is often a matter of concern with these methods, which frequently have been responsible of heat damage and lack of strong welds [1,2].

### 1.1.2 Laser welding with chromophores and solders

Two advances have been useful in addressing the issues associated with laser tissue welding: the application of laser-wavelength-specific chromophores and the addition of endogenous and exogenous material to be used as solder.

The use of wavelength-specific chromophores enables differential absorption between the stained region and the surrounding tissue. The advantage is primarily a selective absorption of laser radiation by the target, without the need for a precise focusing of the laser beam. Moreover, lower laser irradiances can be used because of the increased absorption of stained tissues. Various chromophores have been employed as laser absorbers, including indocyanine green (ICG) [4], fluorescein [5], basic fuchsin and fen 6 [6]. The use of a near-infrared laser - which is poorly absorbed by biological tissues -, in conjunction with the topical application of a dye with an absorption peak overlapping the laser emission, is a very popular setting for the laser welding technique. Diode lasers emitting around 800 nm and ICG have been used in corneal tissue welding in cataract surgery and corneal transplant [7, 8], vascular tissue welding [9, 10, 11], skin welding [4, 12] and in laryngotracheal mucosa transplant [13].

Laser welding by means of solders, namely “laser soldering", makes use of exogenous solders as topical protein preparations. This makes possible a bonding of the adjoining and underlying tissues when activated by laser light. The extrinsic agents provide a large surface area over which fusion with the tissue can occur, thus favoring the approximation of the wound edges that eventually heal together in the postoperative period. Useful welding materials include blood [14], plasma [15], fibrinogen [16] and albumin, which is the one most frequently employed [5, 17]. Several studies have demonstrated that the addition of an albumin solder to reinforce laser tissue repairs significantly improves postoperative results [5, 18]. Moreover, incorporation into the protein solder of a laser-absorbing chromophore makes it possible to confine the heat into the area of solder application, which reduces the

extent of collateral heat damage to adjacent tissues. ICG-doped albumin has become an increasingly popular choice in the last decade [17]. The laser is used to denature the protein immediately after application of the protein solder to the wound site, thus yielding a bond at the solder / tissue interface.

### 1.1.3 Photochemical welding

Photochemical welding of tissues has also been investigated as an alternative method for tissue repair without direct use of heat. This technique utilizes chemical cross-linking agents applied to the cut that, when light-activated, produce covalent cross-links between collagen fibres of the native tissue structure. Agents used for photochemical welding include 1,8-naphthalimide [19], Rose Bengal, riboflavin-5-phosphate, fluorescein and methylene blue [20]. Studies of photochemical tissue bonding have been conducted for articular cartilage bonding [19], cornea repair [20], skin graft adhesion [21] and for repairing severed tendons [22].

## 1.2 - LASER WELDING IN OPHTHALMOLOGY

*This section gives a brief overview of laser welding in ophthalmology. Then the diode laser technique is presented along with its main applications in the closure of corneal and capsular wounds.*

The first attempt to join biological tissues were proposed in ophthalmology, for the treatment of retinal, corneal and scleral samples [23, 24, 25]. The first studies were unsuccessful, resulting in no tissue fusion, while with the improvement of laser technique several research groups adopted different approaches in order to induce welding of scleral and corneal tissue. Retina fusion was achieved by inducing photocoagulation of the tissue, while the technique used to treat other ocular tissues is based on a soft thermal treatment, properly defined as laser welding. Successful experimental studies of laser-induced suturing of ocular tissues on animal models have been reported since 1992 by different authors [26, 27, 28, 29, 30, 31, 32] based on the use of near- and far-infrared lasers, directly absorbed by the water content of the cornea. Various laser types with wavelengths exhibiting high optical absorption in water have been used, such as $CO_2$ (emitting at 10.6 $\mu$m) [30, 31, 32], Erbium:YAG (1455 nm) [26] and diode lasers (1900 nm) [28, 29]. The main problem with such laser wavelengths is that, without an adequate control of the laser dosimetry, the direct absorption of laser light in a short penetration depth of the tissue outer portion caused a high temperature rise at the irradiated surface, followed by collagen shrinkage and denaturation; on the contrary the deeper layers are hardly heated at all, resulting in a weak bonding, since the full thickness of the tissue is not involved in the welding process. Improved results in tissue welding were observed by using exogenous chromophores to absorb laser light, sometimes in association with protein solders. Addition of highly absorbing dyes can allow fusion of wounds at lower irradiation fluences, thus avoiding excessive thermal damage to surrounding tissues. In fact, the usage of a chromophore induces a controllable temperature rise only in the area where it had been previously applied, resulting in a selective thermal effect.

In this regards, a new approach was proposed and tested for the closure of corneal wounds [8, 33, 34, 35] and for the treatment of anterior lens capsule bags [36]. It is based on the use of a near-infrared (NIR) diode laser, in association with the topical application of a NIR absorbing chromophores (ICG). The welding procedure, which was optimized so that it could be used in ophthalmic surgery applications, has been proposed as a valid alternative to

the traditional suturing technique used for the closure of corneal wounds, such as in cataract surgery, in penetrating keratoplasty (i.e. transplant of the cornea), and in the treatment of accidental corneal perforations. It can also be used for closure of the lens capsule (to repair capsular breaks caused by accidental traumas or produced intraoperatively), as well as to provide closure of the capsulorhexis in lens refilling procedures. A description of the technique and its applications is given in the following paragraph.

### 1.2.1- Laser welding of the cornea with diode laser technique

#### 1.2.1.1 Notes on the morphology of the cornea

The cornea is an avascularized connective tissue on the outer surface of the eye, and forms the outer shell of the eyeball together with the sclera (**Fig 1.1**). It acts as one of the main refractive components, assuring good vision with its clarity and shape. It also acts as a mechanical barrier and as a biological defense system. The cornea is composed of different layers: epithelium, stroma and endothelium are the principal ones, proceeding from the external surface towards the inner part of the eye.

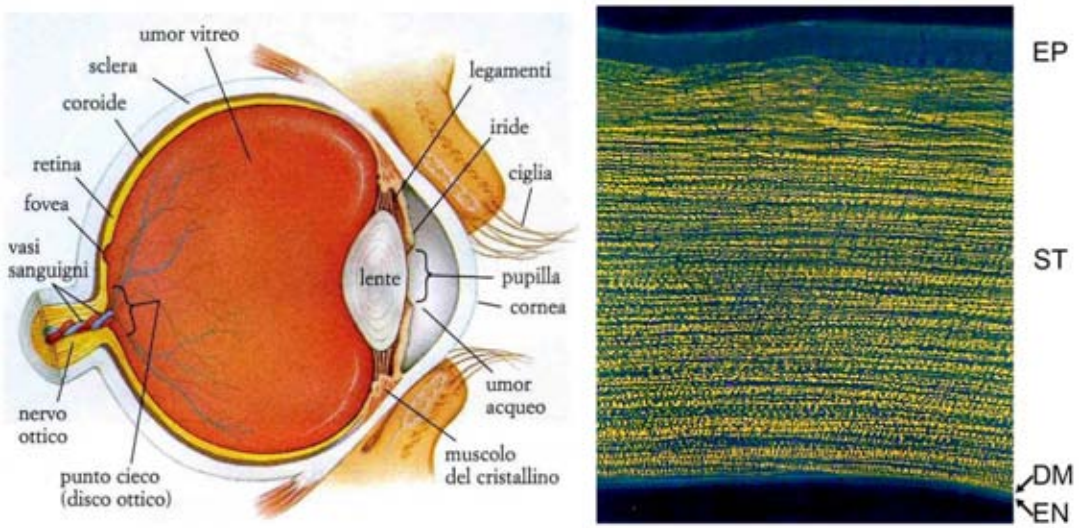


**Fig 1.1** (left) Structure of the eye. (right) Polarized microscopy image of a human cornea section: from the external surface (top) towards the inner part of the eye, the various layers can be identified: EP epithelium, ST stroma, DM Descemet's membrane and EN endothelium. The Picrosirius Red/Alcian Blue stain provides a very clear view of the horizontally oriented stromal lamellae.

More than 90 % of the cornea is stroma, and consists of extracellular matrices (mainly type I collagen and proteoglycans), keratocytes and nerve fibres. The collagen is regularly arranged in fibres, thus contributing to corneal transparency; the collagen fibres are organized in lamellae, i.e. in planes running parallel to the corneal surface. These particular structures and architecture confer unique properties to corneal tissue, e.g. in the reaction

process to external injuries, such as incidental traumas, surgical incisions or ulcers. The injured tissues heal by repair and do not recover the “normal" configuration, because of an induced disorganization in the ordered array of the collagen fibres. This results in an opaque scar with less tensile strength than that of an unwounded cornea, and in a subsequent impairment of the main corneal functions. Moreover, the healing of corneal stroma is slower than that of other connective tissues because of the lack of blood vessels. Clinical changes in scar formation may, in fact, be detected years after surgery has taken place [56].

#### 1.2.1.2 Diode laser welding of the cornea

For all these reasons, the characteristics of laser welding procedures may be very useful in practical surgery, offering the possibility of avoiding many post-operative complications. A laser-welding technique has been recently proposed (**Fig. 1.2**) by the Biophotonic Group of the “Istituto di Fisica Applicata ‘Nello Carrara’” of the National Research Council for welding corneal tissue [7, 8, 33, 34, 35].

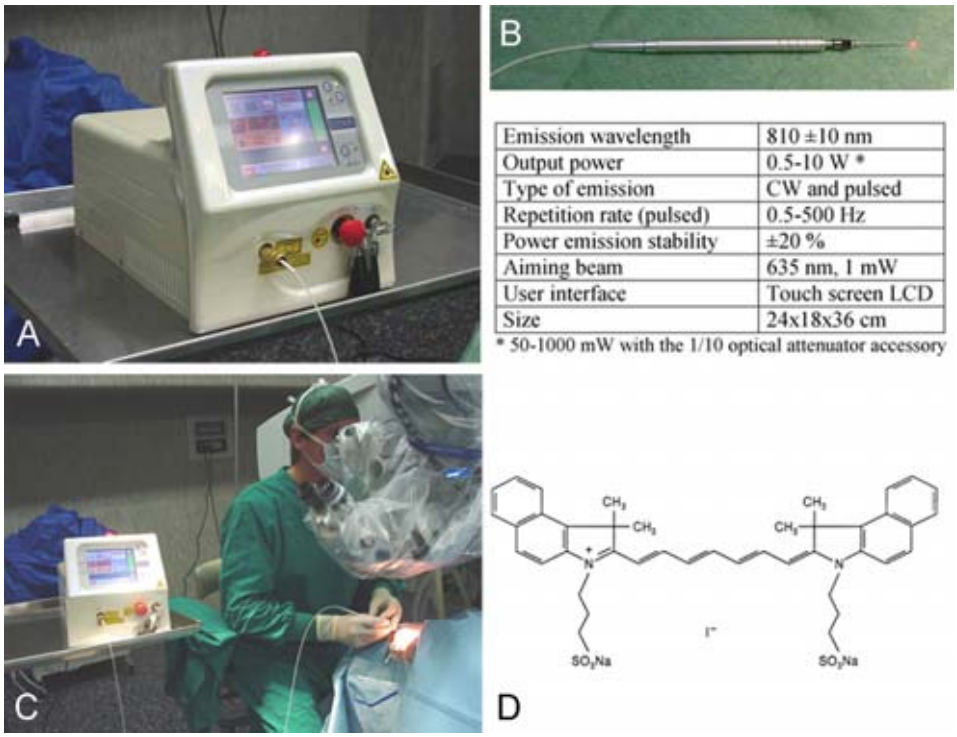


**Fig. 1.2** (A) AlGaAs diode laser emitting at 810 nm (Mod. WELD 800, El.En., Italy); (B) Hand piece to be used under surgical microscope; (C) Diode laser at work during a surgical corneal transplant at AUSL 4 – Unità oculistica, Ospedale di Prato; (D) Structural formula of Indocyanine Green (ICG).

It has been tested and optimized on animal models: experimental analyses were firstly performed on *ex vivo* pig eyes; the healing process was then studied *in vivo* in rabbits. The technique was then proposed clinically and is currently being used for the closure of corneal tissue after penetrating keratoplasty, instead of a continuous suturing. The main advantages

of this clinical practice are an increased patient comfort during the healing process and a reduction of hospitalization costs. The immediate watertight closure of wound edges provides protection from external inflammation, and may prevent endophthalmitis, which sometimes occurs after cataract surgery. The position of the apposed margins has been found to be stable in time, thus assuring optimal results in terms of postoperative induced astigmatism after cataract and keratoplasty surgery [35]. The absence of stitches does not induce foreign body reaction, thus improving the healing process. Histological analyses performed on animals and morphological observations on treated patients have shown that, in a laser-welded wound, tissue regains an architecture similar to that of the intact tissue, thus supporting its main functions (clarity and good mechanical load resistance) (**Fig. 1.3**).

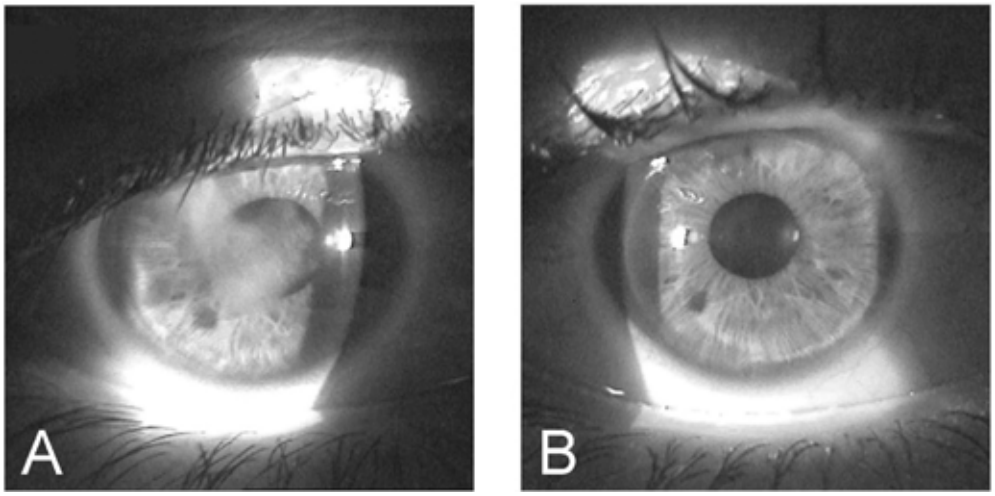


**Fig 1.3** Aspect of human cornea affected by leucoma (A): before surgery, and (B): three days after corneal transplant.

The technique is based on the use of near-infrared continuous-wave AlGaAs diode laser radiation emitting at 810 nm, in association with the topical application of a sterile water solution (10 % weight/weight) of ICG to the corneal wound to be repaired. This dye is characterized by high optical absorption around 800 nm [37], while the stroma is almost transparent at this wavelength. ICG is a frequently-used ophthalmic dye, with a history of safety in humans. It is being used increasingly as an intraocular tissue stain in cataract and vitreoretinal surgery, as well as in staining of the retinal internal limiting membrane [38, 39, 40]. Furthermore, ICG is commonly used as a chromophore in laser welding or laser soldering [1], in order to induce differential absorption between the dyed region and the surrounding tissue. Photothermal activation of stromal collagen is thus induced by laser radiation only in the presence of ICG, resulting in a selective welding effect, which produces an immediate sealing of the wound edges and good mechanical strength. In addition, with the use of ICG, very low laser power is required (below 100 mW), and this

generally means much safer operation with respect to the use of other laser types without the association of dyes.

The procedure used to weld human corneal tissue is as follows: the chromophore solution is placed inside the corneal cut, using an anterior chamber cannula, in an attempt to stain the walls of the cut in depth. A bubble of air is injected into the anterior chamber prior to the application of the staining solution, so as to avoid perfusion of the dye. A few minutes after application, the solution is washed out with abundant water. Lastly, the whole length of the cut is subjected to laser treatment. Laser energy is transferred to the tissue in a non-contact configuration, through a 300-$\mu$m core diameter fibre optic terminating in a hand piece, which enables easy handling under a surgical microscope. A typical value of the laser energy density is about 13 W/cm$^2$ in humans, which results in a good welding effect. During irradiation, the fibre tip is kept at a working distance of about 1 mm, and at a small angle with respect to the corneal surface (side irradiation technique). This particular position provides in-depth homogenous irradiation of the wound and prevents from accidental irradiation of deeper ocular structures. The fibre tip is continuously moved over the tissue to be welded, with an overall laser irradiation time of about 120 s for a 25-mm cut length (the typical perimeter of a transplanted corneal button).

A follow up study on animal models [7] and clinical application of the technique provided evidence that laser-welded tissues exhibits good adhesion and good mechanical resistance. A thorough study of the healing process - based on morphological observations, standard histology, and multi-spectral imaging autofluorescence microscopy [41] - proved experimentally that this takes place in shorter time and with lower inflammatory reaction, when compared to conventionally sutured wounds. Objective observations two weeks after surgery showed a good morphology of laser-treated corneas, with almost restored cuts, generally characterized by better adhesion and less edematous appearance compared to sutured ones. These features were confirmed by means of histological examinations of rabbit corneas, which revealed a well-developed repair process involving the epithelium, which almost regained its physiological continuity and thickness and a partially re-organized architecture of the stroma. Histological analyses on longer follow-up times indicated that the healing of laser-welded wounds was completed in about 30 - 60 days, while in sutured wounds the healing process was still in progress (**Fig. 1.4**). This result is particularly important as far as corneal tissue is concerned, as it typically requires much longer times to be repaired than do other types of tissue. Furthermore, the restored tissue regains a stromal architecture that is very close to the native one, which is crucial to regaining of correct vision.

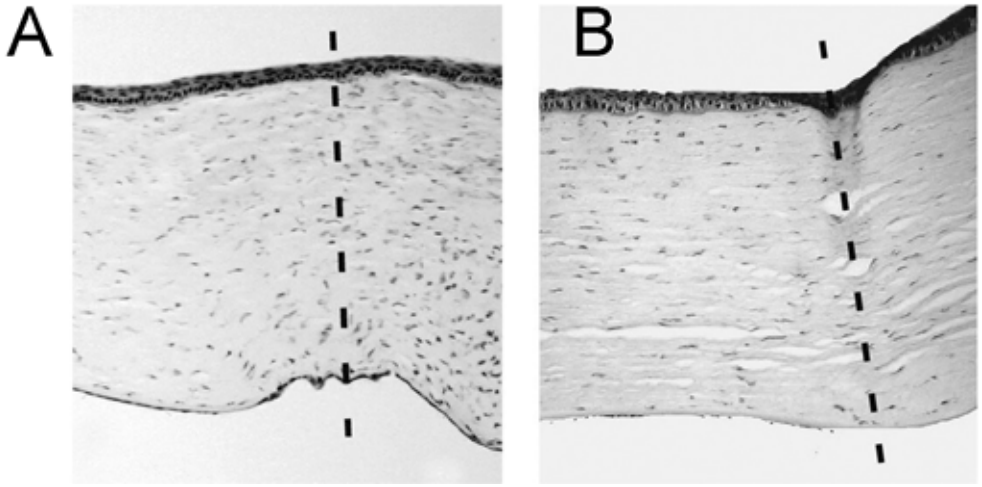


**Fig. 1.4** Histological section of rabbit corneal tissue on postoperative day 30 (Hematoxilin/Eosin, x50); after laser welding (A): the architecture of the cornea regained an almost physiological appearance (the original cut is indicated by the dashed line); after conventional stay suturing (B): the cut is still clearly detectable and large lacunae are evident in the corneal stroma [7].

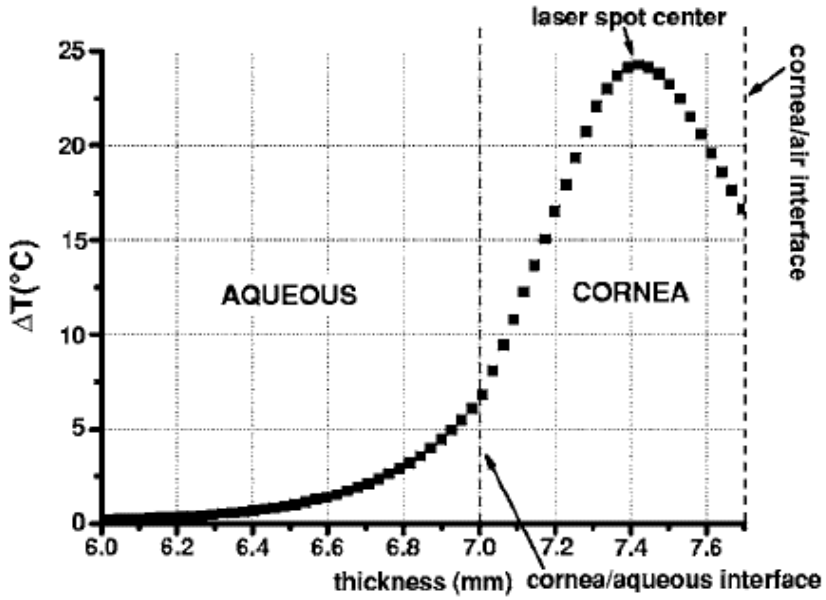


**Fig. 1.5** Temperature rise distribution along radial distance from the center of the eye toward external ambient air. These calculated data refer to 12.5 W/cm$^2$ laser power density and 2 s treatment time. The ΔT maximum value is inside the cornea, in correspondence with the laser spot center. For a mean temperature of 35 °C in the living cornea, the maximum temperature peak due to photothermal interaction is in the 59 °C to 66 °C range, as calculated inside the stained wound for the operative irradiation parameters which give the best welding results in clinical procedures [42].

Experimental analyses with an IR thermo-camera provided information on the heating of the external surface of the irradiated tissues and on heat confinement during the treatment [42]. A partial differential equation modeling of the process allowed to investigate the

temperature dynamics inside the tissue. From this study it was possible to point out that the optimal welding temperature is about 60 °C inside the treated wound (**Fig. 1.5**).

### 1.2.3 Laser closure of capsular tissue with the diode laser welding technique

#### 1.2.3.1 Notes on the lens capsule morphology

The lens, or crystalline lens, is a transparent, biconvex structure in the eye: after the cornea, it is the second refractive component in the eye. The lens is flexible and its curvature is controlled by ciliary muscles through the zonules. It is included within the capsular bag, maintained by the zonules of Zinn, which are filament structures connected to the ciliary muscles fulfilling lens accommodation (i.e. focusing of light rays into the retina in order to assure good vision). This capsule is a very thin (about 10 $\mu$m thick [43]), transparent acellular membrane that maintains the shape of the lens. This tissue is a collagenous meshwork mainly composed of type IV collagen and other non collagenous components such as laminin and fibronectin. Type I and type III collagen are also present [44].

#### 1.2.3.2 Diode laser welding of the lens capsule

The function of the lens capsule is primarily mechanical: in the accommodation process it has load-transmitting function. With ageing, the lens loses its ability to accommodate, thus requiring cataract surgery, which consists of replacing the native lens with a non-accommodating plastic prosthetic one. The ultimate goal of this surgery is ideally the restoration of the accommodative function by refilling the capsular bag with an artificial polymer [45], after the endocapsular aspiration of nuclear and cortical material. This technique may become a viable lens-replacing procedure, as soon as experimental tests are able to prove preservation of capsular mechanical functions and clarity of refilled lens. Moreover, it would be important for the feasibility of this technique, to demonstrate that a biocompatible valve on the anterior lens capsule tissue could be set up to facilitate lens-refilling operations.

In order to improve cataract surgery, thus providing a surgical solution to presbyopia, it has been proposed a solution for performing a flap valve with the use of a patch of capsular tissue obtained from a donor lens, to be laser-welded onto the recipient capsule. The procedure may also be used to repair accidental traumas, such as capsular breaks or perforations during intraocular lenses implantation [46]. Due to its particular fragility and elasticity, it is quite impossible to suture capsular tissue using standard techniques; however, at present there are no alternative methods. Laser welding could be used in order to accomplish this goal. The study is in progress, and preliminary evidence of the feasibility of this technique has recently been obtained [36, 46]. Experimental tests were carried out *ex*

*vivo*, on freshly enucleated porcine eyes. Closure tests were performed by means of patches of donor capsulae (mean diameter: 3 mm). The inner side of the patch was stained with an ICG-saturated solution in sterile water (7 % weight/weight). The staining solution was left in place for 5 minutes. The sample was then washed with abundant water, in order to remove any excess of ICG. The stained patch was then applied to the anterior lens capsule, through a previously performed corneal incision. The stained inner side of the patches were positioned on the exterior surface of the recipient capsule, so as to maintain the original orientation and curvature. This procedure facilitated adhesion between the tissues to be welded. The patch was then irradiated along its external perimeter by means of contiguous laser spots emitted by a 200-$\mu$m-core fiber, whose tip was gently pressed onto the patch surface (contact welding technique) (**Fig. 1.6a**).

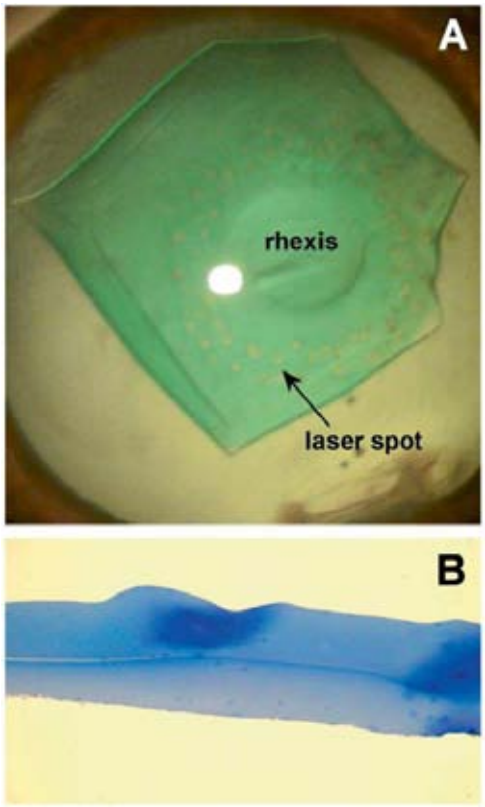


**Fig 1.6** (A) Appearance of a capsulorhexis in a pig eye, that was closed by applying an ICG-stained capsular patch subjected to PLW; laser spots are clearly evident at the periphery of the patch. (B) Histological slice of an anterior capsular patch (20 μm thick) laser-welded onto the anterior lens capsule of a pig eye. Effective adhesion between the two samples was accomplished with minimal heat damage (Methylene Blue staining) [36].

Exposure times were found to be critical in order to avoid heat damage. Continuous wave irradiation, which is typically employed in other laser welding applications, was unsuitable, while pulses around 100 ms (with energies of 30 - 50 mJ) provided the best results. Once welded, the capsular patch showed good adhesion to the recipient anterior

capsular surface. Preliminary biomechanical tests performed on laser-welded anterior capsule flaps showed that the load resistance of welded specimens was comparable to that of healthy tissues. Standard histology analysis indicated good adhesion between the apposed samples and thermal damage localized in the treated area (**Fig. 1.6B**).

## References


1. K. M. McNally: Laser tissue welding. Chap. 39. In: Biomedical Photonics Handbook, ed by T. Vo-Dihn (CRC Press, Boca Raton, 2003) pp 1–45
2. R. Pini, F. Rossi et al.: Laser tissue welding in minimally invasive surgery and microsurgery. Chap. 15. In: Biophotonics. Series: Biological and Medical Physics, Biomedical Engineering, ed by L. Pavesi and P.M. Fauchet (Springer-Verlag, Berlin, Heidelberg, 2008) pp 275-299
3. G. E. Kopchok, R. A. White, G. H. White, et al.: Lasers Surg. Med. 8, 584 (1988)
4. S. D. DeCoste, W. Farinelli, T. Flotte, et al.: Lasers Surg. Med. 12, 25 (1992)
5. D. P. Poppas and D. S. Scherr: Haemophilia 4, 456 (1998)
6. S. G. Brooks, S. Ashley, H. Wright, et al.: Lasers Med. Sci. 6, 399 (1991)
7. F. Rossi, R. Pini, L. Menabuoni, et al.: J.Biomed. Opt. 10, 024004 (2005)
8. R. Pini, L. Menabuoni and L. Starnotti: Proc. SPIE 4244, 266 (2001)
9. R. A. White, G. E. Kopchok, C. E. Donayre, et al.: Lasers Surg. Med. 8, 83 (1988)
10. B. Ott, B. J. Zuger, D. Erni, et al.: Lasers Med. Sci. 16, 260 (2001)
11. A. Puca, A. Albanese, G. Esposito, et al.: Neurosurgery 59, 1286 (2006)
12. C. Chiarugi, L. Martini, L. Borgognoni, et al.: Proc. SPIE 2623, 407 (1996)
13. Z. Wang, M. M. Pankratov, L. L. Gleich, et al.: Arch. Otolaryngol. Head Neck Surg. 121, 773 (1995)
14. S. Wang, P.E. Grubbs, S. Basu, et al.: Microsurgery 9, 10 (1988)
15. D. F. Cikrit, M. C. Dalsing, T. S. Weinstein, et al.: Lasers Surg. Med. 10, 584 (1990)
16. S. K. Forman, M. C. Oz, J. F. Lontz, et al.: Clin. Orthop. Relat. Res. 310, 37 (1995)
17. K. M. McNally, B. S. Sorg, A. J. Welch, et al.: Phys. Med. Biol. 44, 983 (1999)
18. A. J. Kirsch, C. S. Cooper, J. Gatti, et al.: J.Urol. 165, 574 (2001)
19. M. M. Judy, R. W. Jackson, H. R. Nosir, et al.: Proc. SPIE 2970, 257 (1997)
20. L. Mulroy, J. Kim, I. Wu, et al.: Invest. Ophthalmol. Vis. Sci. 41, 3335 (2000)
21. B. P. Chan, I. E. Kochevar and R. W. Redmond: J. Surg. Res. 108, 77 (2002)
22. B. P. Chan, C. Amann, A. N. Yaroslavsky, et al.: J. Surg. Res. 124, 274 (2005)
23. H. C. Zweng and M. Flocks: Tran. Am. Acad. Ophthalmol. Otolaryngol. 71, 39 (1967)
24. R. H. Keates, S. N. Levy, S. Fried, et al.: J. Cataract Refract. Surg. 13, 290 (1987)
25. R. P. Gailitis, K. P. Thompson, Q. S. Ren, et al.: Refract. Corneal Surg. 6, 430 (1990)
26. H. E. Savage, R. K. Halder, U. Kartazayeu, et al.: Lasers Surg. Med. 35, 293 (2004)
27. N. L. Burnstein, J. M. Williams, M. J. Nowicki, et al.: Arch. Ophthalmol. 110, 12 (1992)
28. T. J. Desmettre, S. R. Mordon and V. Mitchell: Proc. SPIE 2623, 372 (1996)
29. G. Trabucchi, P. G. Gobbi, R. Brancato, et al.: Proc. SPIE 2623, 380 (1996)
30. A. Barak, O. Eyal, M. Rosner, et al.: Surv. Ophthalmol. 42, S77 (1997)
31. E. Strassmann, N. Loya, D. D. Gaton, et al.: Proc. SPIE 4244, 253 (2001)
32. E. Strassmann, N. Loya, D. D. Gaton, et al.: Proc. SPIE 4609, 222 (2002)
33. L. Menabuoni, B. Dragoni and R. Pini: Proc. SPIE 2922, 449 (1996)
34. L. Menabuoni, F. Mincione, B. Dragoni, et al.: Proc. SPIE 3195, 25 (1998)
35. L. Menabuoni, R. Pini, F. Rossi, et al.: to be published in J. Cataract Refract. Surg. (2007)
36. R. Pini, F. Rossi, L. Menabuoni, et al.: Proc. SPIE 6138, 307 (2006)
37. M. L. J. Landsman, G. Kwant, G. A. Mook, et al.: J. Appl. Physiol. 40, 575 (1976)
38. L. A. Yannuzzi, M. D. Ober, J. S. Slakter, et al.: Am. J. Ophthalmol. 137, 511 (2004)
39. G. P. Holley, A. Alam, A. Kiri, et al.: J. Cataract Refract. Surg. 28, 1027 (2002)
40. T. John: J. Cataract Refract. Surg. 29, 437 (2003)
41. R. Pini, V. Basile, S. Ambrosini, et al.: Proc. SPIE 6138, 404 (2006)
42. F. Rossi, R. Pini and L. Menabuoni: J. Biomed. Opt. 12, 014031 (2007)
43. N.M. Ziebarth, F. Manns, S.R. Uhlhorn, et al.: Invest. Ophthalmol. Vis. Sci. 46, 1690 (2005)
44. C.C. Danielsen: Exp. Eye Res. 79, 343 (2004)
45. E. Haefliger and J-M. Parel: Exp. Eye Res. 10, 550 (1994)
46. R. Pini, F. Rossi, et al.: Ophthalmic Surg. Lasers Imaging 39, 260 (2008)

# 2. STUDY OF THE MECHANISM OF LASER WELDING

*In this chapter we first (§2.1) give a brief overview of the most significative literature studies that have dealt with the mechanism of laser tissue welding. The second (§2.2) and the third (§2.3) sections are devoted to the work we carried out to clarify the mechanism of diode laser welding of the cornea. In the former section we report on the microscopic analyses we performed on laser-welded corneal tissue according to a typical surgical procedure. The latter section (§2.3) focuses on the chemical analyses which we carried out on a model molecule (hyaluronan) in order to investigate the involvement of proteoglycans in the mechanism of diode laser welding.*

## 2.1 - STATE OF THE ART

*In this section we review the state of the art with regard to the problem of interpreting the mechanism of laser tissue welding, as it is available in the published literature. In particular, the main studies dealing with laser welding proper (i.e. without solders but including or not staining with chromophores) and with other laser welding techniques (i.e. laser soldering and laser photochemical welding) are discussed.*

As far as the mechanism of tissue welding by means of laser light is concerned, a first distinction must be made between: 1) laser tissue welding, 2) laser tissue soldering, and 3) photochemical tissue bonding. For all these three cases, the exact underlying mechanism is

not fully understood. Conversely, several hypotheses do exist, which are based on a limited number of electron and optical microscopy observations and on some *in vitro* studies.

### 2.1.1 Laser welding

Although laser tissue welding has been experimentally demonstrated on a large variety of tissues and by the use of different lasers, its biophysical and biochemical basis remains still unclear. However, the development of a successful welding protocol is strictly dependent on the precise understanding and control of the welding molecular mechanism. Moreover it is worth noting the interplay between laser-induced changes in tissue structure and the wound healing process taking place during the postoperative course.

In general, when induced by solely laser irradiation, laser welding is regarded as purely photothermal process [1]: laser light induces structural modifications in the main components of the extracellular matrix of connective tissue, which generate connection bridges between the apposed edges of the wound to be laser-welded.

Collagen is the most abundant protein in vertebrate connective tissues constituting from 15 to 80 % of the dry weight depending on tissue type. More than 20 different types of collagens have been described in vertebrates (**Fig. 2.1**). Despite the difference among collagens, they are all based on a triple-helical domain consisting of three left-handed α-helices interconnected by stabilizing hydrogen bonds.

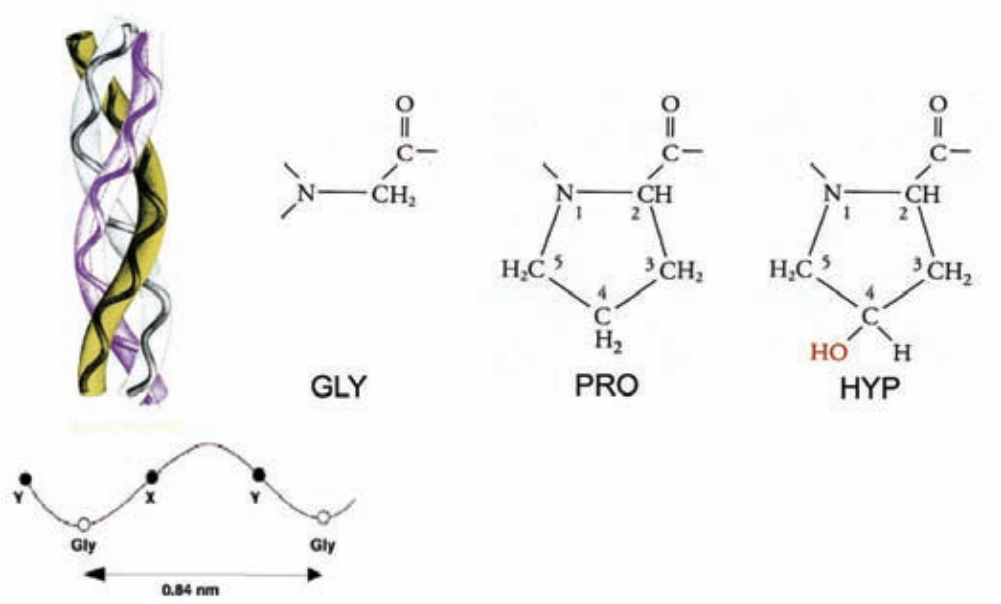


**Fig. 2.1** Collagen molecule is a triple-helix based on three left-handed α-helices which are characterized by the typical aminoacid sequence Gly-X-Y where X, Y are mainly Proline and Hydroxyproline.

Within the collagen family, the fibril-forming collagens are major components of all mammalian connective tissues, providing the structural and organizational framework for skin, blood vessels, bone, tendon, cornea and other tissues. In this type of collagens, molecules are packed in a quarter-staggered manner (**Fig. 2.2**) and connected by covalent bonds to form a collagen fibril. When heat is applied, unwinding of the triple helices occurs due to hydrolysis of the intramolecular hydrogens (**Fig. 2.3**). This is the first step of collagen denaturation process which leads to tissue shortening due to a shrinkage effect parallel to the axis of the fibril [2]. At higher temperatures covalent cross-links connecting collagen strands break, resulting in a complete destruction of the fibrillar structure and causing relaxation of the tissue [3]. The onset value of collagen shrinkage often quoted in the clinical literature is around 60 °C, while relaxation is reported to occur beyond 75 °C.

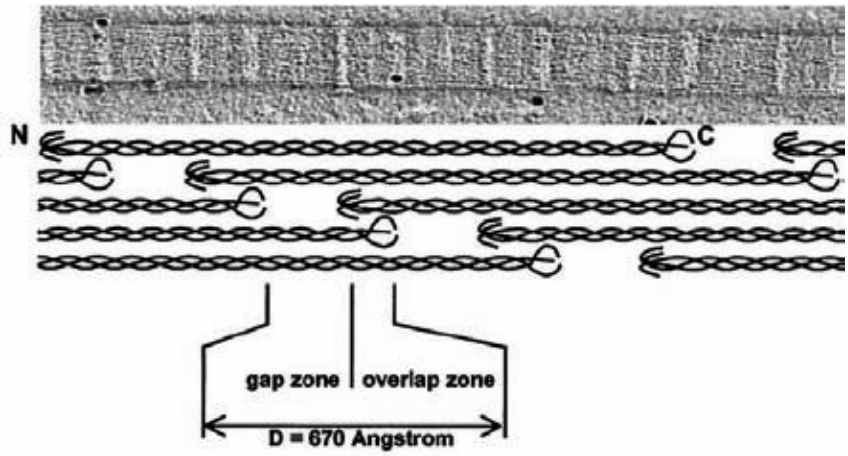


**Fig. 2.2** Collagen triple helices are axially staggered by the period D (67 nm) and regularly organized in the lateral direction. The D-periodicity is easily detected by electron microscope (e.g. see the cross-striation imaged by SEM in the upper part of the image).

However, it is worth noting that collagen denaturation is a rate process governed by the local temperature/time response [4]: thus the time/temperature history influences the shrinkage threshold of collagen, as well as the relaxation phase. Moreover, either the temperature for maximum shrinkage and the relaxation temperature depend on the cross-links density which rises on tissue ageing, and on hydroxyproline content which varies among species and tissues [5].

To date, the laser-induced morphological alterations of collagen molecules have been believed to play a primary role in the laser welding mechanism, leading to the observed tensile strength after laser application [6]. This belief has mainly originated from microscopic observations of laser-welded biological tissue. The microscopic data reported

in the literature on laser-welded tissues can be schematically split into two groups on the basis of different modifications of the collagen matrix observed upon laser welding.

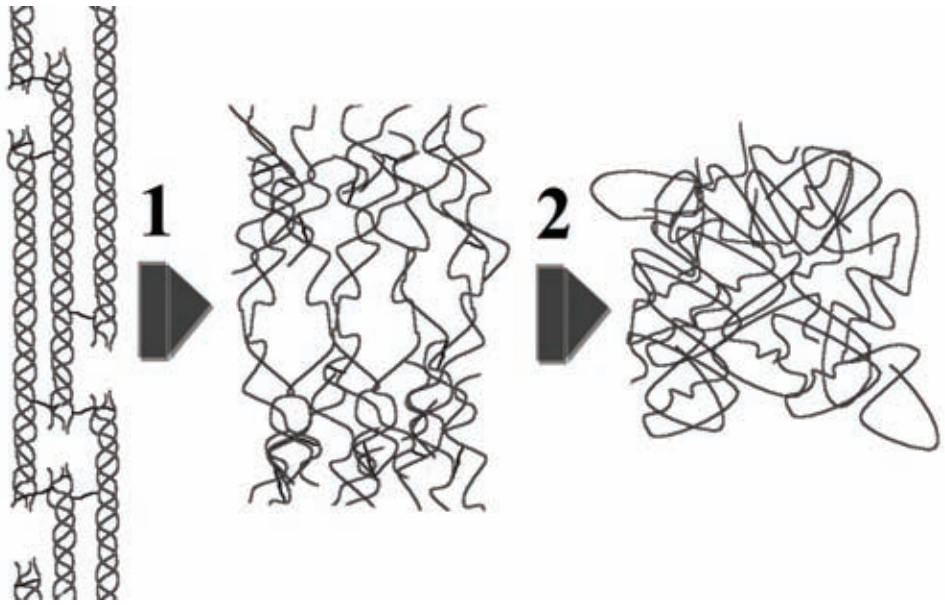


**Fig. 2.3** Structural modifications induced in fibrillar collagen of connective tissue by temperature rise. Normal triple helix collagen molecules are packed in a quarter staggered manner and connected by covalent bonds to form a collagen fibril (*left*). When heat is applied, hydrolysis of intramolecular hydrogen bonds occurs, which results in the unwinding of the triple helices (*middle*). The first step (1) leads to a shrinkage effect parallel to the axis of the fibrils. At higher temperatures, covalent cross-links connecting collagen strands break, resulting in a complete destruction of the fibrillar structure (*right*) and causing relaxation of the tissue (step 2).

The first common observation is a loss of collagen periodicity and increased fibril calibre with associated splitting into fine subfibrillar structures [6, 7] (**Fig. 2.4**). In this case triple helix unwinding probably occurs, leading to partial denaturation of fibrillar collagen. The most common interpretation of the working mechanism is an unraveling of collagen fibers at the cut ends, followed by interdigitation of the fibers across the cut [7]. The result is a fusion either between the cut ends of collagen fibers, either between their parallel face. It is supposed that new chemical bonds are generated upon laser irradiation: while some researchers have proved the generation of new covalent cross-links at the weld site [8], others have suggested the formation of non-covalent interactions between unwound collagen strands on both sides of the weld [9]. Operative temperature values in the 60-65 °C range have been estimated at the weld area [9]. A secondary role of fibrillar type I collagen in the laser welding mechanism has been pointed out in a recent study [10], suggesting the involvement of some other extracellular matrix components, and being in agreement with earlier studies on welded tissue extracts analyzed by gel-electrophoresis [11, 12].

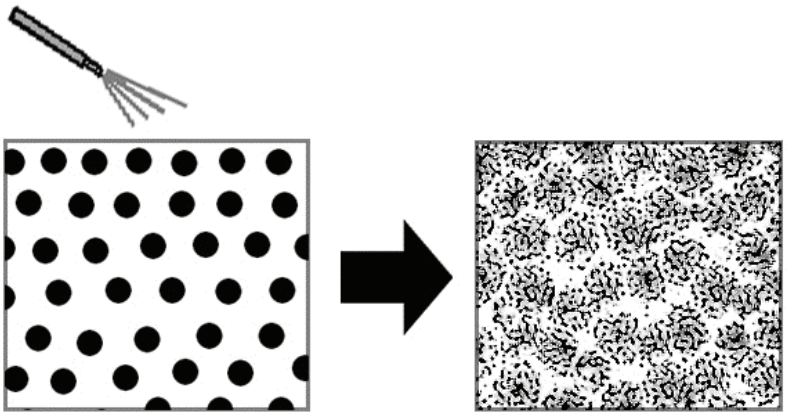

**Fig. 2.4** "Mild" laser welding resulting in a partial modification of the tissue morphology. The extracellular matrix is schematically represented by an array of *black dots* simulating cross-sectioned collagen fibrils embedded in the ground substance, as in a typical connective tissue (*left* ). Native connective tissue subjected to laser irradiation is characterized by collagen fibrils still recognizable and partially swollen (*right*). Temperature values in the range 60–65°C are usually induced at the weld site. The main welding mechanism hypothesized is based on "interdigitation" upon cooling between collagen fibres unraveled by laser heat.

Another common observation of welded samples is the full homogenization of the tissue (also called hyalinosis), in which the loose structure of the collagen fibrils was lost following laser welding [6, 13, 14, 15]. In this context, fibrils fused together and morphologically altered revealed a complete denaturation of the collagen matrix [16, 17] (**Fig. 2.5**).

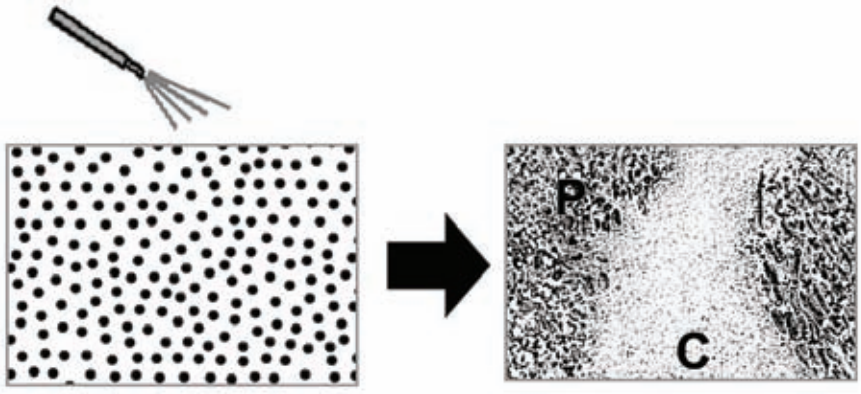


**Fig. 2.5** "Hard" laser welding resulting in a complete homogenization of the tissue. Laser irradiation leads to hardly recognizable collagen structures completely (C) or partially (P) coagulated (*right*). Temperatures above 75°C are usually recorded in these cases. The mechanism proposed relies on the adhesion upon cooling between proteins denatured by laser heat, which, acting as microsolders, seal the wound.

Moreover, cell membranes are also disrupted causing leakage of the cellular proteins. In these cases, operative temperatures of over 75 °C were induced at the welded area [18]. Denatured collagen and intracellular proteins are supposed to photocoagulate thus acting as endogenous glue (micro-solders) and forming new molecular bonds upon cooling [15].

### 2.1.2 Other techniques: laser soldering and photochemical welding

Photothermal soldering relies on the coagulation of a protein solder by means of a laser-induced temperature increase in the tissue. Upon cooling, non-covalent interactions between the solder and the collagen matrix within the tissue are supposed to be responsible for the strength of the weld. Evidence of albumin intertwining within the collagen matrix was found during scanning electron microscopy analyses of specimens irradiated at temperatures above 70 °C [19]. Such a threshold value is fully in agreement with the threshold temperature of albumin coagulation (around 65 °C), as reported in several spectroscopic and calorimetric studies. Evidence of extracellular matrix infiltration of solder within the tissue was also found by using standard histological analysis [14, 20].

In photochemical tissue bonding, photosensitive dyes applied to the wound edges behave as reactive species when irradiated by laser light. They react with potential electron donors and acceptors such as amino acids (e.g. tryptophan, tyrosine, cysteine) of proteins. Strong covalent bonds are produced between the approximated surfaces of the wound, forming instantaneous protein cross-links [21]. The formation of cross-links in collagen type I molecules by means of photochemical activation has been confirmed by using gel electrophoresis [22].

## References


1. S. A. Prahl, and S. D. Pearson.: Proc. SPIE 2975, 245 (1997)
2. J. C. Allain, M. Le Lous, et al.: Conn. Tissue Res. 7, 127 (1980)
3. M. Le Lous, F. Flandin, et al.: Biochim. Biophys. Acta 717, 295 (1982)
4. R. Brinkmann, B. Radt, et al.: J. Cataract Refract. Surg. 26, 744(2000)
5. A. J. Bailey, R. G. Paul and L. Knott: Mech. Ageing Develop. 106, 1 (1998)
6. J. Tang, G. Godlewski, et al.: Lasers Surg. Med. 21,438 (1997)
7. R. Schober, F. Ulrich, T. Sander, et al.: Science 232, 1421 (1986)
8. L. S. Bass, N. Moazami, et al.: Lasers Surg. Med. 12, 500 (1982)
9. W. Small, P. M. Celliers, et al.: Lasers Med. Science 13, 98 (1998)
10. M. Constantinescu, A. Alfieri, G. Mihalache, et al.: Lasers Med. Sci. 22, 10 (2007)
11. L. W. Murray, L. Su, G. E. Kopchok, et al.: Lasers Surg. Med. 9, 490 (1989)
12. C. R. Guthrie, L. W. Murray, G. E. Kopchok, et al.: J. Invest. Surg. 4, 3 (1991)
13. S. D. DeCoste, W. Farinelli, T. Flotte, et al.: Lasers Surg. Med. 12, 25 (1992)
14. B. Ott, B. J. Zuger, D. Erni, et al.: Lasers Med. Sci. 16, 260 (2001)
15. T. Menovsky, J. F. Beek and M. J. C. van Gemert: Lasers Surg. Med. 19, 152 (1996)
16. G. E. Kopchok, R. A. White, G. H. White, et al.: Lasers Surg. Med. 8, 584 (1988)
17. M. C. Oz, L. S. Bass, H. W. Popp, et al.: Lasers Surg. Med. 9, 248 (1989)
18. V. L. Martinot, S. R. Mordon, et al.: Lasers Surg. Med. 15, 168 (1994)
19. K. M. McNally, B. S. Sorg, A. J. Welch, et al.: Phys. Med. Biol. 44, 983 (1999)
20. E. Strassmann, N. Loya, D. D. Gaton, et al.: Proc. SPIE 4244, 253 (2001)
21. B. P. Chan, C. Amann, A. N. Yaroslavsky, et al.: J. Surg. Res. 124, 274 (2005)
22. M. M. Judy, L. Fuh, J. L. Matthews, et al.: Proc. SPIE 2128, 506 (1994)

## 2.2 - MICROSCOPIC ANALYSIS

*In the following, we report on the microscopic analyses we carried out on corneal tissue welded by means of diode laser radiation in association with the topical application of the chromophore Indocyanine Green (ICG). The aim of this analyses was to evaluate, by means of a multifold microscopy approach (including light microscopy (LM), transmission electron microscopy (TEM), and atomic force microscopy (AFM)), the structural modifications induced in fibrillar collagen and in other non-fibrillar extracellular matrix components after a typical laser welding surgical procedure on corneal tissue. The results evidenced a marked disorganization of the normal fibrillar assembly although collagen appeared not to be denatured at the operative conditions we employed. The mechanism of laser welding may be related to some structural modifications in the main interfibrillar components found in connective tissues, i.e. proteoglycans.*
*Surgeries were performed on explanted porcine eyes by Dr. Luca Menabuoni of Unità Operativa Oculistica, Azienda USL 4 of Prato. AFM analysis was conducted in collaboration with Dr. Bruno Tiribilli of ISC-CNR of Florence.*

### 2.2.1 Introduction

Cornea represents a unique tissue mainly constituted by a highly-transparent stromal matrix. For this reason, in order to achieve a successful welding, bond must be provided in as lowest temperature as possible with a yet clinically acceptable strength but without collateral tissue damage and thermal injury that may alter permanently its morphology and function. Most of the laser welding procedures that have been proposed up to now were based on the use of water as an endogenous chromophore for absorbing near- and far-infrared laser light [1-4]. However, they did not demonstrated to be safer enough to reach the clinical phase, since the achievement of successful welding of corneal cuts was frequently accompanied by heat side effects which caused partial stromal coagulation and affected corneal transparency. Improved results were obtained using Indocyanine Green (ICG) as an exogenous chromophore topically applied to the corneal wound to enhance the absorption of low-power near-infrared diode laser radiation [5-7]. ICG is a FDA (Food and Drug Administration)-approved dye that exhibits high optical absorption around 800 nm. It is used, therefore, as a photo-enhancing chromophore under near infrared diode laser irradiation in order to induce a photothermal effect that is confined to the stained tissue. An experimental and theoretical study of the temperature dynamics during laser welding with the use of ICG [8] indicated a lower increase in temperature inside the stromal tissue,

compared with the one induced by other laser techniques that did not employ exogenous chromophores. The temperature in the irradiated site at the operative laser power density of 16.7 W/cm$^2$ was found to be in the 55-65 °C range, which is below the threshold value at which the main modifications to the collagen matrix are expected (see §2.1) [9].

In this section, we report the light (LM), atomic force (AFM) and transmission electron (TEM) microscopy analyses we performed on diode-laser welded corneal tissue in order to characterize the structural modifications in the collagen arrangement that are induced immediately after laser closuring of corneal wounds.

### 2.2.2 Materials & Methods

#### 2.2.2.1 Laser welding procedure

Freshly-enucleated porcine eyes (n=10) were cut with a pre-calibrated 3.5 mm knife and prepared for the laser welding procedure. In brief, a 12 % w/w water solution of ICG (IC-GREEN, Akorn, Buffalo Grove, IL) was placed inside the corneal cut using an anterior chamber cannula. After 2-3 min, which were necessary to stain the cut walls, it was washed out with abundant water. An AlGaAs diode laser (WELD 800, El.EN., Italy) emitting at 810 nm was used for the surgery. The device was equipped with an optical fiber of 300 μm-core-diameter, which was kept at a distance of ~2 mm from the surface of the cornea. Laser light was delivered to the cut by means of 2 s-long contiguous pulses, for a total irradiation time of approximately 25 s. The laser power emission was 80 mW, corresponding to a power density of 16.7 W/cm$^2$ on the corneal surface.

#### 2.2.2.2 Sample preparation for LM, AFM and TEM analyses

*(See Appendix A for details)*

Laser-welded and control corneas were fixed in a modified Karnovsky solution (2 % glutaraldehyde and 2 % paraformaldehyde in 0.1 mol/l sodium phosphate buffer, pH 7.0) for 5 hours, and were then rinsed twice in 0.1 mol/l sodium phosphate buffer at room temperature. Each cornea was subsequently cut into 1 × 1 mm rectangular samples including the laser-treated portion. After being stored in buffer solution overnight at 4 °C, the samples were post-fixed for 2 hours in 1 % osmium tetroxide at room temperature. After sequential dehydration, the specimens were infiltrated in epoxy resin (Sigma, St. Louis, MO, USA) and polymerized for 12 hours at 40 °C, followed by 24 hours at 60 °C. For each sample, 20 semi-thin (ST, 1.5 μm) and 3 ultra-thin (UT, 70-90 nm) slices were cut by a ultramicrotome (Power Tome PC, RCM, Tucson, AZ, USA) for light and electron microscopy measurements, respectively.

The semi-thin sections were attached to a glass slide. Toluidine blue staining was performed on 5 ST slices. In other 15 ST slices, the resin was partially removed using a saturated solution of NaOH in absolute ethyl alcohol [6], and 5 of them were processed for Hematoxylin and Eosin stain using standard pathology laboratory procedures. Other 5 slices were stained with Picrosirius Red (prepared according to Brooks' protocol [10]) in order to evaluate the birefringence of collagen under polarized light microscopy (Zeiss Axiolab, Carl Zeiss, Oberkochen, Germany). The remaining 5 slices were analyzed by AFM using a Pico SPM instrument (Agilent, Santa Clara, CA) operated in dynamic mode. Cantilevers model NSG01, NT-MDT (Zelenograd, Moscow, Russia) with a resonance frequency of about 150 kHz and a tip radius ≤ 10 nm were used. By alkaline etching of the slices, the surface layer of the embedding medium could be removed selectively, thus exposing the inner structure of the tissue within the section to the cantilever without modifying the three-dimensional architecture of the stroma. Similarly, the partial removing of the resin allowed for the staining of the inner tissutal structures by standard histology.

The UT sections were placed on copper grids, stained sequentially with uranyl acetate and lead citrate, and viewed using a transmission electron microscope (Philips CM-12, Philips Industries, Eindhoven, The Nederlands) operating at 80 kV.

#### 2.2.2.3 Morphological analysis

A morphological analysis of AFM and TEM images was performed using Image Pro Plus (Media Cybernetics, Bathesda, MD) and Image J (National Institute of Health, Bathesda, MD). The assessment of the collagen fibrils was made from the anterior 300 μm thick layer of the corneal stroma (with the corneal stroma of porcine eyes being about 800 μm in anterior-to-posterior thickness). The analysis of the laser-treated samples concerned fibrils located at the weld site. The parameters chosen to characterize the fibril integrity were the fibrillar diameter and the axial periodicity. Longitudinally-oriented fibrils were chosen for the evaluation of these parameters from both AFM and TEM images. The interfibrillar distance was obtained from AFM topographic profiles by considering the distance between the tops of adjacent longitudinally-oriented fibrils. Instead the centre-to-centre distance of transversely-cut collagen fibrils was measured from TEM micrographs. The data were reported as mean ± standard deviation.

### 2.2.3 Results

Histological Hematoxylin/Eosin examinations of the welded stroma evidenced adequate tissue bonding between the cut ends. No charring or photocoagulation signs were observed at the sealed site (**Fig. 2.6A**). **Figure 2.6B** shows the negative image of a slice of laser-

welded tissue stained with Picrosirius Red as observed by a polarized light microscope. Under cross-polarized light, an intense birefringence was seen throughout the sample. The layered structure of the stroma was clearly visible at the right and left sides of the slice that had not been subjected to laser irradiation. At the sealed site, the birefringence signal appeared more diffused, lacking the typical alternating pattern, but still remaining clearly visible. Collagen structures were observed to be binding the two edges of the cut.

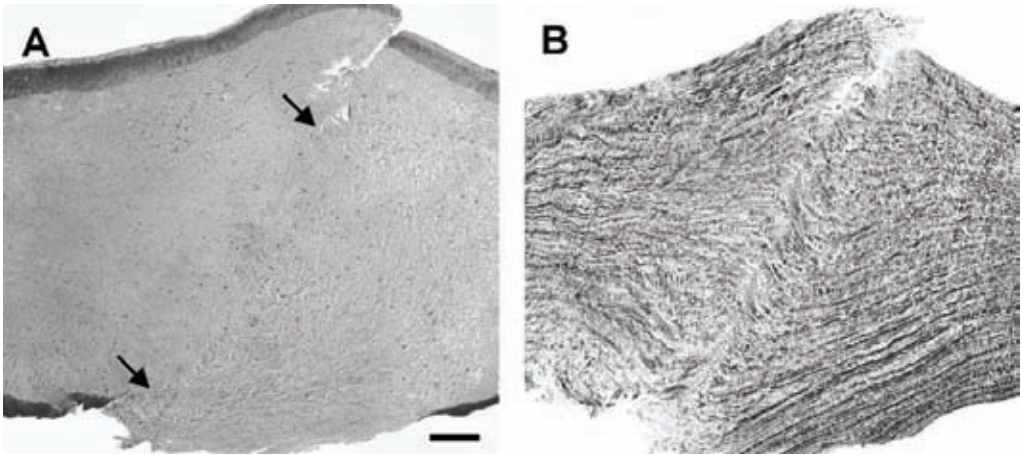


**Fig. 2.6** Microscopic examination of diode laser welded stroma (bar = 100 μm). (A): Hematoxylin/Eosin stain revealed absence of tissue coagulation or charring at the welded site (between the arrows). (B) Negative image of the same sample stained with Picrosirius Red dye shows bridging structures across the wound. The birefringence signal appears more diffused at the weld site but with an intensity comparable to the one of laser-untreated regions.

A similar situation was seen on Toluidine-stained slices (**Fig. 2.7**): lamellae with different orientations met at the weld site, where they appeared winded into skeins.

The typical TEM appearance of untreated corneal stroma is reported in **Figure 2.8A**, which shows the border between two orthogonal lamellae. The collagen fibrils appeared to be regularly organized in a parallel arrangement in each lamella and had similar interfibrillar spacings. In laser-treated samples, at the outer periphery of the weld, TEM analysis showed that the fibrils partially lost their parallel arrangement and the native intralamellar organization.

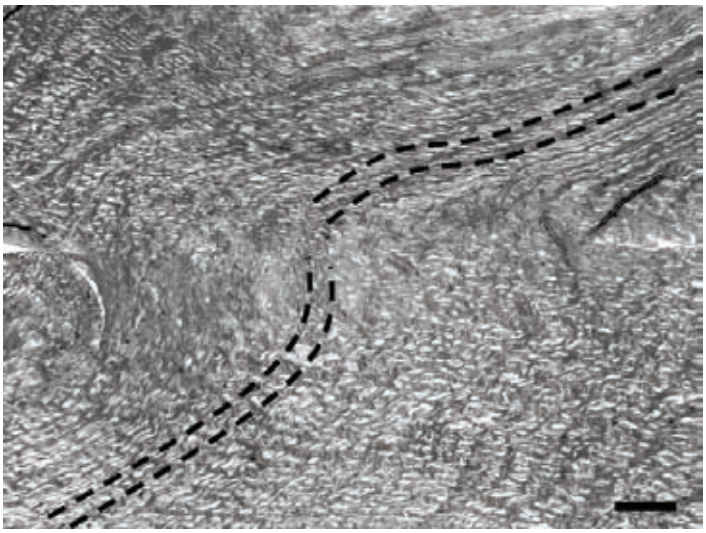

**Fig. 2.7** Welded incision in corneal stroma stained with Toluidine Blue (bar = 15 μm). Lamellae with different orientations (dashed lines) are joined at the weld site.

Fibrils located exactly at the weld site were markedly disorganized, but rarely touched each other directly. There, groups of interwoven fibrils joined the sides of the cut (**Fig. 2.8D**). Magnified images of these fibrils indicated that they were still preserving their periodical cross-striation (D-periodicity) (**Fig. 2.8C**). The margins of the collagen fibrils maintained distinct edges, and never displayed any deterioration or a frayed appearance. Outside the laser-treated zone, the regular lamellar organization of the fibrils was maintained. Electron-dense aggregates resembling the amorphous structures were seen to be dispersed throughout the irradiated area (**Fig. 2.8D**).

The quantitative analysis of the fibrillar morphology is summarized in **Table 2.1**. The analysis of mean fibril diameter and fibril diameter distribution (**Fig. 2.9**) showed no significant differences (within experimental uncertainties) between the laser-welded corneas and the control samples, as mean diameters of 27.7 (S.D. = 2.2) nm and 26.7 (S.D. = 2.0) nm were found for the control and treated corneas, respectively. It was almost impossible to obtain the axial periodicity value from the TEM images. This was due to the rather indistinct cross-striation characterizing the native collagen fibrils (**see Fig. 2.8C**).

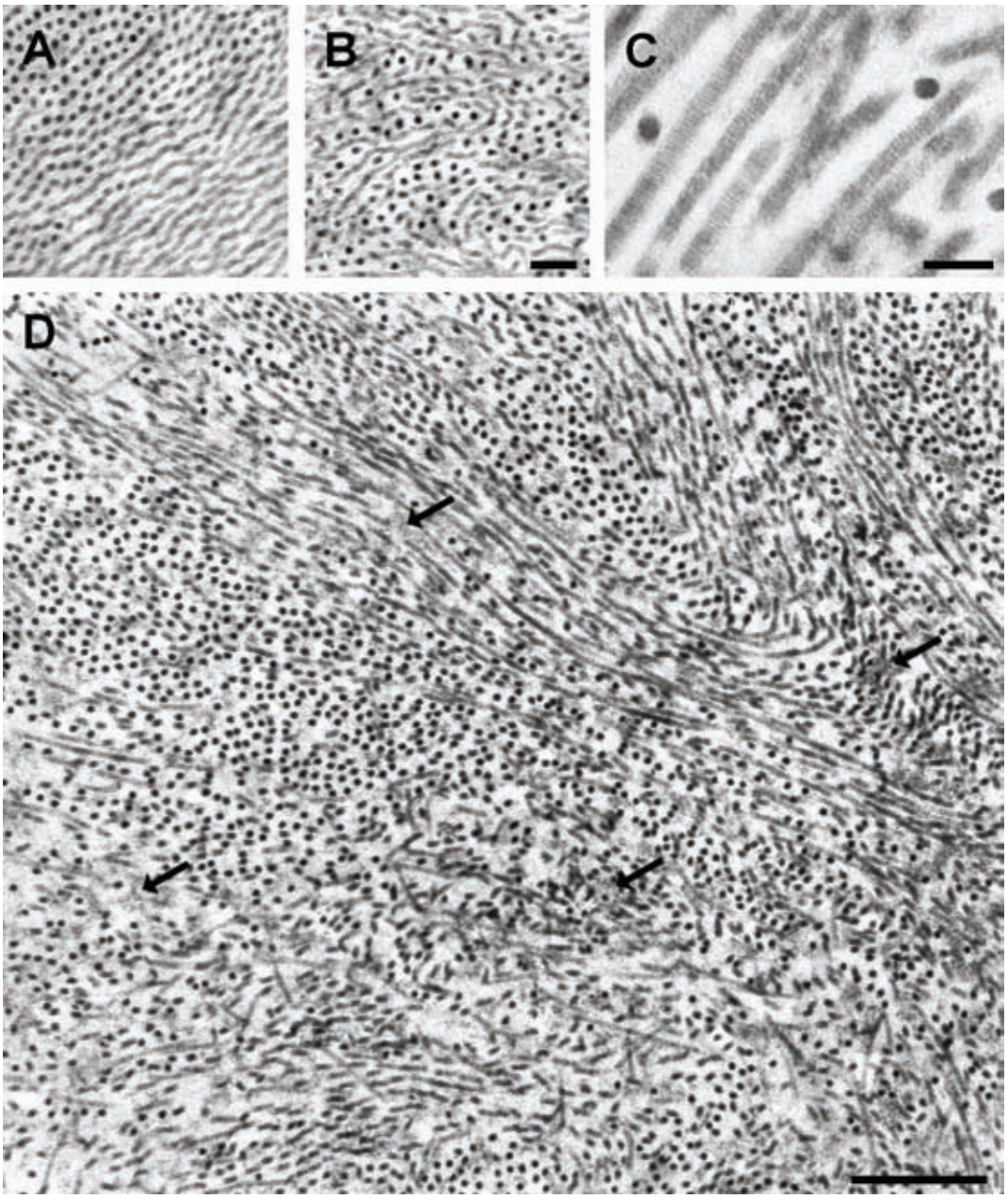


**Fig. 2.8** TEM micrographs showing the fibrillar arrangement observed (A): in a control corneal stroma, (B): in the periphery of the cut of a welded cornea, and (C, D): at the weld site. Cross striation of fibrils is still observable after the laser treatment (C). (A,B: bar = 200 nm, C: bar = 100 nm, D: bar=500 nm ). Arrows indicate electron dense aggregates.

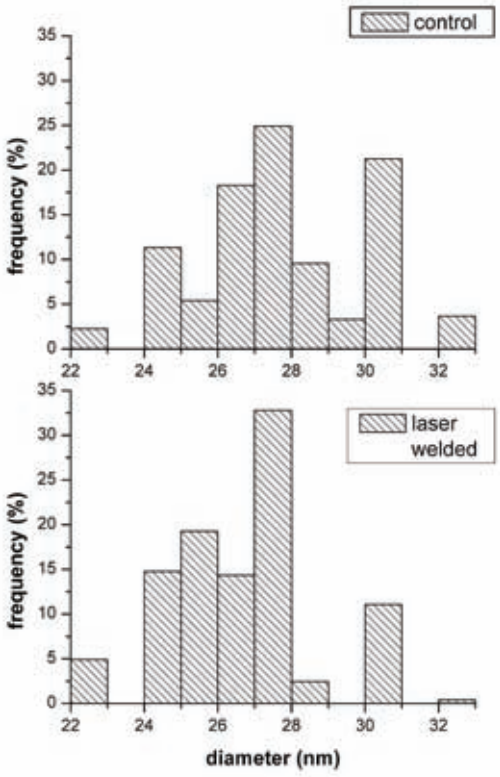


**Fig. 2.9** Distribution of fibril diameters in control and laser-welded stroma. Mean diameters are 27.7 ± 2.2 nm (number of sampled fibrils n = 574) and 26.7 ± 2.0 nm (n = 244), respectively.

**Table 2.1**
Comparison of the morphological features of laser-treated and control collagen fibrils as derived by AFM and TEM
C = control stroma; L= laser-welded stroma; n.d. = not detected

| | | Diameter (nm) | Periodicity (nm) | Interfibrillar distance (nm) |
|---|---|---|---|---|
| AFM | C | 36.2 ± 8.7 (n = 91) | 22 – 39 (n = 106) | 54.1 ± 13.3 nm (n = 86) |
| | L | 35.6 ± 10.0 (n = 50) | 20 – 37 (n = 59) | loss of parallel arrangement |
| TEM | C | 27.4 ± 2.1 (n = 574) | n.d. | 59.7 ± 7.5 nm (n = 123) |
| | L | 26.8 ± 2.3 (n = 244) | n.d. | loss of parallel arrangement |

AFM analysis supported the TEM data, substantially confirming the observations described above. AFM images of control and laser-treated cornea samples were analyzed (**Table 2.1**) considering profiles taken transversely or longitudinally to the fibrillar axes for assessing fibrillar diameter and interfibrillar distance or periodicity, respectively (see the example shown in F**ig. 2.10** bottom panel). The AFM topographies of control corneas showed well-organized collagen fibrils (36.2 ± 8.7 nm in size) running parallel to each other as in a typical intralamellar domain (**Fig. 2.10A,B**). The fibrils exhibited a beaded pattern

with an axial periodicity ranging from 22 to 39 nm. In well-separated control fibrils, bridge-like structures connecting adjacent collagen fibrils were sometimes observed (**Fig. 2.10C**). AFM images of the laser-treated corneal stroma showed a random distribution of fibrillar bundles (**Fig. 2.10D,E**). However, fibril diameters and periodicity were similar to the ones observed in the control samples. In addition, rather broad unstructured zones devoid of a clear morphology were frequently noted throughout the laser-treated specimens (**Fig. 2.10F**).

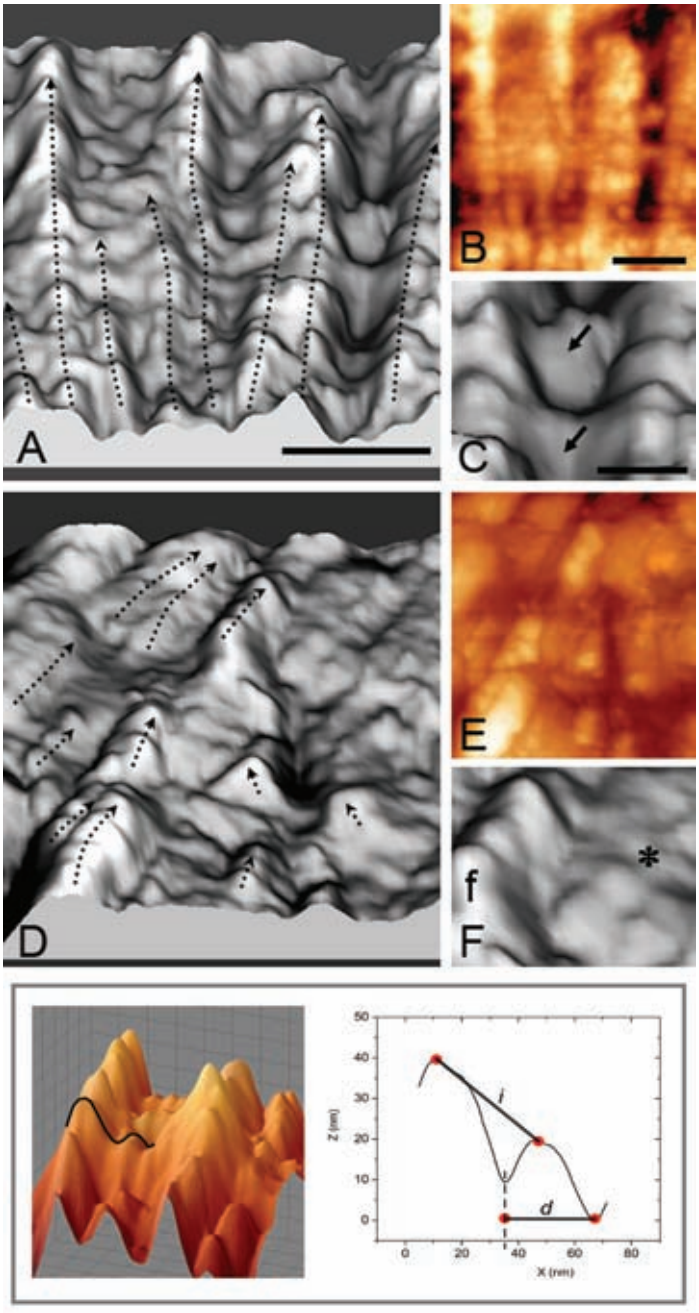


**Fig. 2.10** AFM topographies of corneal stroma samples. 3D (A,C,D,F) and 2D (B,E) rendering of control (A,B,C) and diode laser-welded (D,E,F) specimens. Arrows indicate bridge-like inter-fibrillar structures.
f collagen fibril;
* unstructured material.
(A,B,D,E: bar = 100 nm; C,F: bar = 50 nm).
Bottom panel: transverse profile (right) taken from an AFM surface plot of a selected portion of control stroma (left), example of the measurement of characteristic fibrillar parameters as fibrillar diameter (*d*) and interfibrillar distance (*i*).

### 2.2.4 Discussion

Laser-induced morphological alterations of collagen fibrils are considered to play a primary role in the laser welding mechanism (see §2.1) [11,12]. However, experimental and theoretical studies on the heat diffusion during diode laser welding of corneal tissue suggested operative temperature values at the limit of the denaturation threshold of fibrillar collagen (i.e. in the 55-65 °C range while the denaturation of collagen normally starts beyond 65 °C) [8]. Our microscopy study is strikingly in accordance with this picture. In fact it pointed out a minor involvement of fibrillar collagen in the mechanism of laser welding, as first suggested by light microscopy and then well-delineated by the microscopies at the nanometric level.

Polarized light microscopy showed an intense birefringence signal associated with Picrosirius Red throughout the sample. In particular, outside the welded cut, lamellae showed the typical alternating birefringence pattern of a normal cornea. At the weld site, the birefringence signal was still present, but the lamellar sheet pattern lost its net boundaries between lamellae. Presence of collagen structures connecting the cut edges was evidenced under polarized light, as also confirmed by means of Toluidine Blue staining. In any case, we never observed any birefringence reduction or loss of the type that is typically associated with heat- or laser-induced thermal damage that affects the fibrillar structure of collagen [10,13-15]. Thus, the substantial preservation of birefringence also at the weld site may be interpreted as the absence of coagulated (hyalinized) fibrillar collagen. On the other hand, since Picrosirius Red is ineffective in detecting proteoglycans or other collagen types other than fibrillar collagen [16], we cannot exclude the occurrence of more significant thermal modifications in these ground substance components surrounding the collagen fibrils, as discussed in the following.

TEM and AFM analyses provided a more detailed picture of the collagen modifications induced by corneal welding. Observations of the welded region showed groups of fibrils interwoven across the cut. Moreover, the structure of each individual fibril appeared not to be modified by laser irradiation, showing a full preservation of the regular cross-striation and of regular diameter. The slightly greater value of the fibrillar size found by the AFM analysis was probably a result of the distortion typical of cantilever tip convolution [17]. In fact, the value of the tip size that we employed (≤10 nm) was comparable to the difference between the TEM and AFM fibrillar diameter main values, as reported in **Table 2.1**. The periodicity along the fibrils of laser-treated samples evaluated by AFM furnished values comparable to those found in native corneas. Actually, these values did not fit the expected 67 nm D-periodicity of collagen fibrils [18]. However, the attitude of AFM to resolve more than one band per D-period was previously pointed out [19 and refs. therein]. Additionally,

we note that the alkaline etching of the epon resin carried out to expose the outer layer of the specimen to the cantilever, could partially "clean off" the ground substance surrounding the collagen fibril thus amplifying the visibility of the D-periodicity.

In summary, the observed fibrillar disorganization in the region of the laser-welded corneal cut was never accompanied by thermally-induced ultrastructural modifications of the fibrillar structure, in contrast to what has been reported in the literature. Schober et al. [20] observed an increase in fibril caliber, a loss of periodicity, and a splitting into fine fibrillar substructures. A similar effect was seen in dura mater subjected to $CO_2$ laser irradiation [21], in tendon specimens heated at 60 °C for twenty minutes in water bath [22], in joint capsular collagen under Holmium:YAG irradiation [23], and in diode laser-assisted anastomosis of arteries performed without exogenous chromophores at a relatively high diode laser power of 250 W/cm$^2$ [24]. In all these cases, high temperatures or long exposure times promoted partial collagen denaturation that was characterized by an unwinding of the triple helix and a subsequent loss of fibrillar integrity. This triple-helix unraveling, followed by "interdigitation" on cooling between fibers, was indicated by Shober et al. as the structural basis for laser-induced welding [20].

Our different results let us conclude that fibrillar collagen was not denatured in our laser conditions, confirming previous thermodynamic studies [8], and thus was not directly involved in the closure mechanism of corneal cuts. Instead, the loss of organization of the collagen bundles observed at the weld site can probably be correlated to some structural modification in other main extracellular components. It is recognized that proteoglycans are interfibrillar macromolecules which play a primary role in stabilizing and maintaining the orderly arrangement of fibrils within the corneal stroma [25,26]. We propose a direct involvement of these compounds in the molecular mechanism of diode-laser welding of corneal tissue. As a matter of fact, the bridge-like structures observed in the control cornea and the amorphous material found to be randomly present in the welded samples may be attributed to proteoglycans, which underwent thermal modifications, as previously suggested [27]. In this regard, we may tentatively hypothesize a primary role for proteoglycans which could undergo some modifications at the typical temperature values induced by diode laser welding (55-65 °C), and then be rearranged upon cooling in a way of connecting collagen fibrils together .

### 2.2.5 Conclusions

Our microscopic analysis has made it possible to characterize the supramolecular modifications in stromal extracellular matrix that follow a typical diode-laser welding intervention of corneal tissue. The unaltered structural properties of fibrillar collagen

indicated that its denaturation did not occur at the operative laser energy that we used. However a marked disorganization in the fibrils was noted at the weld site. This led us to hypothesize the involvement of proteoglycans in the diode laser-welding mechanism of corneal stroma.

## References


1. N.L. Burstein, J.M. Williams, et al.: Arch. Ophthalmol 110, 12 (1992)
2. T.J. Desmettre, S.R. Mordon, and V. Mitchell: Proc. SPIE 2623, 372 (1996)
3. H.E. Savage, R.K. Halder, et al.: Lasers Surg. Med. 35, 293 (2004)
4. M. Barak, O. Eyal, et al.: Surv. Ophthalmol. 42(Suppl 1), S77 (1996)
5. L. Menabuoni, B. Dragoni, and R. Pini: Proc. SPIE 2922, 449 (1996)
6. F. Rossi, R. Pini, et al.: J. Biomed. Opt. 10, 024004 (2005)
7. R. Pini, F. Rossi, et al: Proc. SPIE 5314, 245 (2004)
8. F. Rossi, R. Pini, and L. Menabuoni: J. Biomed. Opt. 12, 014031 2007)
9. J. Kampmeier, B. Radt, et al.: Cornea 19, 355 (2000)
10. S.G. Brooks, S. Ashley, et al.: Lasers Med. Sci. 6, 399 (1991)
11. K. M. McNally: Laser tissue welding. Chap. 39. In: Biomedical Photonics Handbook, ed by T. Vo-Dihn (CRC Press, Boca Raton, 2003) pp 1–45
12. R. Pini, F. Rossi et al.: Laser tissue welding in minimally invasive surgery and microsurgery. Chap. 15. In: Biophotonics. Series: Biological and Medical Physics, Biomedical Engineering, ed by L. Pavesi and P.M. Fauchet (Springer-Verlag, Berlin, Heidelberg, 2008) pp 275-299
13. M.N. Asiyo-Vogel, R. Brinkmann, et al.: J. Cataract Refract. Surg. 23, 515 (1997)
14. D.J. Maitland and J.T. Walsh: Lasers Surg. Med. 20, 310 (1997)
15. V. Sankaran and J.T. Walsh: Photochem. Photobiol. 68, 846 (1998)
16. L.C.U. Junqueira, G. Bignolas, and R.R. Brentani: Histochem. J. 11, 447 (1979)
17. S. Yamamoto, J. Hitomi, et al.: Arch. Histol. Cytol. 60, 371 (1997)
18. D.F. Holmes, C.J. Gilpin, et al.: Proc. Natl. Acad. Sci. USA 98, 7307 (2001)
19. N.J. Fullwood, A. Hammiche, et al.: Curr. Eye Res. 14, 529 (1995)
20. R. Schober, F. Ulrich, et al.: Science 232, 1421 (1986)
21. T. Menovsky, J.F. Beek, and M.J.C. van Gemert: Lasers Surg. Med. 19, 152 (1996)
22. R.R. Anderson, G.M. Lemole, et al.: Lasers Surg. Med. Suppl 6, 56 (1994)
23. K. Hayashi, G. Thabit III, et al:: Arthroscopy 12, 474 (1996)
24. J. Tang, G. Godlewski, et al.: Lasers Surg. Med. 21, 438 (1997)
25. M. Hirsch, G. Prenant, and G. Renard: Exp. Eye Res. 72, 123 (2001)
26. K.M. Meek, C. Boote Exp. Eye Res. 78, 503 (2004)
27. P. Kronick, B. Maleeff, and R. Carroll: Connect. Tissue Res. 18, 123 (1988)

# 2.3 - CHEMICAL ANALYSIS

*As a complement to the previous section, this part will focus on the chemical analyses that have been performed on a model molecule (hyaluronan) in order to investigate the direct involvement of proteoglycans in the mechanism of diode laser welding of the cornea. In conclusion, an hypothesis on the mechanism of laser welding, based on the reorganization of corneal proteoglycans, is proposed.*
*FTIR and DSC analyses were performed in collaboration with Prof. Luigi Dei of the Department of Chemistry, University of Florence.*

## 2.3.1 Introduction

### 2.3.1.1 Proteoglycans

In higher multicellular eukaryotic organisms the space between cells is composed of the extracellular matrix (ECM) of tissues. The ECM consists of insoluble collagen fibrils and soluble polymeric structures, mainly proteoglycans (PGs), that together are responsible for the tissue adjustment related to the stress of movement and the maintenance of the organism's shape [1]. The fibrils are inextensible; they resist and transmit tensile stress, defining the maximum size of the tissue. The PGs swell the aqueous space between fibrils, taking compressive stresses and limiting tissue collapse under pressure. Water-soluble molecules diffuse through the aqueous PG channels to and from cells. In addition to the mechanical functions, PGs play an essential part in the multiple regulatory functions including cell proliferation, cell migration, extracellular matrix deposition, cell-matrix interaction, and tissue morphogenesis and repair.

These PGs usually have a globular protein part (head) to which glucosaminoglycans (GAGs) are attached (tails) [2]. The proteins are gene products and the GAGs are post-traslational modifications. The greater part of GAGs is associated with a few types of PGs, simply described as small (~100 kDA), large (>200 kDa) and very large (≈1 MDa) (**Fig. 2.11**). Their proteins have different primary structures and shapes. The small PGs are constituted by 1 globular protein and 1 (or less frequently 2) GAGs chain(s), while the large and very large PGs have at least 1 globular and 1 linear polypeptide domain with 5-10, and up to 100 GAGs chains, respectively. Soft-fibrous tissues (tendon, skin, cornea, etc.) contain predominantly type I collagen associated with small PGs, such as proteodermatan sulfates (also called decorin) and proteokeratan sulfates (which include lumican and fibromodulin) of molecular mass ~100 kDA, ~50 % of which is protein and the rest is GAG. Very large

PGs are responsible for the elastic response of articular cartilage to loading, like the stuffing in a cushion. Large PGs have similar pressure resistant functions.

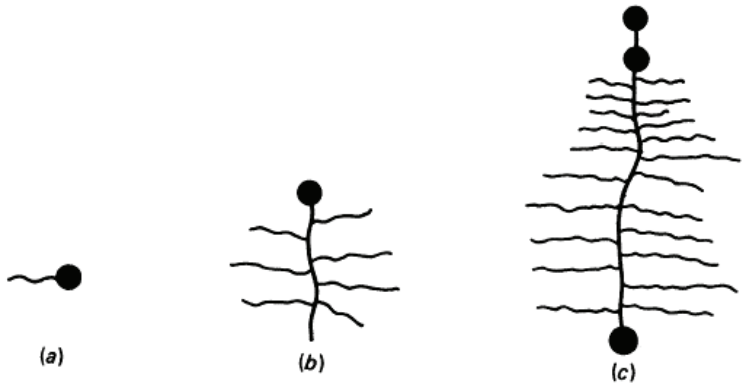


**Fig. 2.11** Diagrammatic illustrations of the appearance of (a) the small, (b) the large, and (c) the very large proteoglycans (from [2]).

GAGs consist of long, unbranched chains of repeating disaccharide units classified as chondroitins, dermatans, keratans, which are sulfated, and hyaluronan, which is not (**Fig. 2.12**). A similar group, the heparans, are particularly associated with cell and basements membranes. Evolutionary selection pressures and exogenous selection pressures mediated by microbes interacting with GAGs contributed to the their diversification [3]. These polymers differ in the type of disaccharides they utilize as building blocks, and in the linkage between the building blocks [2]. Such diversification led to their division into three structural groups: 1) cellobiose (e.g., hyaluronan), (2) polylactoseamines (e.g., dermatan, chondroitin, and keratan sulfate), and (3) polymaltose (heparin, heparan sulfate). Chondroitin sulfate (CS), dermatan sulphate (DS), keratan sulfate (KS), and hyaluronan (HA) have very similar polymer backbone structures (1:3, 1:4 $\beta$-linked pyranose rings) (**Fig. 2.12**). In solution they are supposed to assume helical conformations with 2 disaccharides (**Fig. 2.13**) per complete helix turn (twofold helix), as shown by NMR [2,4] and confirmed by modeling and computer simulation [5]. GAGs's twofold helix is stiffened by intramolecular H-bonds and by the repulsion between the anionic sites [6]. All GAGs reveal large hydrophobic patches, spread over 3 sugar units, present on both sides of the polymer (see **Fig. 2.13**), and consisting of 7-9 CH units-equivalent to a fatty acid. Monomeric units of hyaluronan, keratan sulfate and chondroitin are stable $^4C_1$ chair conformers in physiological condition.

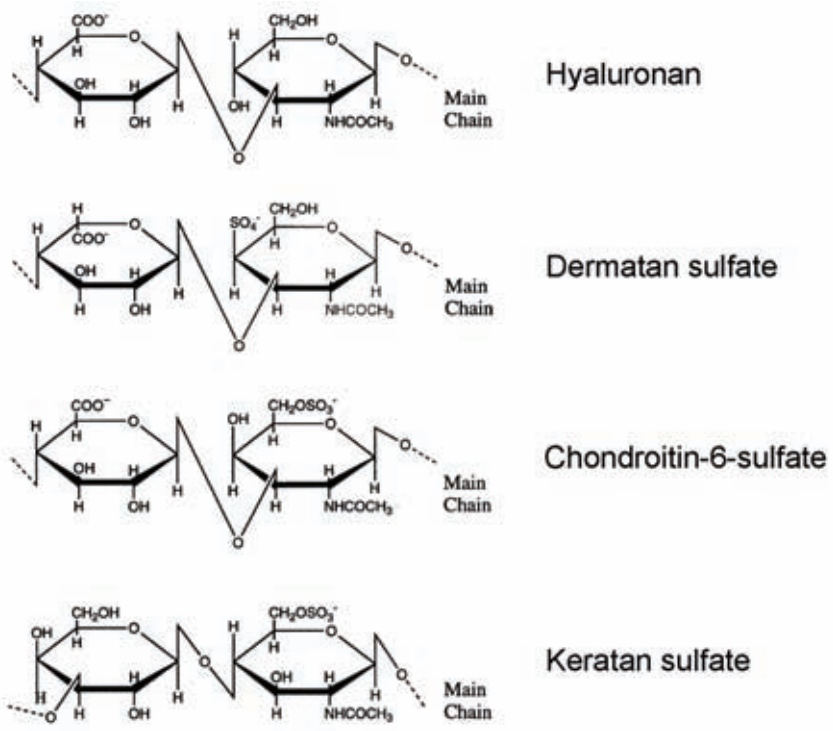


**Fig. 2.12** Primary structures of building blocks of selected GAGs. The linkage geometry between predominant monomeric units are: Hyaluronan: -4GlcUA$\beta$1-3GlcNAc$\beta$1-; Dermatan sulfate: -4IdoUA$\beta$1-3GalNAc(4S)$\beta$1-; Chondroitin-6-sulfate: -4GlcUA$\beta$1-3GalNAc(6S)$\beta$1-; Keratan sulfate: -3Gal$\beta$1-4GlcNAc(6S)$\beta$1- (where GlcUA = $\beta$-D-glucuronic acid; IdoUA = $\alpha$-L-iduronic acid; Gal = $\beta$-D-galactose; GalNAc = $\beta$-D-N-acetylgalactosamine; GlcNAc = $\alpha$-D-N-acetylglucosamine).

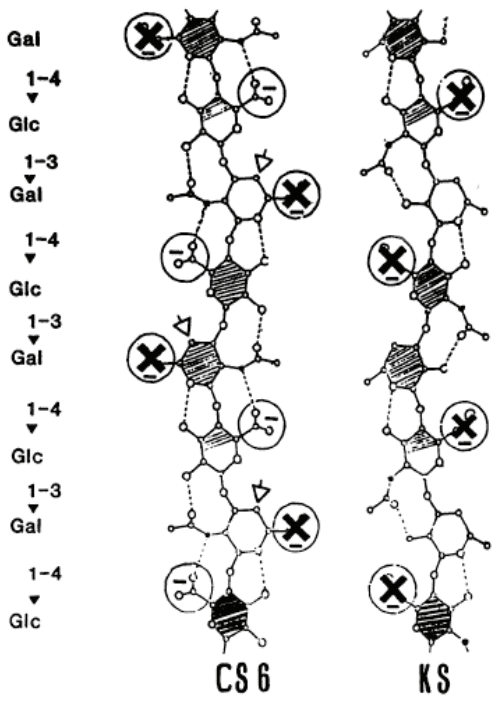


**Fig. 2.13** Secondary structures of selected GAGs in water solution. Chondroitin-6-sulfate (CS6) as well as keratan sulfate (KS) assume a twofold helix conformation stiffened by intramolecular H-bonds and by the repulsion between the anionic sites (ringed, ester sulfate = X and carboxylates). Both CS6 and KS are Gal$\beta$1→4,Glc$\beta$1→3 polymers, with a stable $^4C_1$ chair conformation. Hyaluronan (HA) is identical to CS6 without sulfation, with GlcNAc instead of GalNAc, and with an extra H-bond from GlcNAc C4OH to GlcUA ring oxygen, which is not possible from the axial GalNAc C4OH (arrowed). This position is sulfated in CS4 and in DS, concentrating the charges closer to the center line than in CS6. In DS, if the IdoUA ring is $^4C_1$ (unfavored), the carboxylate group is axial, at right angles to the plane of the paper, thus bringing this charge closer to the center line of the polymer than in CS4 or CS6. If IdoUA is $^1C_4$ (favored), the carboxylate is equatorial, as is that in CS4, CS6, and HA. Hydrophobic patches (cross-hatched) are in identical positions in all four GAGs. (from [1])

The structure of dermatan sulfate helix is, instead, somewhat different with respect to that of the other GAGs. This GAG is metabolically derived from chondroitin sulfate by epimerization of D-glucuronate (GlcUA) to L-Iduronate (IdoUA). The percentage epimerized varies from around 30 % in cornea and cartilage to over 80 % in skin and sclera. In contrast to GlcUA, which has a stable $^4C_1$-conformation, IdoUA can take up other two more compact conformations, i.e. $^1C_4$, and $^2S_0$, with minimal energy exchange [7] ($^2S_0$ is intermediate between $^4C_1$and $^1C_4$). There are thus many possible secondary structures within a dermatan chain. However, it was demonstrated that the compact conformers are preferred over $^4C_1$ in water solution [7].

#### 2.3.1.2 Proposed GAG-GAG interactions in vitro and in tissues

GAGs chains have been proposed to aggregate *in vitro* via hydrophobic bonding and hydrogen bonding between anti-parallel twofold helices, in a similar manner as for DNA double helix [1,2]. The more charged are the GAGs, the greater their mutual repulsion and the lower the stability of their aggregates. Furthermore, the position of anionic sulfate ester groups would determine whether aggregates can form [1]. In chondroitin-4-sulfate they are present along the central axis of the polymer, giving a highly concentrated polyanionic field; instead, in chondroitin-6-sulfate, sulfates are at the periphery of the twofold helix, giving a less intense polyanionic field and a weaker mutual repulsion between polymer chains. Computation and electron microscopy agreed that aggregates formation was possible in this latter case, other than for KS, which have an equivalent sulfates disposition, but not in that of chondroitin-4-sulfate [1]. DS sulfation is sometimes very low to the point of qualifying it as a non-sulfated chondroitin and these structures would aggregate easily, like HA (which is, equally, not sulfated). In cornea DSs have regular ~50% (4-)sulfation (i.e. alternating non-sulfated and sulfated disaccharides). This means that the polymer has the sulfate groups on one face of the twofold helix. Computation showed that aggregation can take place on the non-sulfated face [1]. By means of light-scattering studies, DS was demonstrate to self-aggregate in physiological solution [8] and then dissociate in 1M urea solution, suggesting involvement of H-bonds in the aggregation process. In particular results pointed out the formation of DS-DS aggregates which were successively called “duplexes” [1,2]. DS aggregation in dimethylsulphoxide solution was much reduced by competing lipids, implying disruption of hydrophobic DS-DS interactions [2]. An equilibrium constant of $10^4$ was tentatively proposed for DS duplexes [8].

In connective tissues, collagen fibrils and PGs form a dense and well-organized mutually interconnecting network. The interfibrillar PGs constitute a well-defined, complex molecular chain system providing rigid bridges between the fibrils and thereby being

responsible for the maintenance of the regular array of collagen fibrils [1]. PGs are equidistant and orthogonally attached at specific sites of the collagen fibrils by their protein cores (**Fig. 2.14**).

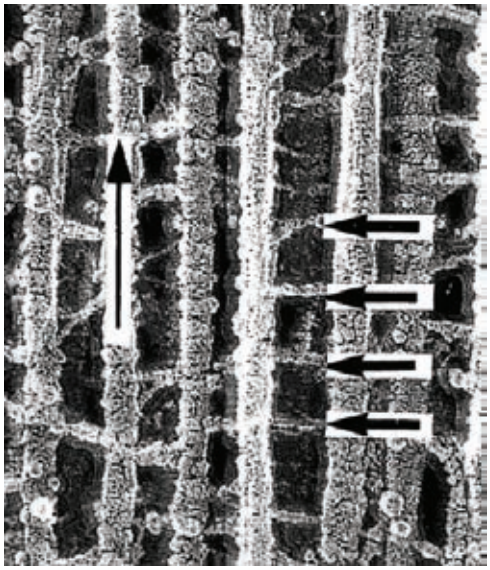

**Fig. 2.14** Proteoglycans (short arrows) orthogonally bridging two collagen fibrils (long arrow) of human posterior corneal stroma at regular intervals. Samples were ultrarapidly-frozen onto a copper block cooled by liquid nitrogen, freeze-fractured, deeply etched and rotary replicated with platinum-carbon. Replicas were examined in a transmission electron microscope equipped with a tilting device (from [9])

The interaction of the PGs with collagen fibrils is thought to be noncovalent and is characterized by an affinity constant of ~$10^8$ $M^{-1}$ [10]. By using a specific proteoglycan staining for electron microscopy, GAGs have been shown to interact with collagen fibrils on specific binding sites, forming antiparallel doublets that make it possible to maintain the relative position among the adjacent collagen fibrils [2,11] (**Fig. 2.15**). It was proposed that 2 GAG chains, 1 from each PG, form duplexes, covering the space between fibrils, anchored by protein cores attached to each fibril [11] (**Fig. 2.15** bottom panel). Stability after chemical treatments in the tissues of GAGs bridges visualized by electron histochemistry - crucially the disruptive effects of urea in the presence of non-ionic detergent, which were much greater than either separately - was compatible with postulated hydrophobic and H-bonded aggregates [12].

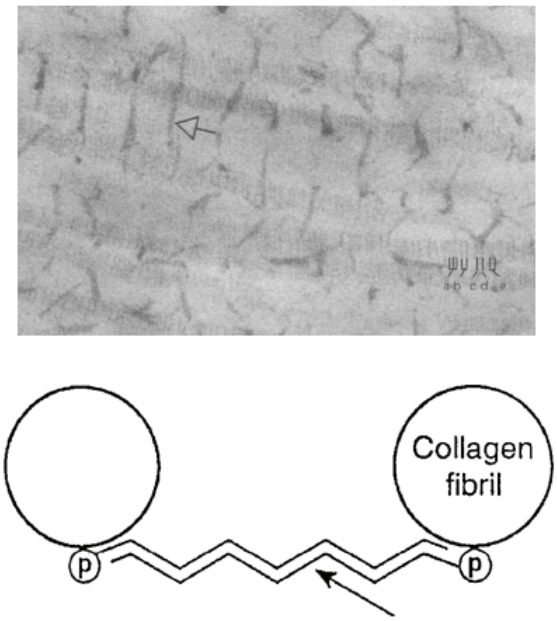


**Fig. 2.15** Transmission electron micrograph of bovine corneal stroma obtained by using a specific PGs stain (Cupromeronic Blue in 0.05 M $MgCl_2$) (from [2]). Proteoglycans bridges of DS-conjugated PGs (arrowed) between collagen fibrils are visible as dark filaments arrayed mainly orthogonally to the fibrils and interacting with collagen at specific binding sites. In corneal stroma DS-conjugated PGs bind at the d and e bands while bands a and c are occupied by KS-conjugated PGs. (bottom) scheme of a PGs duplex connecting two collagen fibrils by the GAG chains (arrow) as proposed by Scott [2,11].

#### 2.3.1.3 Hyaluronan

Because of its greater simplicity and availability, unsulfated HA is the archetypal GAG with which the others can be compared. The properties of the other GAGs aggregates can be deduced, in first approximation, from the structural behavior of HA. Here follows a brief summary of the main literature dedicated to hyaluronan structuring *in vitro*.

Hyaluronan (HA) (**Fig. 2.16**) is a high molecular mass linear glycosaminoglycan consisting of N-acetyl-D-glucosamine (GlcNAc) and D-glucuronic acid (GlcA), which form the disaccharide repeat (-GlcNAc-β1,4-GlcA-β1,3). HA is a major component of the extracellular matrix of vertebrates where it is involved in maintaining osmotic balance and reducing friction in tissues such as the synovium, vitreous humor, and cartilage. The distinctive biomechanical properties of HA have been utilized in the development of numerous biomedical products. For example, HA solutions are used as protectants of the cornea in dry eyes, as substitutes for vitreous fluid in eye surgery and, as lubricants in the treatment of osteoarthritic joints. HA also forms the structural basis of the pericellular matrix and contributes to mediating and modulating cell adhesion, as well as to other biological processes, such as development, tumor metastasis, and inflammation [13-15].

The wide range of biological functions of HA suggests the existence of a correspondingly large repertoire of conformations. Extensive research has been carried out over the past sixty years on the structural properties expressed by HA in solution, but, at present, the question is still controversial. In dilute solution at physiological pH and ionic strength, HA chains assume a stiffened random worm-like coil configuration, with a persistent length of about 5-7 nm, occupying a large hydrodynamic volume [14, 16]. The local stiffening responsible for generating the persistence length is partly due to the mutual electrostatic repulsion among carboxyl groups, and mainly to the existence of intramolecular hydrogen bonds bridging adjacent monosaccharide units, which restricts rotation and flexion at the glycosidic linkages [17-19]. Molecular dynamics simulations and NMR data on HA oligosaccharides in water suggested that these hydrogen bonds are in rapid (in the sub-nanosecond timescale) exchange with water [20, 21]. The resulting picture is a highly dynamic ensemble of chaotically interchanging semiordered states, as recently confirmed by NMR data [22, 23]. Because of the huge hydrodynamic volume and high molecular weight of HA, its individual chains are brought in contact and begin to entangle each other at concentrations above ~1 mg/ml (for MW about 1-2 MDa) [17, 24]. This leads to high elastoviscous solutions showing non-ideal behavior (non-Newtonian viscosity), which, however, can be predicted by a simple expression for polymer solution viscosity, not invoking stable associations [15]. Experimental results of HA diffusion in a wide range (0.05-10 mg/ml) of concentrations also confirmed that the overlapping of the domains of the individual molecules does not lead to the formation of stable networks, typical of a gel [25].

However, evidence of HA aggregation has also been reported: HA short segments have been demonstrated to self-associate in physiological solution [26, 27], while a variety of intermolecular aggregates were observed when HA was spread on surfaces [28, 29]. Furthermore, Scott and co-workers, on the basis of electron microscopy [30] and NMR [31] data, proposed the formation of highly ordered arrangements mediated by hydrogen-bonding and hydrophobic interactions among antiparallel HA chains, forming planar or curved sheets. These chain-chain interactions were reported to be reversibly disaggregated by an increase in temperature or by alkalinisation [30, 32]. Recent infrared spectroscopy studies have suggested the formation of three dimensional superstructures of HA chains stabilized by water bridges [33-35]. This water-mediated supramolecular assembly was shown to break down progressively when the temperature was increased to over ~40 °C [36], in accordance with previous NMR observations [32].

In the present work we aim to investigate more deeply the HA's ability to form supramolecular aggregates. Scientists have mainly focused their attention on dilute solutions of HA in order to study its physiochemical properties without the influence of nonspecific

interactions. However, HA can be found highly concentrated in some biological compartments, as in the synovium or in the umbilical cord. Moreover, pericellular, intercellular and intracellular sites, where HA performs several critical biological roles [37, 38], are locations characterized by high levels of macromolecular crowding. These constraining environments can potentially lead to intermolecular associations by favoring the approach between adjacent chains, and thus to increase the “effective” molecular concentration, as suggested by a recent concept [39, 40]. We used the combination of falling ball method (FBM), differential scanning calorimetry (DSC), Fourier transform infrared (FTIR) spectroscopy, and polarized-light microscopy (PLM) in order to build up a consistent picture of HA’s ability to constitute stable superstructures under high concentration conditions.

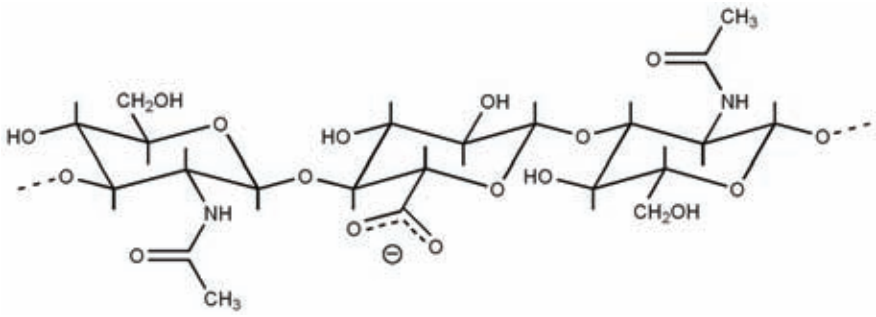

**Fig. 2.16** Schematic chemical representation of a trisaccharide of HA including the repeating disaccharide unit consisting of *N*-acetyl-D-glucosamine and D-glucuronic acid.

### 2.3.2 Experimental section

#### 2.3.2.1 Materials

We have used HA obtained from a bacterial source in order to minimize the protein-mediated aggregation of polymer chains, which might occur if HA from an animal source was employed [24, 41]. In particular, HA sodium salt from *Streptococcus equi* (Esperis S.p.a, Milan, Italy) having a molecular mass of approx. 1.000 kDa was used. The protein content was found to be lower than approx. 0.025% by means of specific quantitative spectrophotometric analysis. Different concentrations of the polymer in 0.15 M NaCl solution were separately prepared in small glass vials. The samples were homogenized by heating them in a thermostat oven at ~ 60 °C for ca. 4 h; such a period has been shown to be suitable for avoiding any type of molecular weight reduction [42] assuring a good rate of homogenization [43]. The vials were then kept closed at room temperature for about one month in order to obtain well-equilibrated samples prior to analysis.

#### 2.3.2.2 Falling ball method

HA samples were sealed in a glass tube 10 cm in length and 1 cm in diameter. The filled tube was left in place at room temperature in the dark for several days (typically one month) until complete equilibration of the solution was achieved. Then the tube was opened and a tungsten carbide ball of 0.5 mm in diameter and density of 14.9 g/ml was put at its top. We measured the distance covered by the ball in 1 min at a fixed temperature.

#### 2.3.2.3 Differential scanning calorimetry

DSC measurements were performed using a Q1000 (TA Instruments) equipped with a universal Analysis 2000 Version 3.7A software. Steel sample pans (TA Instruments) hermetically sealed to avoid water evaporation were used. The weight of the samples was checked at the beginning and at the end of the measurements, and only measurements in which no evaporation had occurred were considered. The sample was first equilibrated at 0 °C, heated to 80 °C and then cooled from 80 °C to 0 °C at 5 °C $min^{-1}$ both in the heating and in the cooling mode. Measurements were made under a dry nitrogen flow of 40 $cm^3$/min. The calibration of the DSC apparatus was performed through the melting of the indium.

#### 2.3.2.4 Infrared spectroscopy

FTIR spectra were collected in the mid-IR range (4000-1000 $cm^{-1}$) with a Nexus 870-FTIR (Thermo-Nicolet), in transmittance mode, with a resolution of 4 $cm^{-1}$, with 32 scans per spectrum, and no mathematical correction (e.g. smoothing) was performed. In a typical experiment, a small amount (about 1.5 mg) of the sample was placed between two $CaF_2$ windows, which were then sealed using a Teflon tape. This was done in order to avoid possible water evaporation during spectra recording at higher temperatures. The spectrum of the $CaF_2$ probe alone was used as a reference in the absorbance calculations.

#### 2.3.2.5 Polarized-light microscopy (PLM)

HA samples were observed under circular polarization using a polarized-light microscope (Leica DM 2500 P). Typically, a sample amount of about 3 mg was sandwiched between a microscope slide and a glass coverslip appropriately pre-treated, stored at room temperature for up to one week and then observed. The pre-treatment of the glass slides was twofold in order to create a hydrophilic or a hydrophobic environment. For the first purpose, the glasses were first cleaned with a non-ionic detergent, treated with a saturated solution of NaOH in ethyl alcohol for 1 h, and then rinsed with water. Other glasses were sprayed with a plasticizer (Plastivel, Mark Service), which, upon drying, formed a thin, transparent and homogeneous layer over the glass surface.

### 2.3.3 Results and Discussion

The properties of HA (**Fig. 2.16**) have been investigated in the literature using a variety of techniques, typically in dilute solution, i.e. in the range 0.1-1 mg/ml. Under physiological solvent conditions at low concentration, HA molecules adopt a stiffened random coil configuration. Increasing the concentration, because of the extended hydrodynamic domains of the polymer, HA chains begin to entangle conferring to the solution distinctive hydrodynamic properties (viscoelasticity is dramatically increased) [15]. Previous studies on HA at this concentration regime have provided no evidence of strong chain-chain associations, but rather an entanglement coupling behavior, typical of a temporary polymer network [25, 44]. However, HA has been shown to form aggregates in highly crowded biological environments, as when confined in intercellular [44] or intracellular [37] spaces. The aim of this paper was thus to illustrate how the structural features of HA could be affected when studied under high concentration conditions *in vitro*, which would have great significance for the understanding of biological phenomena occurring in constricted environments *in vivo*. This was accomplished by means of techniques enabling the investigation of both macroscopic (by viscosity, calorimetric and polarized-light microscopy measurements) and molecular properties (by FTIR spectroscopy).

**Falling Ball. Fig. 2.17** shows a selection of representative results of the FB experiment performed on HA samples. Results obtained from up to 50-mg/ml-concentrated samples displayed a nearly monotonic decrease in viscosity at increasing temperature. A similar trend had been previously reported and attributed to a decrease in the persistence length due to a greater freedom of rotation around the glycoside bonds or to an increased population of high energy conformers at increasing temperature [24, 46]. At higher concentration values, a more abrupt change in viscosity was detected. For example, when considering the 100 mg/ml sample, we observed that the solution started to soften at ~35 °C and became fluid at around ~50 °C. The distinct change in the slope of the viscosity observed during the heating of these HA samples can be referred to the loosening of certain cooperative interactions, which are typically found to play a key role in polymer-polymer complexes of polysaccharide systems [47]. Extrapolated lines of the travel distance below and beyond these values furnished a gel-like to fluid-like transition at 40-45 °C, in accordance with previous studies which had ascribed it to a destabilization of a postulated HA supramolecular assembly [17, 36].

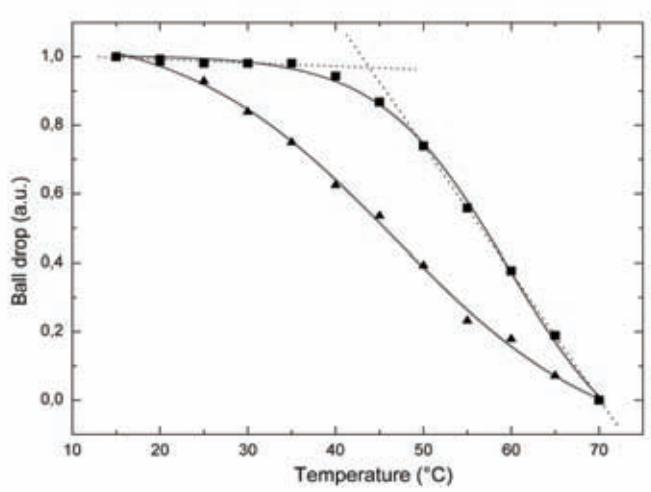


**Fig. 2.17** Normalized falling distance of a 0.5 mm tungsten carbide ball inside a 100 mg/ml (squares), or a 10 mg/ml (triangles) HA solution in physiological saline as a function of the temperature.

**FTIR**. Infra-red spectroscopy can be a powerful tool to obtain structural information on the behavior of water molecules embedded in macromolecules, and, thus, to gain indirect insight into the structure of the latter. The infrared spectrum of HA water solutions was dominated by the broad band relative to the OH stretching of $H_2O$ molecules falling in the 3000-3700 $cm^{-1}$ region (see **Fig. 2.18**), in accordance with previous observations [33-35]. Strong differences in the shape of this band were evident from a comparison of differently-concentrated HA solutions, unequivocally indicating the presence of different structural water environments.

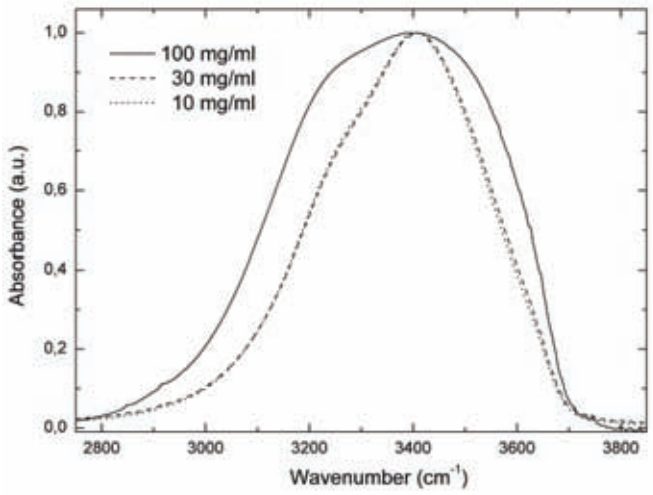


**Fig. 2.18** OH stretching band of various HA concentrations in physiological saline at 20 °C.

A first interesting insight comes from considering the modulation of the peak intensity of the OH-stretching band as a function of the temperature (**Fig. 2.19**). The less concentrated

samples showed a nearly monotone decrement of intensity that can be ascribed to a progressive thinning of the HA film hold between the $CaF_2$ windows, caused by a monotone change of fluidity of the HA solution, as previously observed from FB measurements (compare **Fig. 2.19B** with **Fig. 2.17**, triangles). On the contrary we observed a sharp change of slope occurring at ca. 35 °C for more concentrated samples (see **Fig. 2.19B**, squares). Indeed, from 15 up to 35 °C thinning is highly inhibited due to the constant viscosity properties (compare with the same range in **Fig. 2.17**, squares). At ~35 °C the thinning is not longer inhibited and starts to affect the absorbance of the peak (see **Fig. 2.19A**), resulting in a constant decreasing trend in the temperature range 35-70 °C. Thus, in this case, we may infer the presence of a HA superstructure that undergoes a transition beyond a characteristic temperature threshold, as already suggested by FB measurements.

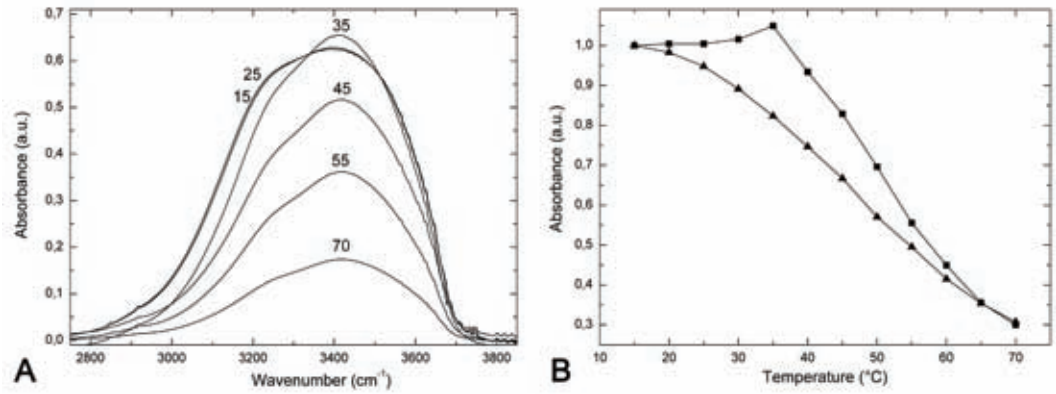


**Fig. 2.19** (A) OH stretching band of 100 mg/ml HA in physiological saline at increasing temperature. (B) Variation of the peak intensity of OH stretching band as a function of the temperature. Squares: 100 mg/ml; triangles: 10 mg/ml.

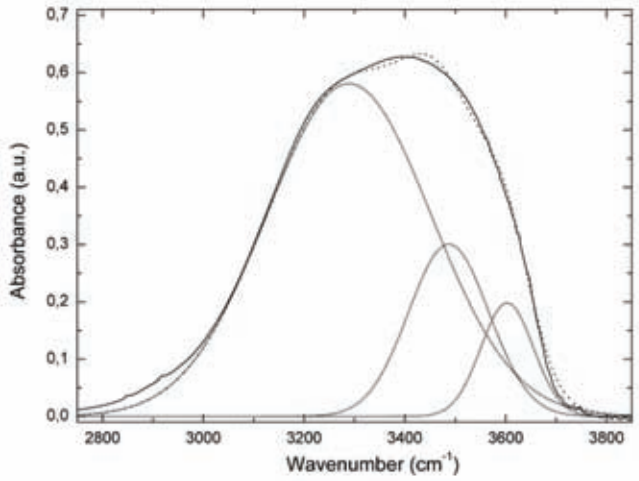


**Fig. 2.20** Gaussian deconvolution of the OH band of 100 mg/ml HA in physiological saline at 20 °C.

In order to qualitatively assess the changes in the OH stretching band arising from an increase in temperature and a variation in concentration, we fitted each spectrum as a sum of three Gaussian curves, in accordance with previous studies [48-50]. An example of fitting is reported in **Fig. 2.20**. Each of the Gaussian curves accounts for different water populations associated with a particular type of hydrogen bond, which have been previously discussed for HA [51]: These are "network water (NW)" molecules, "intermediate water (IW)" molecules, and "multimer water (MW)" molecules. The first type, NW, which is assigned to the lower energy Gaussian curve (~3300 $cm^{-1}$), is assumed to be originated from water molecules involved in transient networks that break and form continuously. These water molecules are most likely to be connected tetrahedrally, almost as in ice, thus generating instantaneous H-bonded low-density pathways, extending over a supramolecular level. The second type of water molecules, IW (centered at ca. 3480 $cm^{-1}$) is ascribed to molecules connected in some way to other water molecules, although unable to develop fully connected patches, and thus, having distorted H-bonds. This component of water has an average degree of connection larger than that of dimers or trimers, but lower than those participating in the percolating networks. The third kind of water molecules, MW (higher energy Gaussian at ~3600 $cm^{-1}$), corresponds to water molecules poorly connected with their environment and standing as free monomers, or as dimers or trimers. The latter assignment is supported by the fact that, frequency wise, these MW molecules are close to those found in the vapor phase, just as the NW Gaussian is positioned at frequency close to that of the OH band in ice.

As water is represented by three different states in the systems (NW, IW, MW), it is reasonable to assume that the total peak area corresponding to the water band is the sum of the peak areas of the different states of water. Thus, we can calculate the fraction of NW, IW, and MW weighted on the total amount of water, and we can plot the variation of the ratio between the area of each Gaussian component ($A_i$) to the total peak area ($A_{tot}$) as a function of the temperature. The $A_i/A_{tot}$ calculated trends relative to these solutions (**Fig. 2.21A,B**) unveiled a different behavior, mainly of the NW and the IW fractions, as a function of either concentration or temperature. Major modifications were observed for the most concentrated samples examined. For example, if we consider the 100 mg/ml HA solution, "network water" passed from 0.75 up to 25 °C to 0.55 beyond 60 °C, while the "intermediate water" varied from 0.20 to 0.40 exactly in the opposite manner. Thus a modification of the water structuring occurred when a certain temperature value, i.e. 25 °C, was reached; then, after a gradual decrease between 25 and 60 °C, a constant trend was maintained despite further heating. Instead, less concentrated HA samples (e.g. 10 and 30 mg/ml) showed slight variations in the NW and IW fractions upon heating, which were mainly centered at around 0.70 and 0.25, respectively. Interestingly, the 100 mg/ml HA

sample showed initial (up to 25 °C) $A_i/A_{tot}$ values of NW and IW more similar to those typically found for the 10 mg/ml than for the 30 mg/ml sample.

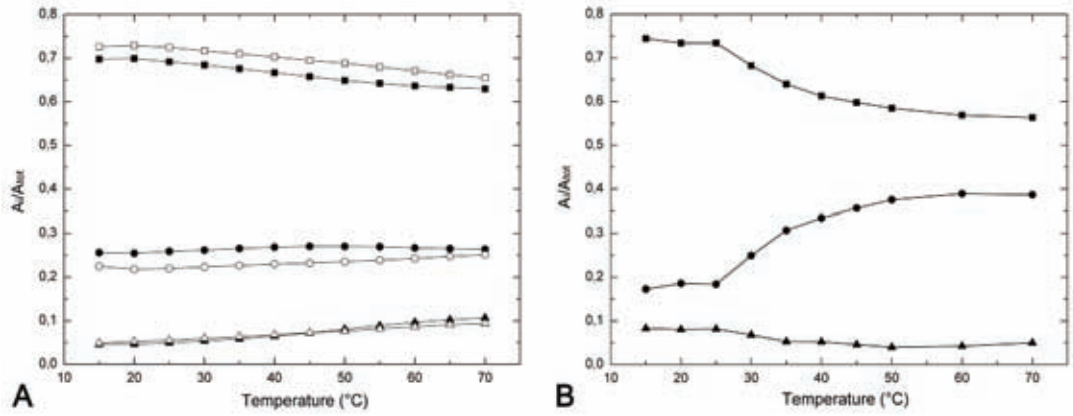


**Fig. 2.21** Ratio of the area of the *i*th Gaussian component ($A_i$) to the total peak area ($A_{tot}$) versus temperature. (A): NW (square), IW (circles), and MW (triangles) fractions of 10 mg/ ml (open) and 30 mg/ml (filled) HA in physiological saline. (B): NW (square), IW (circles), and MW (triangles) fractions of 100 mg/ ml HA in physiological saline.

Semi-diluted HA solutions have been previously shown to form temporary networks, whose average mesh size was predicted to be progressively lower than 20 nm for solutions progressively more concentrated than 10 mg/ml [52-53]. The confinement of water inside low-sized pores can be disadvantageous for the long-distance water connectivities, favoring the more restricted connectivities, as previously reported for water confined in fluorocarbon reverse micelles [49]. Accordingly, in our measurements the 30 mg/ml HA sample showed NW and IW values respectively lower and higher, on average, in comparison with the 10 mg/ml solution, suggesting a moderate effect of confinement. The plot of 100 mg/ml HA sample revealed a different trend. Firstly, it unequivocally showed a transition between two different kinds of water structuring, and thus, of HA. At low temperature, i.e. below 25 °C, NW was favored possibly because of stable associations among HA chains. This allowed the formation of a large-pore-size polymer network (See the scheme proposed in **Fig. 2.22**), which favored the formation of long-distance connectivities of water molecules with respect to small-sized water aggregates. These pores should have a dimension comparable to that of the 10 mg/ml sample, if we consider the similarity of their initial NW values. Beyond 25 °C, the intermolecular interactions are supposed to break progressively leading to a polydisperse entanglement on average more crowded with respect to that of less concentrated solutions, because of the higher local chain density. As a matter of fact, we observed a considerable decrease in NW and, simultaneously, an increase in IW, which are both well in accordance with our hypothesis.

FTIR results pointed out the formation of stable supramolecular assemblies only at the highest concentrations considered. The sharp change in shape of the OH stretching band starting at 25 °C, indicating a transition from a large- to a restricted-connectivity water structuring, suggested a concurrent transition from a stable to a temporary HA network. Furthermore, it is to be noted that the low-temperature threshold supposed to disrupt the network is well in agreement with the occurrence of weak intermolecular associations among the HA chains.

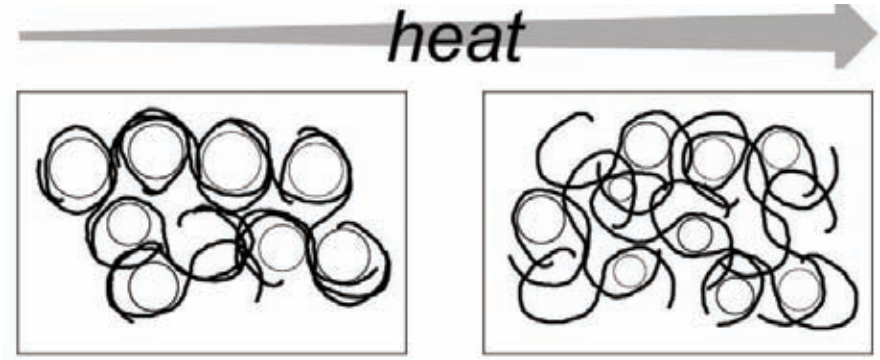


**Fig. 2.22** Proposed scheme of HA network rearrangement (from stable to temporary) during heating.

**DSC.** DSC analysis of highly concentrated HA solutions was performed in order to obtain a quantitative estimate of the structural transition showed by FB and FTIR measurements. **Fig. 2.23** shows a heating curve relative to the 100 mg/ml HA sample acquired at a scanning rate of 5 °C/min. The DSC curve enabled the detection of an exothermic and an endothermic transitions at 25-35 °C and at 45-60 °C, respectively. The latter was ascribed to a gel-like to fluid-like transition. In fact, the onset of this transition is well in accordance with the threshold values characterizing the sharp change in the viscosity properties of concentrated HA samples which were observed above (see **Fig. 2.17** and **Fig. 2.19B**, squares). The exothermic transition starting at 25 °C is not easily ascribable: it may proceed from a transient re-organization of the HA chains stimulated by a rather low temperature regime. Moreover, it appears an integral part of the process leading to the disruption of the HA supramolecular network since it matches the starting temperature of water re-structuring found by FTIR measurements (see **Fig. 2.6B**). Anyway, additional measurements will be carried out in the near future to clarify this picture. The measured enthalpies calculated from the area of the two peaks were of the order of 100-200 cal/mol (referred to a disaccharide unit). These values are quite compatible with weak non-covalent interactions as those characteristic of Van der Waals and hydrophobic forces, which are frequently responsible of the structuring of polysaccharide systems [47].

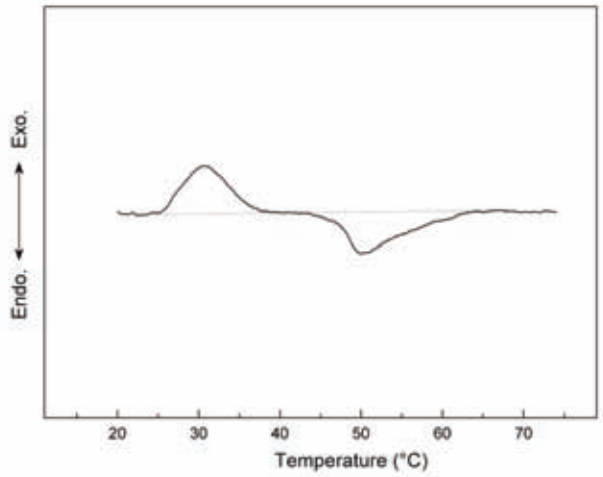


**Fig. 2.23** DSC curve of 100 mg/ml HA in physiological saline recorded at a heating rate of 5 °C/min.

**PLM**. This technique can selectively visualize the birefringence originating from anisotropic structures, which are seen as shining bodies on a dark background. The analyzed samples consisted of thin films of HA solutions in physiologic saline in the 10-100 mg/ml range, obtained by sandwiching a small amount of the sample between a microscope slide and a coverslip previously pre-treated. As mentioned before, the pre-treatment of the microscope glass slides consisted either in creating a hydrophilic or a hydrophobic environment.

Soon after the preparation, all types of films looked homogeneously dark. This indicates the lack of extensive ordered chain-assemblies over the concentration scale examined. During one week of storing at ambient temperature, by following a slight loss of water due to evaporation, the HA depositions on polar glass tended to loss their initial shape assuming ragged edges consisting in honeycomb-like structures (**Fig. 2.24**). In these locations, the HA strands were probably induced to approach themselves, creating a bright and persistent birefringence. On the other hand, HA films deposited within plasticized slides (hydrophobic substrate) reduced slightly in size although conserved linear edges, which lacked any type of birefringence. Similar results were found for all samples considered even if the more the concentration, the less the time required for the development of the birefringence textures (in the hydrophilic environment).

The HA molecule owns hydrophobic groups oriented above and below the average plane of each sugar ring, whereas the hydrophilic groups are displayed around the perimeter of the rings, thus creating relatively hydrophobic and hydrophilic faces, respectively [31]. The existence of such a twofold character can account for the different behavior observed when changing the environment from polar to hydrophobic. HA placed in between hydrophilic surfaces appeared prone to generate ordered assemblies. This is comprehensible if we

consider that HA keeps its hydrophilic faces in contact with the polar surfaces while using its hydrophobic patches to mediate the assembly with the other polymer chains. This observation is thermodynamically explained by an entropically driven process due to water molecules initially bound to the polymer and then freed by the association of approaching polymer segments [15], which is even more favored during water loss process. The observed local ordered assemblies can thus be interpreted as the result of the generation of favorable interactions among the HA chains, probably induced by a hydrophobic effect. On the other hand, the lack of birefringence observed in the HA samples sandwiched between plasticized surfaces can be interpreted in accordance with a moderate affinity for this environment, ascribable to the non-polar groups of the polymer. The preferential interaction of the hydrophobic patches with the plasticized substrate probably inhibited the possibility to employ them for the generation of extended ordered assemblies. Similar results have been recently obtained by Cowman and co-workers by means of atomic force microscopy [54]. They showed that HA deposited on mica (hydrophilic) tended to frequently generate intermolecular associations, as opposed to when a graphite substrate (hydrophobic) was used.

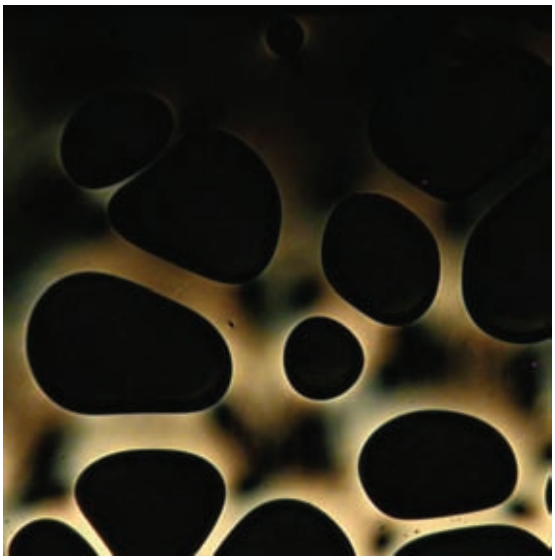

**Fig. 2.24** PLM image of a HA sample (100 mg/ml) in physiological saline sandwiched between polar microscope slides and after one week of storing at room temperature.

In comparison to aged HA films spread on a polar glass, HA in concentrated solutions is expected to generate looser networks mediated by restricted junction zones (which are replaced by dynamic entanglements under a lower concentration regime). These junction zones, under certain perturbing conditions such as those carried out in this experiment, are encouraged to develop into more extended and stiffened intermolecular associations, which were actually detected by our PLM imaging. With this assumption, we can ascribe to hydrophobic interactions also the self-associations operating in stable HA networks in

solutions, which, in addition, agree with the low enthalpy values obtained from the DSC analysis.

### 2.3.4 Conclusions

The multifaceted analysis that we carried out enabled us to bring to light the ability of HA solutions in physiological saline to generate stable superstructures under high concentration conditions. FB and FTIR measurements of the less concentrated HA samples suggested the presence of a temporary polymer network, in which the overlapping of individual HA domains did not lead to stable interactions. By increasing the concentration, the crowded local environment was supposed to promote the association of HA chains one to another. FB and FTIR analyses of highly concentrated HA solutions revealed the presence of stable polymer networks, which dissolved upon heating. DSC underlined the existence of a gel-like to fluid-like transition, while it excluded any involvement of strong intermolecular interactions. PLM suggested that chain-chain associations were driven by hydrophobic interactions, which is essentially compatible with the low enthalpy values obtained from DSC analysis. Thus, we can hypothesize a switching from temporary to stable HA networks as a function of the concentration. The latter probably originated from the formation of junction zones mediated by hydrophobic interactions.

In physiological compartments the presence of a high number of macromolecules makes the space highly crowded. In practice this leads to the enhancement of the “effective” concentration of the individual macromolecules [39]. The intermolecular associations of highly concentrated HA solutions can be viewed as a strategy of the system to reduce its free energy by maximizing the available volume (and minimizing the excluded volume), as normally observed in living systems [40]. On the basis of the results presented here, we would like to underline the importance of taking into account the “effective” macromolecular concentration within future studies dealing with the structuring of HA and of other glycosaminoglycans in physiological conditions. Furthermore, at this concentration also the biological activity of the polymer could be partially altered, which is actually an issue usually neglected in the case of more diluted solutions.

### 2.3.5 Involvement of proteoglycans in the mechanism of laser tissue welding

A similar picture can be hypothesized for the interfibrillar PGs of corneal stroma (and, likely, of other soft-fibrous connective tissues). In fact this biological environment is highly crowded by macromolecular species, mainly collagen fibrils and PGs themselves, as nicely depicted by the following model recently proposed by Müller and co-workers [55] (**Fig. 2.25**):

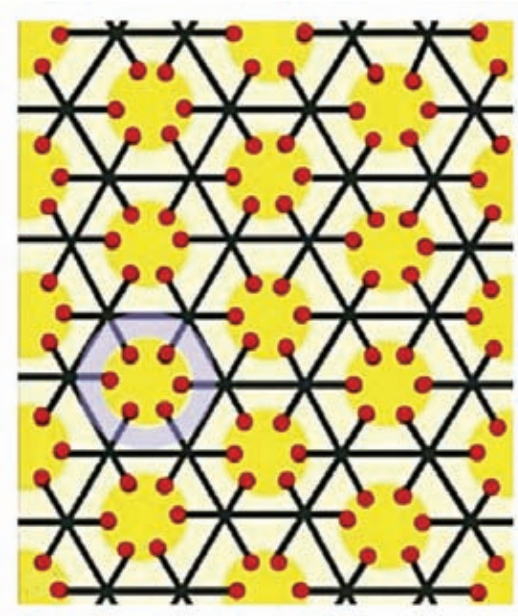

**Fig. 2.25**. Schematic visualization of stromal organization as proposed by Müller. Hexagonal arranged collagen fibrils are interconnected at regular distances with their next nearest neighbors by groups of six PGs, attached orthogonally to the circumference of the fibrils. In this way a regular meshwork of ring-like (intermediate between hexagonal and circular) 11 nm thick structures (bluish) enwrapping the collagen fibrils is formed. (from [55]).

In this model, at equidistant sites along their circumferences, six core proteins of PGs are attached to the hexagonal arranged collagen fibrils. The GAG chains of PGs join next nearest neighbor collagen fibrils and form a ring-like structure around each collagen fibril of approximately 11 nm in thickness (i.e. a gel-like shell surrounding individual collagen fibrils). The article from Müller et al. [55] furnishes also quantitative parameters of PGs and collagen fibrils in the stromal cornea, achieved by electron microscopy analysis. These are reported in **Table 2.2** and used for the following calculations:

| | | |
|---|---|---|
| Diameter of ring-like structures | 45·0 ± 4·2 nm | (~45 nm) |
| Thickness of PGs | 10·5 ± 1·7 nm | (~11 nm) |
| Length of PGs | 53·9 ± 5·4 nm | (~54 nm) |
| Diameter of collagen fibrils | 22·7 ± 1·8 nm | (~23 nm) |
| Distance between adjacent collagen fibrils | | (~43 nm) |

**Table 2.2** Quantitative parameters of proteoglycans and collagen fibrils in the human cornea (from [55]).

We can tentatively try to calculate the effective concentration of the PG component within the corneal stroma taking into account of the space occupied (and thus subtracted) by the main extracellular stromal macromolecules (fibrillar collagen and PGs themselves).

Corneal stroma is composed by 78 % of water, 15 % of collagen, 1 % of PGs, and 5 % of other components (% is expressed in weight/weight). Considering the density of corneal stroma equal to 1 g/ml (the exact value is 1.062 g/ml [56]), we can estimate a concentration of stromal PGs of about 10 mg/ml (that we call "apparent concentration").

Let's consider a volume inside the stroma of 54 nm (in length) × 43 nm (in width) × 100 nm (in height) = (232 $\cdot 10^3$) $nm^3$, that we call the "apparent volume", where the length is equal to that of each individual PG (along the X-axis), the width is the interfibrillar distance (along the Y-axis) and the height is arbitrarily chosen (along the Z-axis) (see the scheme of **Fig. 2.26**). Inside the considered area of (54 x 43) $nm^2$ on the XY plane, two half ring-like structures (two semicircles of 795.2 $nm^2$ area) plus two other fractions of ring-like structures (two circular segments of 236.5 $nm^2$ area) are present. These correspond to a total occupied volume of [(795.2 x 236.5)x2] x 100 = (206 $\cdot 10^3$) $nm^3$, which represents the total "excluded volume". Thus, the "effective volume" is (26 $\cdot 10^3$) $nm^3$, which represents about 10 % of the "apparent volume". We can thus estimate that the "effective PGs concentration" in corneal stroma is 10 times higher than the "apparent concentration", that is ~100mg/ml. This is in accordance with the concentration value at which the model GAG hyaluronan has been proved to aggregate (see §2.3.3). We may note the this is a very rough estimation which, among others, does not take into account for the electrostatic repulsion between neighbor PGs and the interaction of each core PG protein with the collagen fibril or other extracellular components, which both can alter the aggregation process.

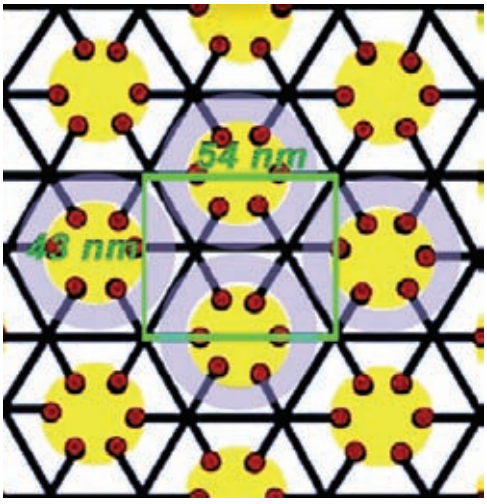


**Fig. 2.26** Calculation of effective stromal PG concentration. We consider a (54 × 43 × 100) $nm^3$ volume (the green square defines the (54 × 43) $nm^2$ area laying on the XY plane) of corneal stroma. Excluded areas are represented by ring-like structures (bluish) surrounding each fibril.

We can thus infer that the Scott's model [1,2], which provides the presence of PG doublets connecting two adjacent fibrils (i.e. aggregates formed by the interaction of two GAG chains), is reasonable for the corneal stroma in physiological conditions. It is worth noting that this is true if we extend the results found for the archetypal GAG (hyaluronan) studied in crowded *in vitro* environments to the corneal GAGs *in vivo*. Thus, we ought to point out that this conclusion can be intrinsically subjected to some fault.

From the same extension (of the HA behavior to that of the other GAGs), we can conclude that, by heating aggregated corneal PGs beyond the temperature threshold of ~60 °C, a reversible disaggregation of the GAG chains should occur.

Another expected effect of the temperature rise is the denaturation of the protein core of the PGs, which could lead to suspect a possible separation of the PGs from the fibrils during heating. Thermal denaturation of the PG core was previously investigated by P.G. Scott [57, 58]. He proved that thermal denaturation of small PGs, in particular of decorin, actually occurs at a low temperature (i.e. at around 45 °C), but this does not affect the linkage between the protein core of the PGs and the collagen fibril. The solely addition of a chemical denaturant was associated with the breakage of the PG-collagen bond.

Hence, considering the results obtained from microscopy analyses of welded corneas, from chemical analyses of the model GAG hyaluronan in crowded environments and from the considerations on proteoglycans aggregates we made above, we can tentatively hypothesize a model of the corneal welding process taking place at the typical low powers of diode laser irradiation. The GAGs bridges connecting collagen fibrils in native stroma are probably broken at the characteristic temperatures of diode laser welding (55-65 °C range), as suggested by our results. The individual GAG strands, freed upon heating, could successively create new bonds with other free strands during the cooling phase. In practice, a number of disaggregated PGs of one side of the wound could interact with other PGs of the other side generating new bonds, which are probably of non-covalent nature (maybe, hydrophobic). The weld is hold by groups of interwoven fibrils joining the sides of the cut as shown by microscopy data. The interwoven fibrils are supposed to be connected by several newly-formed GAG bridges. A scheme of the proposed mechanism of laser welding is reported in **Fig. 2.27.**

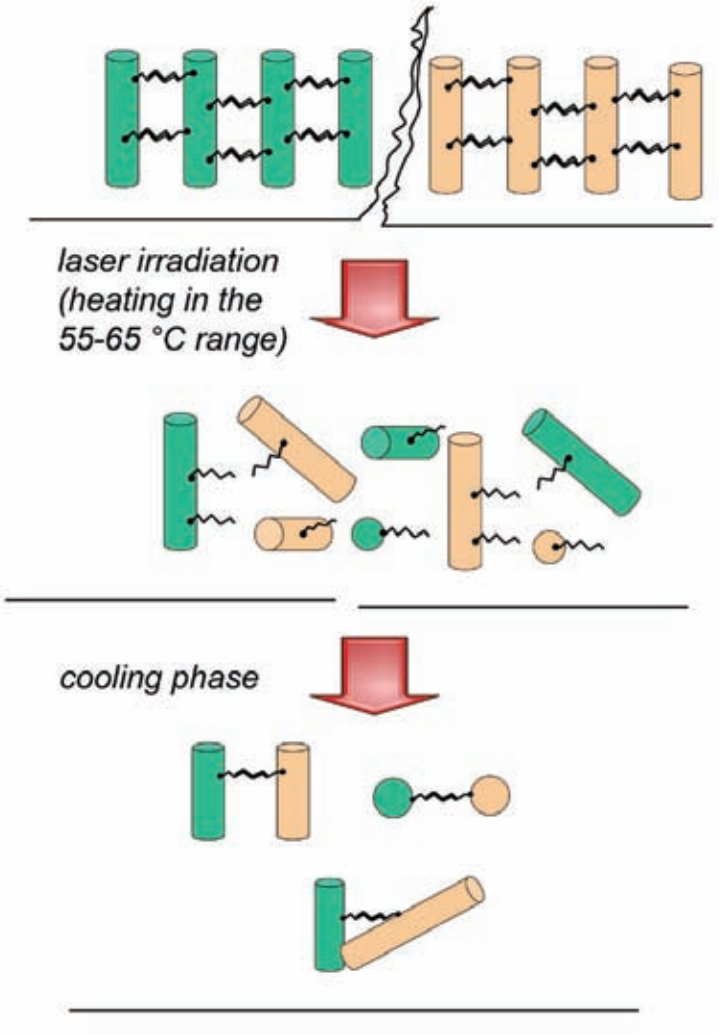


**Fig. 2.27** Proposed scheme of laser welding of corneal stroma. During the laser irradiation a local heating in the 55-65 °C range is induced. This leads to the disruption of GAGs aggregates (doublets) of the two side of the wound to be welded and thus to a fibrillar rearrangement. During the cooling phase, GAG strands freed upon heating may interact with each other generating new bonds between the fibrils at the two sides of the cut and thus originating the weld.

## References

1. J. E Scott: FASEB J. 6, 2638 (1992)
2. J. E. Scott: J. Anat. 187, 259 (1995)
3. P. Gagneux and A. Varki: Glycobiology 9, 747 (1999)
4. E.F. Hounsell: Structural and conformational analysis of keratan sulphate oligosaccharides and related charbohydrate structures. In: Keratan sulphate chemistry, biology, chemical pathology, ed by H. Greiling and J.E. Scott (The Biochemical Society, London, 1989) pp 12-15
5. H. Moulabbi, H. Broch, et al.: Theochem. 395-396, 477 (1997)
6. J. E. Scott, and M. J. Tigwell: Biochem. J. 173, 103 (1978)
7. B. Casu, M. Petitou, et al.: Trends Biochem. Sci. 13, 221 (1988)
8. L-A. Fransson, L. Cöster, et al.: J. Biol. Chem. 257, 6333 (1982)
9. M. Hirsch, G. Prenant, and G. Renard: Exp. Eye Res. 72, 123 (2001)
10. N. Uldbjerg and C.C. Danielsen: Biochem. J. 251, 643 (1988)
11. J. E. Scott: J. Physiol. 553, 335 (2003)
12. J. E. Scott and A. M. Thomlinson: J. Anat. 192, 391 (1998)
13. L. J. Lapcík, L. Lapcík, et al.: Chem. Rev. 98, 2663 (1998)
14. A. J. Day and J.K. Sheehan: Curr. Opin. Struct. Biol. 11, 617 (2001)

15. M. K Cowman and S.Matsuoka: Carbohydr. Res. 340, 791 (2005)
16. K. Hayashi, K. Tsutsumi, et al.: Macromolecules 28, 3824 (1995)
17. E. R. Morris, D. A. Rees and E. J. Welsh: J. Mol. Biol. 138, 383 (1980)
18. J. E. Scott, F. Heatley, et al.: Biochem. J. 199, 829 (1981)
19. A. Almond, J.K. Sheehan and A. Brass: Glycobiology 7, 597 (1997)
20. A. Almond, A. Brass, and J.K. Sheehan: Glycobiology 8, 973 (1998)
21. A. Almond, A. Brass, and J.K. Sheehan: J. Phys. Chem. B 104, 5634 (2000)
22. M. K. Cowman, J. Feder-Davis and D.M. Hittner: Macromolecules 34, 110 (2001)
23. A. Almond, P.L. Deangelis, C.D. Blundell: J. Mol. Biol. 358, 1256 (2006)
24. E. Fouissac, M. Milas and M. Rinaudo: Macromolecules 26, 6945 (1993)
25. P. Gribbon, B.C. Heng and T.E. Hardingham: Biophys. J., 1999, 77, 2210-2216.
26. R. E. Turner, P.Y. Lin and M.K. Cowman: Arch. Biochem. Biophys. 265, 484 (1988)
27. M. K. Cowman, J. Liu, M. Li, et al.: In The Chemistry, Biology, and Medical Applications of Hyaluronan and Its Derivatives, ed. by Laurent, T. C., Portland Press: London, 1998 pp 17-24.
28. M. K. Cowman, M. Li and E.A. Balazs: Biophys. J., 75, 2030 (1998)
29. M.K. Cowman, C. Spagnoli, et al.: Biophys. J. 88, 590 (2005)
30. J. E. Scott, M. Cummings, et al.: Biochem. J., 274, 699 (1991)
31. J. E. Scott and F. Heatley: Proc. Natl. Acad. Sci. U. S. A. 96, 4850 (1999)
32. J. E. Scott and F. Heatley: Biomacromolecules 3, 547 (2002)
33. K. Haxaire, Y. Maréchal, et al.: Biopolymers 72, 10 (2003)
34. K. Haxaire, Y. Maréchal, et al.: Biopolymers 72, 149 (2003)
35. Y. Maréchal, M. Milas and M. Rinaudo: Biopolymers 72, 162 (2003)
36. M. I. Giannotti, M. Rinaudo and G.J. Vancso: Biomacromolecules 8, 2648 (2007)
37. S. P. Evanko, W.T. Parks, et al.: Histochem. Cytochem. 52, 1525 (2004)
38. S. P. Evanko, M.I. Tammi and T.N. Wight: Adv. Drug Deliv. Rev. 59, 1351 (2007)
39. G. Rivas, F. Ferrone and J. Herzfeld: EMBO Rep. 5, 23 (2004)
40. A. P. Minton:. J. Biol. Chem. 276, 10577 (2001)
41. W. E. Krause, E.G. Bellomo and R.H. Colby: Biomacromolecules 2, 65 (2001)
42. B. H. Min, J.Y. Lee, et al.: In Hyaluronan, structure, metabolism, biological activities, therapeutic applications, ed.; Balazs, E. A.; Hascall, V. C., Matrix Biology Institute: Edgewater, New Jersey, USA, 2005 pp 55-59
43. M. Takahashi, T. Hatakeyama and H. Hatakeyama: Carbohyd. Polym. 41, 91 (2000)
44. C. D. Blundell, P.L. Deangelis and A. Almond: Biochem. J. 396, 487 (2006)
45. J. E. Scott, A.M. Thomlinson and P. Prehm: Exp. Cell. Res. 285, 1 (2003)
46. R. L. Cleland: Biopolymers 18, 1821 (1979)
47. M. Rinaudo: Macromol. Biosci. 6, 590 (2006)
48. G. Onori and A.J. Santucci: J. Phys. Chem.: 97, 5430 (1993)
49. L. Dei and S. Grassi: J. Phys. Chem. B 110, 12191 (2006)
50. J.-B. Brubach, A. Mermet, et al.: J. Phys. Chem. B, 105, 430 (2001)
51. J. Liu and M.K. Cowman: J. Thermal Anal. Calorimetry 59, 547 (2000)
52. S. C. De Smedt, A. Lauwers, et al.: Macromolecules 27, 141 (1994)
53. T. E. Hardingham: In Hyaluronan, structure, metabolism, biological activities, therapeutic applications; Balazs, E. A.; Hascall, V. C., Eds., Matrix Biology Institute: Edgewater, New Jersey, USA, 2005, pp 67
54. C. Spagnoli, A. Korniakov, et al.: Carbohyd. Res. 340, 929 (2003)
55. L. J. Müller, E. Pels, et al.: Exp. Eye Res. 78, 493 (2004)
56. J. Kampmeier, B. Radt, et al.: Cornea 19, 355 (2000)
57. P. G. Scott: Biochem. Soc. Trans. 19, 3776 (1991)
58. P. G. Scott: Biochem. Biophys. Res. Comm.: 138, 3 (1986)

## 2.4 - PERSPECTIVES

Future investigations on the mechanism of laser welding should follow a twofold approach. From one side, it is necessary to carry out a more detailed analysis in order to prove the feasibility of self-assembly, and mainly of duplexing, of the small PGs of corneal stroma. This could be achieved mainly by means of calorimetric and spectroscopic methods, as we employed for the hyaluronan molecule. However, this investigation may bring a number of concerns. The low availability of commercial PGs and, overall, the lack of commercial PGs from corneal stroma, necessarily requires the extraction of PGs directly from corneal tissue. Extraction protocols of stromal PGs were previously proposed, even if they are troublesome in obtaining a highly-purified product on the microgram scale which is needed to prove the aggregating tendency of PGs. A more feasible strategy is to extract only the GAG part of PGs, which is obtained following simpler protocols. Furthermore, more convincing data are expected in this case due to the lack of the proteic component (PG core) that could strongly affect the results.

On the other side, a non-traditional electron histochemistry approach could be tried, based on staining protocols specifically used for the PGs detection. This, in principle, could lead to a better picture of the final architecture of PG molecules after laser welding. However, a microscopy analysis based on non-traditional electron histochemistry (as the specific methods for PG detection, see e.g. **Fig. 2.15**) is very time and skill demanding. Moreover, it is probably subjected to fail in the case of our welded samples because of the wide usage of more invasive protocols in respect with those normally employed. These could strongly affect the local stromal architecture, thus compromising the detection of the original distribution and assembly of the PGs at the weld site.

# 3. OPTIMIZATION OF LASER WELDING (Part I)

## Setup of noninvasive imaging systems to investigate (photo)thermally-induced changes in corneal collagen

*Here the second topic of this thesis dealing with the optimization of laser welding technique is introduced. With regard to this topic, our work was aimed at pursuing two distinct objectives, which thus cover two distinct chapters of the thesis (Part I & 2). The first part deals with the work done to assess the feasibility of two imaging techniques, namely fluorescence and second-harmonic generation, to monitor photothermally- and thermally-induced changes in biological tissue, with particular regard to cornea. The second part is devoted to present new nanostructured chromophores: in particular the enhanced capability of suitably synthesized gold nanoparticels to generate consistent photothermal effects when used as laser-absorbers in tissues are discussed.*

*The following chapter starts with an introduction to the problem of investigating and monitoring the structural changes that may occur to the main components of biological tissues when subjected to (photo)thermal therapy (§3.1). The rest of the chapter is devoted to describe the solutions proposed in this thesis to this problem, which rely on the use of fluorescence imaging (§3.2) and second harmonic generation imaging (§3.3).*

## 3.1 - BACKGROUND

*This section provides an overlook of the therapeutical applications based on the induction of thermal and photothermal effects (i.e. thermal effects induced by the conversion of the absorbed light into heat). Then a brief description of the most popular analytical methods used to characterize the structural changes induced in connective tissues and in particular on cornea is reported.*

Thermal therapies are increasingly used in clinical practice for the treatment of diseases and injuries. The heating devices employed are based principally on the use of laser irradiation, radiofrequency electrical current, or microwaves. Heat-induced effects have been exploited for instance in dermatology, for skin rejuvenation and resurfacing or for the treatment of cutaneous vascular lesions [1]; in orthopedics, for the thermal treatment of shoulder instability [2]. In ophthalmology an increasingly number of medical procedures are based on the application of heat and more commonly on the generation of photothermal processes mediated by laser. For example, heat-induced effects have been exploited for refractive surgery using PRK or LASIK techniques, for reshaping of corneal curvature in laser thermokeratoplasty, for the closure of corneal wounds with minimally invasive laser welding (as we have seen in the previous chapters) [3]. The ability to monitor quali-quantitatively the structural changes to the tissue is of utmost importance in controlling the heating effect induced, in assessing the quality of surgical intervention and in preventing undesiderable thermal damage to the peripheral structures.

Structural changes in connective tissue resulting from therapeutic thermal treatments are primarily imputable to collagen. This protein is the most abundant one in the body and the main component of connective tissues. Collagen molecule has a triple helix composed of polypeptide chains highly stabilized by interconnecting hydrogen bonds. Within the collagen family, the main component of fibril-forming collagens is type I collagen, which provides the structural and organizational framework for skin, blood vessels, bone, tendon, cornea and other tissues. In this type of collagens, molecules are packed in a quarter-staggered manner and connected by covalent bonds to form microfibrils few nanometers in diameter, which then combine to form collagen fibrils that are a few to hundred nanometers in size. Some tissue are characterized by two to three hierarchical levels of organization at progressively larger scales, beyond the fibrils. For example in tendon they organize in 1-10 μm thick fibers which in turn form bundles of fibers called fascicles. In corneal stroma, collagen fibrils have uniform diameter and associate which each other to form 1-2 μm sheets known as lamellae. Intralamellar domains are characterized by a regular spacing of

collagen fibrils, which are responsible to the unique physical property of cornea, that is transparency.

When corneal stroma is subjected to a temperature rising, several morphological changes occur to its lamellar domains [3], strictly related to as much ultrastructural modifications in extracellular matrix components, that is ground substance, mainly constituted of proteoglycans, and fibrillar collagen. The first step is ruled out by the denaturation of the ground substance mainly occurring before the onset of fibrillar collagen denaturation, i.e. from ~45 to ~60 °C . In this range one or two subsequent phase transitions are observed which are correlated to a local disorder of the lamellar arrangement. Likely, this is ascribable to the breaking of interfibrillar proteoglycans bridges (discussed in §2), which leads to loss of the regular interfibrillar spaces. The next stage relies on the helix-coil transition of collagen molecule which precedes in two following steps. At first, unwinding of the triple helices occurs due to the hydrolysis of the intramolecular hydrogen bonds. This leads to tissue shortening due to a shrinkage effect parallel to the axis of the fibril. As a consequence, fibrillar edges appear frayed and the fibrillar diameter increases. At higher temperatures covalent cross-links connecting collagen strands break, resulting in a complete destruction of the fibrillar structure and causing full denaturation of collagen and relaxation of the tissue. A schematic representation of the structural modifications occurring in collagen fibrils of corneal stroma upon heating above physiologic temperature is reported in **Fig. 3.1**.

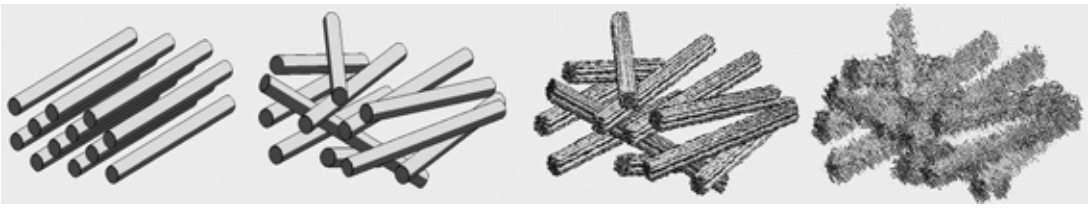

**Fig. 3.1.** Thermal transitions of corneal stroma from the collagen point of view. Native stroma is characterized by a regular arrangement of collagen fibrils. The first step leads to a progressive fibrillar disorganization, ascribed to the breaking of proteoglycan bridges connecting collagen fibrils together. At higher temperatures fibrillar collagen is denatured during two following steps: in the first, intramolecular H-bonds break leading to the a moderate thickening of the fibrillar size and to the appearance of frayed fibrillar edges; in the last step, covalent cross-links connecting collagen molecules together break, causing the complete denaturation of collagen (also called gelatinization or hyalinosis).

Several techniques have been employed to characterize thermal modifications of collagenous tissue. Calorimetric studies have typically been conducted using Differential Scanning Calorimetry (DSC). This method makes it possible to characterize the thermodynamic behavior of many connective tissues, which then show substantial

improvement compared to the use of other previously-adopted approaches [4-7]. On the other hand, histological techniques (e.g. histological staining and immuno-fluorescent labeling) remain the most commonly-used imaging platform, due to their relative ease of use [8-10]. Transmission Electron Microscopy (TEM) is used when high resolution is required [8,10], but it involves high costs as well as complex protocols for specimen processing. Although DSC and the afore-mentioned microscopy techniques may be very useful when used on tissue *ex vivo*, they are unsuitable for monitoring heat-induced changes *in vivo*.

For this reason, we were aimed at exploring the feasibility of two imaging techniques traditionally employed for laboratory investigations, which are potentially adaptable to be employed as *in vivo* diagnostic tools. These are one-photon fluorescence microscopy (simply referred to as "fluorescence microscopy" in the text) and second harmonic generation (SHG) microscopy. The following sections reports on the preliminary studies performed during this thesis in order to evaluate the applicability of these techniques as real-time controlling systems for surgical applications based on induced thermal and photothermal effects.

## References

1. K. Suthamjariya and R. Rox Anderson: Laser in dermatology. In: Biomedical Photonics Handbook, ed by T. Vo-Dinh (CRC Press, 2003), pp. 40/1-40/40
2. A.L. Wallace, R.M. Hollinshead, and C.B. Franck: J. Shoulder Elbow Surg. 9, 354 (2000)
3. M. N. Asiyo-Vogel: "Methods for the analysis of thermal denaturation of corneal collagen in refractive laser surgery" Doctorial Thesis (1998), Faculty of Medicine, University of Lubeck, Germany
4. J. Kampmeier, B. Radt, et al.: Cornea 19, 355 (2000)
5. C.A. Miles, T.V. Burjanadze, and A.J. Bailey: J. Mol. Biol. 245, 437 (1995)
6. F. Flandin, C. Buffevant, and D. Herbage: Biochim. Biophys. Acta **791**, 205 (1984)
7. P. Kronick, B. Maleeff, and R. Carroll: Connect. Tissue Res. **18**, 123 (1988)
8. R. Agah, J.A. Pearce, et al.: Lasers Surg. Med. **15**, 176 (1994)
9. A.D. Zweig, B. Meierhofer, et al.: Lasers Surg. Med. **10**, 262 (1990)
10. T. Tanaka, S. Furutani-Miura, et al.: Jpn. J. Ophthalmol. **44**, 482 (2000)

# 3.2 - FLUORESCENCE IMAGING

*In this section the use of fluorescence micro-imaging analysis for monitoring thermally-induced phase transitions in corneal tissue is proposed. Tissue samples were heated in a water bath at temperatures in the 35-90 °C range. Fluorescence images of the structural modifications induced in corneal stroma were acquired after staining with Indocyanine Green. Discrete Fourier Transform and entropy analyses of each image made it possible to characterize the thermally-induced phase transitions in the stroma, and to indicate a threshold value for severe thermal damage. The procedure could be proposed as the basis for a real-time monitoring system for photothermal therapies.*
*The image processing algorithms were developed in collaboration with Dr. Francesca Rossi of IFAC-CNR of Florence and with the group of Prof. Nesi of the Department of Systems and Informatics, University of Florence.*

### 3.2.1 Introduction

This section presents an imaging system for monitoring thermally-induced phase transitions in corneal tissue. The procedure is based on the use of fluorescence micro-imaging analysis of ICG-stained tissues (**Fig. 3.2**). ICG allows for a homogeneous and unspecifical staining of the tissue, thus providing a bright fluorescence emission from the entire structure of the sample. (It is worth noting that unstained corneal stroma lacks a strong autofluorescence signal, making challenging its detection.) ICG was chosen because its photophysical properties are well-known [1], and because of its low toxicity and use in common practice in medical diagnostics and surgery [2-5]. Specifically, it has been proposed as a effective optical absorber in several applications of laser welding techniques (see [6,7] and §1 and §2 of this thesis). If simple analysis of the stained tissue during treatment has to be performed, it will be possible to characterize the phase transitions of the tissue. The proposed technique could thus be useful as an alternative, low-cost micro-imaging analysis for controlling thermal structural modifications in connective tissues.

### 3.2.2. Experimental procedure

#### 3.2.2.1 Heat bath treatment

Sixty-three freshly-enucleated, intact porcine eyes were used (mean age of the animals: 9-11 months). The entire corneas were extracted, and their transparency and integrity were

controlled prior to being used in the tests. The samples were stored in BSS buffer at room temperature for less then 6 hours. Each sample was then immersed in a water bath for five minutes. This treatment time ensured that thermal equilibrium was reached [8]. A heating immersion circulator (mod. ED, Julabo Labortechnik GmbH, Seelbach, Germany) with ±0.03 °C temperature stability and a reading error of ±0.1 °C was used to heat the water bath. The temperature values studied were in the range of interest for medical applications: namely, the values 35, 40, 45, 47, 50, 53, 55, 56, 57, 58, 59, 60, 61, 62, 63, 66, 68, 71, 74, 77, 90 °C were tested. Three different corneas were heated at each temperature, in order to give statistical significance to the study. After immersion in the water bath, the samples were stored in formalin until micro-imaging was performed.

#### 3.2.2.2 Image acquisition

Cornea samples were sliced in 200-µm-thick cross-sections, which were stained with a 0.5% (w/w) water solution of Indocyanine Green (IC-GREEN, Akorn, Buffalo Grove, IL) over a 4-minute period. The absorbance spectrum of a ICG-stained corneal stroma is depicted in **Fig. 3.2.** The slices were briefly rinsed in water and then mounted on microscope glass slides. All measurements were performed using an inverted epi-fluorescence microscope (Diaphot Nikon, Tokyo, Japan) equipped with a high-pressure mercury lamp (HBO 100 W, Osram, Augsberg, Germany) as the light source. The excitation wavelengths were selected using 10-nm bandwidth interference filters (436FS10-25, Andover Corporation, Salem, NH, USA) coupled to a dichroic mirror (ND510 Diaphot Nikon). Fluorescence images were acquired using a slow-scan cooled CCD camera (Chroma CX260, DTA, Cascina, Italy) equipped with a 512×512 pixel detector (KAF261E, Kodak, Heidelberg, Germany). The thermally-induced modifications to the corneal specimens were evaluated using fluorescence images acquired with a NIR long wave pass filter (800FH90-25, Andover Corporation).

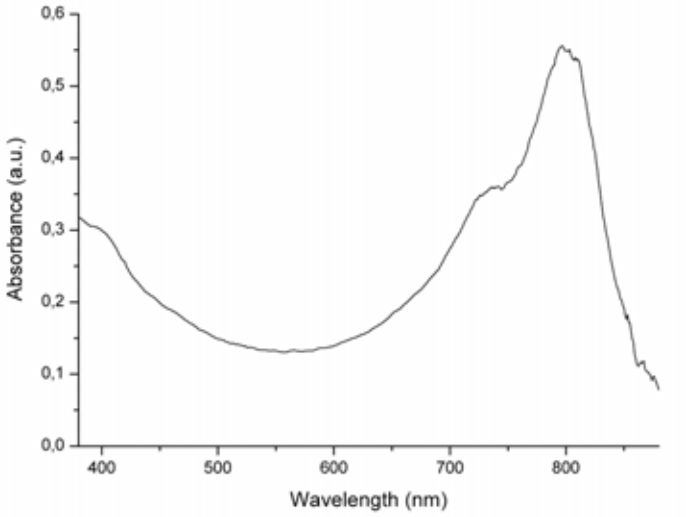


**Fig. 3.2** Absorbance spectrum of ICG-stained corneal stroma.

### 3.2.2.3 Micro-imaging analysis

Micro-imaging analysis was performed by means of two image processing methods: the image entropy and the two-dimensional Discrete Fourier Transform (2D DFT) [9]. The entropy is a statistical index widely used in the field of information theory to express the information content of a message. It is used as a measure of redundancy in an information source. When applied to an image with a regularly repeated pattern, as the lamellar planes in a corneal stroma, a high value in image entropy means a high level in regular organization, while a low value may be related to a reduction of the number of planes visualized in the image, i.e. caused by a homogenization of the tissue. When applied in image processing, the classical entropy definition does not take into account of the spatial properties of the image. To circumvent this limitation, the 2D DFT was used to assess the geometric characteristics of the acquired image. The 2D DFT is a mathematical transformation of an image: the usual spatial domain representation is a function of two spatial variables, $f(x,y)$, indicating the intensity of the image at a particular point $(x,y)$. The Fourier transform is the frequency domain representation of an image as a sum of complex exponentials of varying magnitudes, frequencies, and phases. In the frequency domain, an edge (i.e. a line separating one region from another) is composed of a wide range of frequency components: the frequency distribution of the transformed image can be analyzed to approach the problem of finding the distribution of image lines direction and then to identify the geometry of the image textures. In particular, when considering a pattern of horizontal lines, as in the corneal stroma, the frequency distribution shape is an ellipse oriented along the orthogonal axis; in event of random patterns, instead, the distribution contains contributions due to all the directions, and the shape tends to be circular. For these reasons, the corneal stroma image spectrum was considered for further evaluation on stromal structural modifications.

Next the DFT magnitude was thresholded to levels 0 or 1, and the degree of deformation was quantitatively calculated using the ratio between the width (taken at 70% level) of the horizontal to the vertical histograms (H/V). The H/V parameter was plotted and compared with the shrinkage of the corneal stroma, which was expressed as $\Delta\text{thickness}^{-0.5}$ (in fact a change in $\text{thickness}^{-0.5}$ is proportional to a change in diameter of the corneal button if the volume remains constant).

Two grey levels images showing a 400×400 μm tissue area were acquired from each cornea sample, in order to visualize both the anterior and posterior corneal stroma. The two methods were then applied, by means of a commercial software image processing tool (Matlab® 7.1, the Mathworks, Natick, MA, USA). The 2D DFT of each image was computed with the proper software function. The DFT is usually defined for a discrete function *f(m,n)* that is nonzero only over the finite region $0 \le m \le M-1$ and $0 \le n \le N-1$. The two-dimensional *MxN* DFT and inverse *MxN* DFT relationships are given by:

$$F(p,q) = \sum_{m=0}^{M-1}\sum_{n=0}^{N-1} f(m,n) e^{-j(2\pi/M)pm} e^{-j(2\pi/N)qn} \qquad \begin{matrix} p = 0,1,\ldots,M-1 \\ q = 0,1,\ldots,N-1 \end{matrix}$$

$$f(m,n) = \frac{1}{MN}\sum_{p=0}^{M-1}\sum_{q=0}^{N-1} F(p,q) e^{j(2\pi/M)pm} e^{j(2\pi/N)qn} \qquad \begin{matrix} m = 0,1,\ldots,M-1 \\ n = 0,1,\ldots,N-1 \end{matrix} \qquad (1)$$

The values F(p,q) are the DFT coefficients of *f(m,n)*. The resulting image spectrum was then shifted so as the zero-frequency component *F(0,0)*, corresponding to the image average brightness, is displayed in the center of the frequency distribution image. Thus, the logarithm of the absolute value of the calculated DFT was then visualized.

The same image source was processed by applying the *edge* function, based on Canny filter, to perform edge detection and extract the spatial distribution of the lamellar planes. The entropy was then evaluated. For an image with *L* grey levels, entropy *E* is a scalar value, defined as:

$$E = -\sum_{k=0}^{L-1} P(g_k)\log(P(g_k)) \qquad (2)$$

where: $P(g_k)$ is the histogram value of the $k$-th grey level $g_k$. A new parameter was defined as the entropy inverse: it was indicated as the Disorganization Parameter (DP = 1/$E$), and it was used to characterize heat-induced phase transitions in the stroma.

### 3.2.3 Results

The fluorescence images of water-bathed corneal samples (**Fig. 3.3**) showed a regular and straight horizontal pattern of lamellar sheets at temperatures in the 35÷50 °C range. An additional increase in temperature (51÷61 °C) evidenced the appearance of cavities between lamellae grouped into separate clusters and lacking regular straightness, while above 56 °C, undulations within the lamellae were progressively formed, rapidly converting into a pronounced banding pattern. From 62 °C the lamellar thickness started to grow and the horizontal patterns began to assume a random distribution in space. In the last temperature range (74÷90 °C), the fluorescence images appeared dazed showing less discernible microscopic features.

The plot of the logarithm of the DFT absolute values evidenced the gradual loss of regular lamellar organization with the heat-treatment. The DFT distribution was prevalently along the vertical axis until the temperature was below 62 °C. When higher values were applied to the tissue, the DFT distribution became uniform and the spectrum assumed a circular form. **Fig. 3.4** shows the comparison between the Fourier spectral shape modifications and the measured shrinkage of the corneal stroma. A significant agreement between the two parameters is evident. The intensity of the entropy was calculated for each image, and the resulting DP was plotted. The results are shown in **Fig. 3.5**, where the calculated mean DP value and the standard error of the mean are reported for each temperature. Five relative maximum peaks are present, corresponding to the temperature values of 45 °C, 53 °C, 57 °C, ~66 °C and ~75 °C.

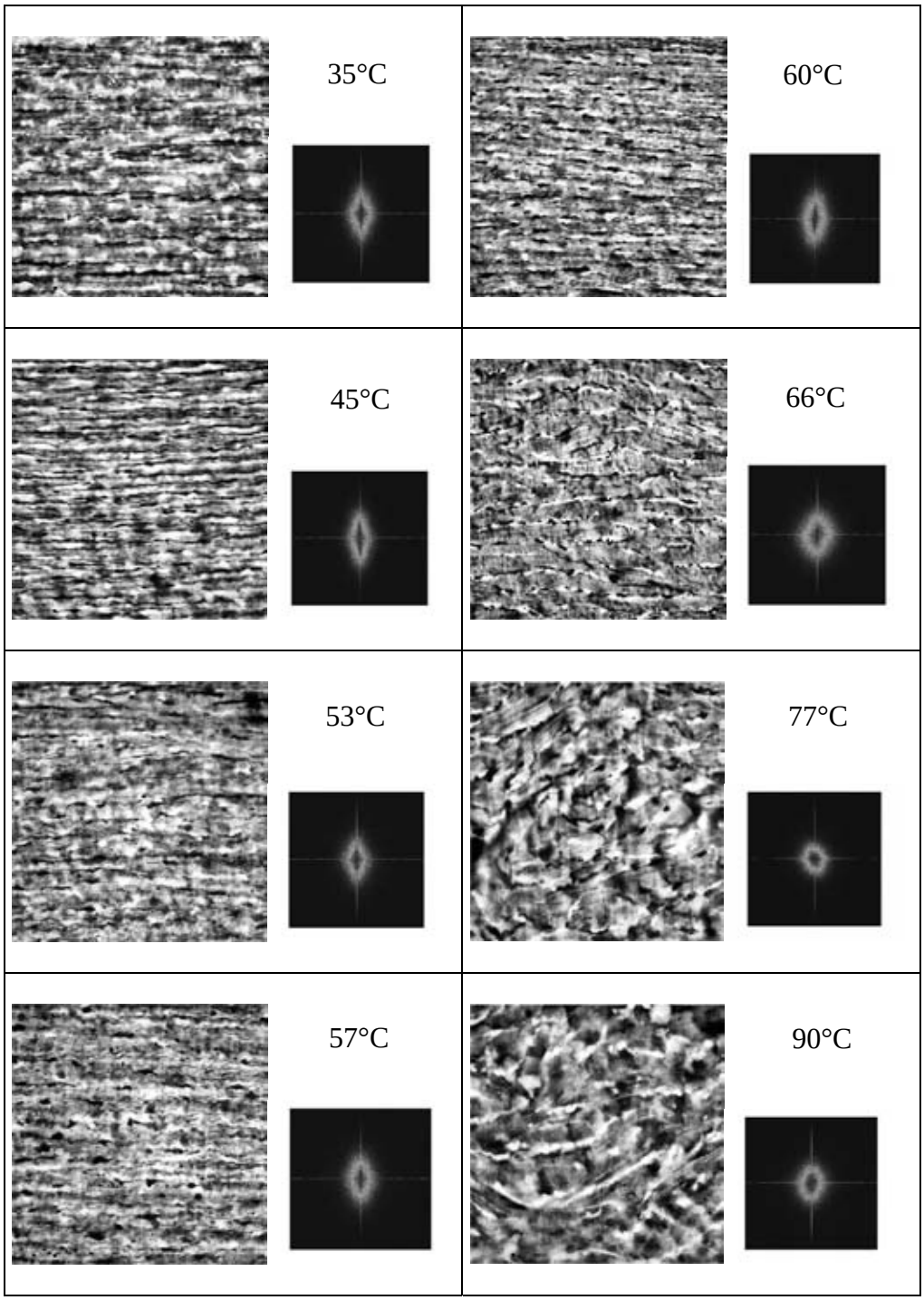


**Fig. 3.3** Fluorescence micro-images of cornea samples heated in a water-bath at different temperatures. The logarithm of the absolute value of the DFT is also shown to the right of each image. The images correspond to an area of 400×400 μm.

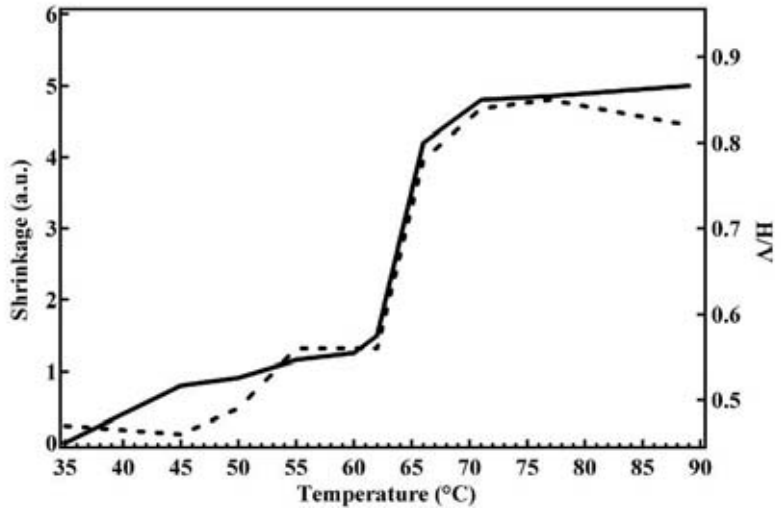


**Fig. 3.4** Plot of the corneal shrinkage (solid line) (expressed as $\Delta t^{-0.5}$ where $t$ is the measured corneal thickness) and DFT shape modification (dashed line) (expressed as the ratio between the width taken at the 70% level of the horizontal and vertical histograms) as calculated for different temperature values.

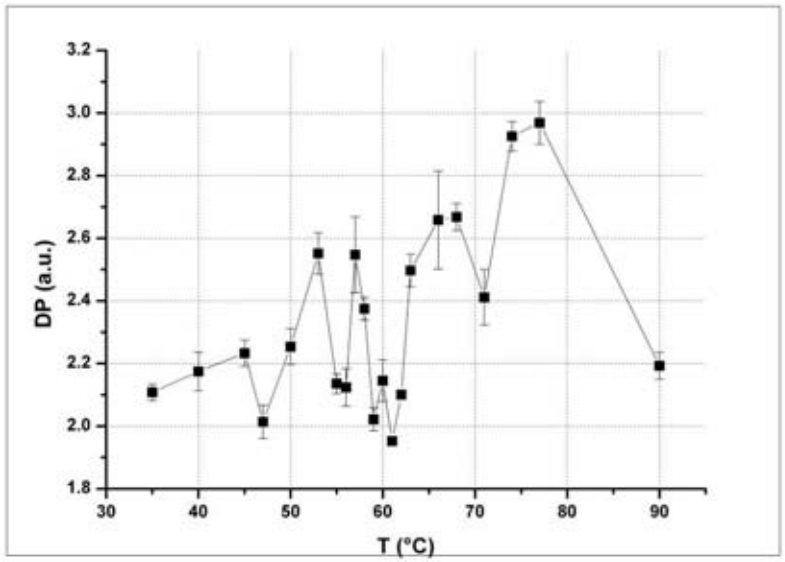


**Fig. 3.5** Plot of the Disorganization Parameter (DP) vs. temperature. Peaks are in correspondence with the principal phase transition temperatures of corneal tissue (see, i.e., [10,11])

### 3.2.4. Discussion

The image-processing method described turned out to be extremely precise in detecting thermally-induced morphological modifications of the corneal stroma. The DFT distribution gave a geometrical description of the acquired images as a function of the thermal treatment. The change in Fourier spectral appearance from elliptical to circular observed at around 62 °C is probably attributed to the occurrence of corneal shrinkage. In fact, the H/V plot

resembles well the shrinkage trend with an onset shrinkage temperature of 62 °C and a saturation value from 71 °C, and is in full agreement with previously reported values on porcine corneal specimens [12]. Corneal shrinkage takes place in the direction parallel to the axis of the collagen fibrils (i.e. parallel to the corneal surface) and is accompanied by a thickening in the direction perpendicular to this axis [13]. This contraction is closely associated with the uncoiling of the collagen triple helix leading to the early step of protein denaturation. For temperature conditions beyond 70 °C the contraction is overcome by relaxation processes leading to the ultimate step of collagen denaturation also called hyalinization or gelatinization [14]. This phenomenon is ascribed to the hydrolysis of the covalent cross-links connecting neighboring collagen molecules. The two steps of fibrillar collagen denaturation were finely highlighted in this study by two sequential phase-transitions peaked at around 66 °C and at 75 °C as shown by the DP plot. With regard to the other transition points detected by the image-processing analysis (see **Fig. 3.5**), the involvement of fibrillar collagen can be excluded, as inferred from previous studies on thermal-bathed connective tissues [15,16] and from our microscopy results on laser welded corneal tissue (see §2). In addition, DSC studies on rat skin collagen have pointed out that ground substance macromolecules may be possibly involved in the calorimetric endotherms observed for temperature values in the 50÷60 °C range [17,18]. It can be inferred that the phase transitions detected at 53 °C and 57 °C are related to some structural modification of extracellular components other than fibrillar collagen. Finally, collagen in the non-reticulated state (soluble) is more susceptible to temperature increases being in nonstabilized form, and has been proved to unwind at a temperature of about 40-45 °C [19,20]. Thus we may tentatively connect the first entropy peak detected at 45 °C to the denaturation of collagen in the monomeric form which may be present as neosynthesized molecules in the extracellular matrix, as previously suggested [17].

The proposed method was found to be highly effective for the characterization of thermal transitions of the cornea. By the use of DP in conjunction to DFT it was possible to label each phase transition. For example the 53 °C and 66 °C images have similar DP values (see **Fig. 3.5**), but the DFT spatial distribution is clearly different (see **Fig. 3.4**), permitting thus to distinguish between the two temperature points.

The method described here could be proposed as a control system, and mainly in those surgical procedures in which ICG staining of the tissue is also part of the treatment protocol, as in diode laser welding technique (see §1 and §2 of this thesis). Its extension to *in vivo* real-time applications could be carried out by means of an association with confocal microscopy. It could be ultimately proposed as the basis for a diagnostic methodology for *in*

*vivo* characterization of corneal structures used during surgical procedures based on heating treatments.

### 3.2.5 Conclusion

A procedure for characterizing phase transitions in corneal tissue with the use of a low cost apparatus and the simple implementation of an image-processing algorithm has been described. The system has been found to be extremely precise in detecting thermally-induced morphological modifications in the corneal stroma. It could, therefore, be used as the basis for a control methodology during surgical procedures based on heating treatments in connective tissues.

## References

1. M. L. J. Landsman, G. Kwant, et al.: J. Appl. Physiol. 40, 575 (1976)
2. L. -P. Kamolza, H. Andel , et al.: Burns 29, 785 (2003)
3. L. A. Yannuzzi, M. D. Ober, et al.: Am. J. Ophthalmol. 137, 511 (2004)
4. G.P. Holley, A.Alam, et al.: J. Cataract Refract. Surg. 28, 1027 (2002)
5. T. John: J. Cataract Refract. Surg. 29, 437 (2003)
6. L. Menabuoni, R. Pini, et al.: J. Cataract Refract. Surg. 33, 1608 (2007)
7. K.M. McNally: Laser tissue welding. In: Biomedical Photonics Handbook, ed by T. Vo-Dinh T (CRC Press, 2003) pp. 39/1-39/45
8. A. J. Welch and M. Van Germert: Optical-thermal response of laser-irradiated tissue (Plenum Press, 1995)
9. A. Jain: Fundamentals of digital image processing (Prentice-Hall, 1989)
10. J. Kampmeier, B. Radt, et al.: Cornea 19, 355 (2000)
11. H. Y. Tan, S. W. Teng, et al.: J. Biomed. Opt. 10, 054019 (2005)
12. E. Spoerl, G. Wollensak et al.: Ophtalmologica 218, 136 (2004)
13. J. C. Allain, M. Le Lous, et al.: Conn. Tissue Res. 7, 127 (1980)
14. M. N. Asiyo-Vogel, R. Brinkmann, et al.: J. Cataract Refract. Surg. 23, 515 (1997)
15. P. Kronick P, B. Maleeff B, and R. Carroll: Connect. Tissue Res. 18, 123 (1988)
16. S. Thomsen, H. Vijverberg, et al.: Proc. SPIE 1882, 230 (1993) 14
17. F. Flandin, C. Buffevant, and D. Herbage: Biochim. Biophys. Acta 791, 205 (1984)
18. M. Le Lous, F. Flandin, et al.: Biochim. Biophys. Acta 717, 295 (1982)
19. E. Tiktopulo and V. Kajava: Biochemistry 37, 8147 (1998)
20. P. E. Mc Clain, E. R. Wiley: J. Biol. Chem. 247, 692 (1972)

## 3.3 - SECOND-HARMONIC GENERATION (SHG) IMAGING

*This section is aimed at proposing an analytical method based on second-harmonic generation (SHG) imaging to track the loss of organization in the corneal collagen lattice induced by photothermal effect. Porcine cornea samples were treated with low-power laser irradiation in order to get localized areas of tissue disorganization. The disorder induced within the irradiated area of corneal stroma was quantified by means of Discrete Fourier Transform, auto-correlation and entropy analyses of the SHG images. Polarization modulated SHG measurements allowed to probe the changes in the structural anisotropy of sub-micron hierarchical levels of the stromal collagen. The obtained results emphasize the great potential of the SHG imaging to detect subtle modifications in the collagen assembly of cornea. Moreover, on account of the emerging potential of SHG imaging to become an in vivo diagnostic tool, the proposed analytical methods may find future application in the clinical setting.*
*The image processing algorithms were developed in collaboration with Dr. Fulvio Ratto and Francesca Rossi of IFAC-CNR of Florence.*

### 3.3.1 Introduction

Second harmonic generation (SHG) imaging is an emerging microscopy technique based on the nonlinear optical effect called SHG, also commonly called frequency doubling. This phenomenon require intense laser light passing through a highly polarizable material with a noncentrosymmetric molecular organization. The second-harmonic light emerging from the material is at precisely half the wavelength of the light entering the material. Thus the SHG process within the nonlinear optical material changes two near-infrared incident photons into one emerging visible photon at exactly twice the energy (and half the wavelength). Differently from other linear or nonlinear fluorescence microscopies (as one- or two-photon excited microscopy) in which some of the incoming energy is lost during relaxation of the excited state, SHG does not involve an excited state, is energy conserving and preserves the coherence of the laser light.

SHG imaging is particularly well suited to analyze connective tissues due to the significant second order nonlinear susceptibility of collagen [1,2]. This confers high contrast and specificity to the SHG images. Moreover the intrinsically noninvasive nature of this technique further enhances its potential to become a clinical tool to perform *ex vivo* biopsies or *in vivo* imaging. SHG signals have been used to discriminate cancerous tissue [3,4] and

genetic disorders [5], which are related to altered content and assembly of the collagen matrix resulting in a modulation of the SHG intensity. In addition, SHG microscopy holds great potential in differentiating normal and abnormal structures by using a polarization-modulation approach, which exploits the coherent nature of the second harmonic signal [6-9]. Overall SHG imaging is presently considered a powerful technique to investigate tissue structure and organization, and may become a noninvasive complement to traditional structural methods such as electron microscopy, X-ray diffraction and histological analysis.

The corneal stroma displays a very regular assembly of collagen fibrils (~30 nm in size) which are arranged parallel to each other into lamellar domains (i.e. 0.5-2.5 μm thick planar structures running parallel to the corneal surface) [10]. The highly ordered nature of this tissue makes it a convenient model to study disorganization events of the normal connective matrix. In this study, SHG imaging is used to quantify the photothermally-induced modifications in the fibrillar collagen assembly of laser-treated porcine corneas. The morphological and thermodynamic properties of this model have been thoroughly characterized in the context of early experiences of laser welding [11,12]. When the corneal stroma undergoes low-power continuous wave diode-laser treatment, a controlled thermal effect can be induced within the irradiated volume. The result is a mild perturbation of the regular fibrillar arrangement, while uncontrolled denaturation of collagen is avoided. Moreover, the extent of lattice disorder decreases smoothly and progressively with the distance from the center of the irradiated area. Such a model enables the study and comparison of different disorganization patterns on the same tissue sample.

In order to correlate the modulation of the SHG signal with the disorganization of the corneal collagen, an image analysis approach to quantify the different structural patterns of lamellar assembly generated by the laser irradiation was firstly adopted. Then maps of the local orientation of the fibrillar lattice and investigated the typical distance over which the regular sub-lamellar arrangement is preserved were extracted. Finally, a comparison between the second-harmonic polarization profiles from non-irradiated and irradiated areas was made, in order to highlight differences in the interfibrillar arrangement at the smallest resolvable length scale of our microscope. A parallel transmission electron microscopy (TEM) analysis was performed to further support the SHG data.

### 3.3.2 Materials and methods

#### 3.3.2.1 Sample treatment

Ten porcine eyes were enucleated and kept in a humid environment until the time of experiments, typically 12 h after their extraction. The cornea was explanted and sliced in 1-

mm-thick cross-sections with a razor blade. In order to induce a controlled temperature rise in the samples, each cornea was treated under usual conditions for the low-power diode-laser welding procedure [12]. In doing this, one side of the slice was stained with a water solution (10 % w/w) of a chromophore (Indocyanine Green, ICG). The stain was then washed out after 2 min, in order to remove the excess of chromophore not absorbed by the tissue. ICG is an effective optical absorber of laser radiation emitted at 810 nm, and so it can mediate a localized and well-controlled photothermal effect within the tissue [12]. The laser device used was an AlGaAs diode (Mod. Weld 800, El.En., Italy), equipped with an optical fiber of 300 μm-core diameter (NA 0.24). The fiber tip, which was kept at a constant distance of 1 mm from the surface of the slide, delivered to the sample a power of 40 mW (8.3 W/cm$^2$) for an overall time irradiation of 2 s. These parameters allowed to confine the photothermal effect within a ~400 μm-radius spot (see **Fig. 3.6**), inducing a gradient of disorganization in the corneal collagen from the centre to the periphery and beyond the irradiated area. After the treatment, the samples were stored in formalin until the SHG images were acquired.

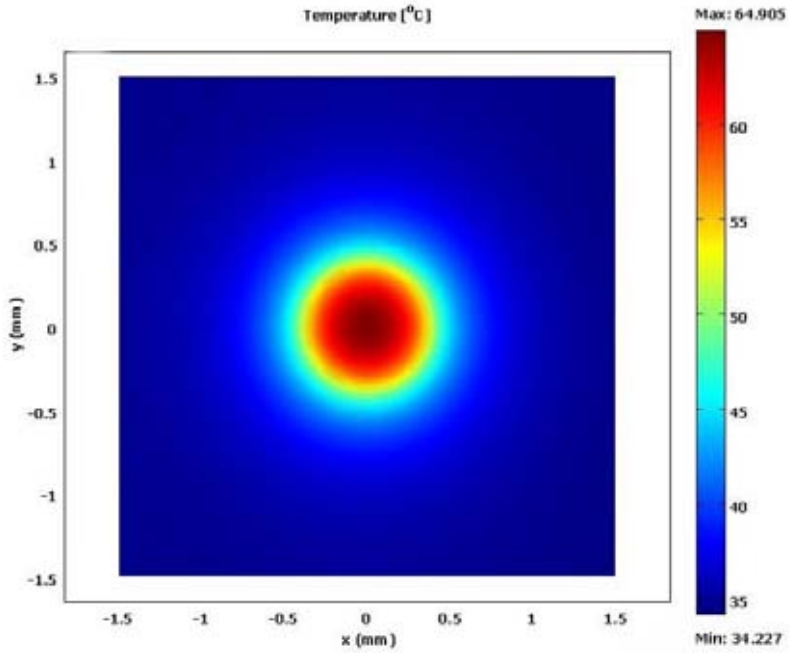


**Fig. 3.6.** Temperature development within a ~400 μm-radius spot area of a corneal slice subjected to diode laser irradiation. The data are the result of a 3D model (obtained with the software Comsol Multiphysics 3.4 (Comsol AB, Sweden)), based on the solution of the bio-heat equations, which describes the photothermal effects induced by the diode laser irradiation (40 mW power output, 2 s irradiation time) inside the tissue [11].

Laser-treated cornea slices were then processed for TEM measurements. In brief, they were fixed in glutaraldehyde and cut into 1 mm$^2$ samples including the laser-treated portion.

The samples were postfixed in osmium tetroxide and, after sequential dehydration, were infiltrated in Epon resin. Ultra-thin sections were cut and stained with uranyl acetate and lead citrate, and examined with an electron microscope (Philips CM-12, Philips Industries, Eindhoven, The Nederlands). Micrographs of representative fields of control and irradiated regions were taken from each specimen.

#### 3.3.2.2 SHG microscopy system

The experimental setup consisted of a modified inverted microscope (Nikon TE300, Nikon Instruments, Tokyo, Japan). Detailed descriptions of the SHG microscope have been given previously [13]. Briefly, the excitation was accomplished by a mode-locked Ti:Sapphire laser emitting 120-fs width pulses at a 90-MHz repetition rate, a wavelength of 880 nm and an average power at the sample in the range 1÷10 mW. The beam was focused onto the sample by a 50× 0.95 NA oil immersion objective (Nikon Plan-Apo, 0.35 mm WD, Nikon Instruments, Japan), and collected using a 60× 1.00 NA long working distance water immersion objective (Nikon Plan-Fluor, 2 mm WD, Nikon Instruments, Japan). A quarter-wave plate and a linear polarizer are placed immediately before the back focal plane of the focusing objective. The broad band (690-1200 nm) quarter-wave plate is mounted on a micromanipulator to obtain a circularly polarized light (with ellipticity equal to 1 within an error of 4%). A variable linear polarization of the exciting beam is accomplished through a linear polarizer mounted on a motorized rotating stage in order to rotate the polarization angle of the incident electric field without movement of the biological specimen. The SHG signal was isolated from the fundamental and any fluorescence by a 440 ± 5 nm band-pass filter (Z440BP, Chroma Technology Corporation, Rockingham, VT, US). For all imaging not involving the polarization analysis, the laser excitation was circularly polarized. The pixel dwell time was set to 5 μs/pixel. The scanning time was approximately 0.8 s for a 500×500 pixels image. Image areas of 60×60 $\mu m^2$ (0.12 μm/pixel), 500×500 pixels were considered, unless otherwise specified, for the analysis reported below.

#### 3.3.2.3 Image analysis of lamellar anisotropy

The analysis of the circularly polarized SHG corneal images was performed by means of two image processing techniques: the two-dimensional Discrete Fourier Transform (2D DFT) and the image entropy [14]. The processing algorithms were developed in the Matlab and IGOR Pro platforms (Matlab 7.0, the Mathworks, Natick, MA; IGOR Pro 4.07, WaveMetrics Inc. Lake Oswego, OR).

The frequency distribution in a Fourier-transformed image can be analyzed to retrieve the pattern of image line directions, so as to characterize the geometry of the image texture

[15]. Thus, the 2D DFT of each image was computed and the logarithm of the absolute value of the calculated DFT was displayed. Next, the DFT magnitude was thresholded to levels 0 or 1. The degree of DFT deformation was quantitatively calculated by fitting the result with an ellipse and by calculating the ratio between its short and long axes, i.e. its aspect ratio (AR).

The entropy is a statistical index widely used in the field of information theory to express the information content of a message. The entropy of the image intensity can be used to characterize its texture randomness [16]. Images were processed by applying the edge function based on Canny filter, to extract the spatial distribution of the collagen matrix. The calculation of the entropy E of an image with *n* grey levels was obtained by Eq. (1):

$$E = -\sum_{i=1}^{n} p(g_i)\log(p(g_i)) \qquad (1)$$

where $p(g_i)$ is the histogram value of the *i*-th grey level $g_i$. We defined a Disorganization Parameter (DP) as the inverse of *E* [14], and used it for subsequent analysis (growing DP values correspond to an increasingly disordered content of an image texture). Finally, AR and DP values, calculated for selected regions taken at different distances from the middle of the laser-irradiated area, were compared.

#### 3.3.2.4 Polarization analysis of sub-lamellar anisotropy

To assess the extent of the modification of the sub-lamellar assembly of the collagen matrix upon laser treatment, we investigated the dependence of the SHG signal on the polarization angle of the excitation light. We acquired series of images at different polarization angles (with steps of 10°) for selected control and irradiated areas of the laser-treated tissue. A twofold approach for the analysis of the polarization data was followed.

**Analysis of the sub-lamellar arrangement**

The polarization profile of the SHG intensity acquired from individual pixels exhibits a typical pattern of minima and maxima (see e.g. the experimental data (♦) in **Fig. 3.7**). As a rule of thumb, the minima are obtained when the polarization of the excitation light lies orthogonal to the principal axis of the collagen fibrils [8]. The identification of these minima allows for the construction of laterally resolved maps of the angles $\alpha$ which define the local mean orientation of the collagen fibrils within each pixel. The lateral resolution of these maps is about the size of the focal volume (i.e. about 400 nm as estimated by the Rayleigh criterion [17], with a 0.95 NA objective and $\lambda$ = 880 nm). These maps allowed us to

investigate the lateral correlation between the mutual orientations of the collagen fibrils through an immediate auto-correlation analysis. The auto-correlation matrices:

$$C(d_x, d_y) \equiv \frac{\sum_{i,j} \alpha(i + d_x, j + d_y)\alpha(i, j)}{\sum_{i,j} \alpha(i, j)^2}, \quad (2)$$

where the discrete variables $d_x$ and $d_y$ are the length along the horizontal and vertical directions, were computed from the data at different distances from the irradiated area, and then fitted to an isotropic exponential decay:

$$C(d_x, d_y) \equiv 10^{-\frac{\sqrt{d_x^2 + d_y^2}}{L}}, \quad (3)$$

in order to obtain a quantitative estimate of a correlation length $L$. The latter is taken to represent the typical distance over which the regular sub-lamellar arrangement is preserved.

**Analysis of the interfibrillar alignment at the sub-micron scale**

To investigate the laser-induced changes in the interfibrillar alignment, we analyzed polarization profiles from individual points (0.5 μm size) from treated and untreated areas of the corneal stroma. The appearance of the average profiles (average over 1000 randomly selected profiles per kind of area) provides qualitative insight of the modifications involved in the photothermal process.

Then we treat the polarization profiles in analogy to a time domain signal, and pursue a quantitative estimate of the main differences between the data from treated and untreated areas over a frequency domain, i.e. by an FFT analysis. In practice, a typical polarization profile can be decomposed into the sum of three main contributions, which are: 1) a zero frequency level, 2) a modulation signal found at low frequencies, 3) a supposedly white noise, which dominates at high frequencies (see the example in **Fig. 3.7**). In the analysis below we set a threshold for the upper frequency of the modulation signal at 1/60°, i.e. any maxima and minima narrower than three data points is treated as noise fluctuations.

The component at zero frequency simply represents the polarization-averaged SHG intensity. The components at low frequencies account for the main modulation of the signal as due to the local orientation of the fibrillar lattice. Conversely the components at high

frequencies are interpreted as pure noise fluctuations. With these assumptions, we computed the FFT of the SHG intensities and calculated an effective Modulation Parameter (*MP*) as the average amplitude of the FFT modulus at low frequencies $\langle I \rangle_{LF}$ minus the noise level $\langle I \rangle_{HF}$ (extrapolated from the average amplitude of the FFT modulus at high frequencies) and normalized by the intensity at zero frequency $I_0$:

$$MP = \frac{\langle I \rangle_{LF} - \langle I \rangle_{HF}}{I_0}. \quad (4)$$

The values of this parameter may give an indication of the extent of the alignment of the fibrils within the single point. We calculated the *MP* from individual polarization profiles and compared their average values from treated and untreated areas (average over 1000 profiles per kind of area).

### 3.3.3 Results and discussion

The circularly polarized SHG images of the corneal stroma (**Fig. 3.8**) revealed ~ 0.5 μm thick fiber-like structures, which actually consisted of many collagen fibrils, organized in lamellar domains, and which were previously referred to as fibrillar bundles [18]. The size of these structures is comparable with the minimum resolvable distance for our microscope (~ 400 nm, i.e. the size of the focal volume given by the Rayleigh criterion, see §3.3.2).

**Fig. 3.9** displays an example of a stack of four images taken at different distances from the center of a ~ 400 μm-radius laser-irradiated spot area. These four regions of interest (ROIs, 60×60 $\mu m^2$ each) well represent the progressive collagen disorganization. At the exterior of the spot (ROI a) a parallel arrangement of waved lamellar planes is clearly visible. Moving towards the center of the laser-treated area (ROIs from b to d), the lamellar arrangement is progressively lost and a dense packing of increasingly disordered collagen bundles appears. Correspondingly, the 2D DFT diagrams transform from elliptical to circular shapes, which indicates a transition towards random patterns.

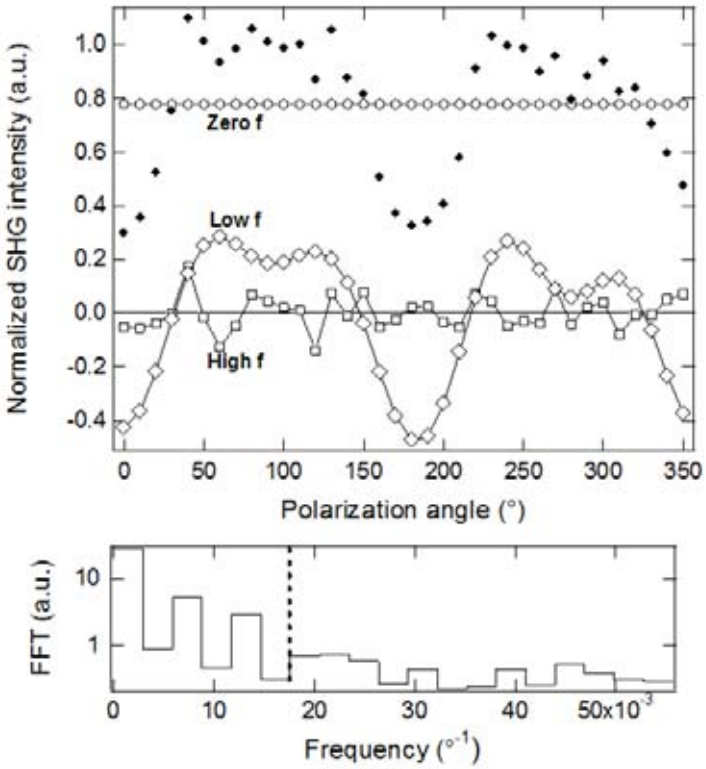


**Fig. 3.7** FFT of a polarization-modulated SHG profile. Upper: frequency (f) decomposition of the experimental data (♦) into zero (○), low (◊) and high (□) frequency contributions. Lower: frequency distribution (log scale).

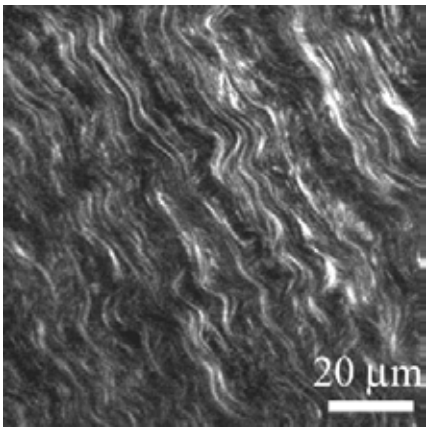


**Fig. 3.8** SHG image of an intact porcine corneal stroma.

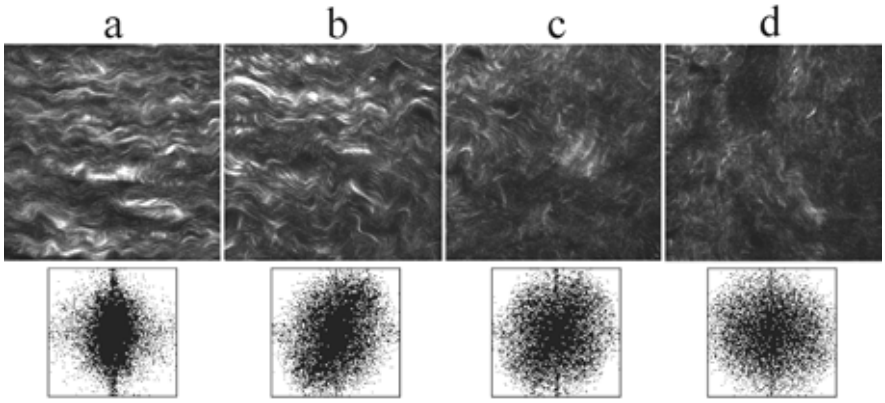


**Fig. 3.9** Stack of SHG images (60×60 μm$^2$ ROIs) taken from the periphery to the center of a laser-irradiated spot area. The radial distance of the ROIs from the center of the irradiation spot area are 600 μm (a); 400 μm (b); 200 μm (c); 0 μm (d). The DFT diagram of each ROI is also shown in the lower panels.

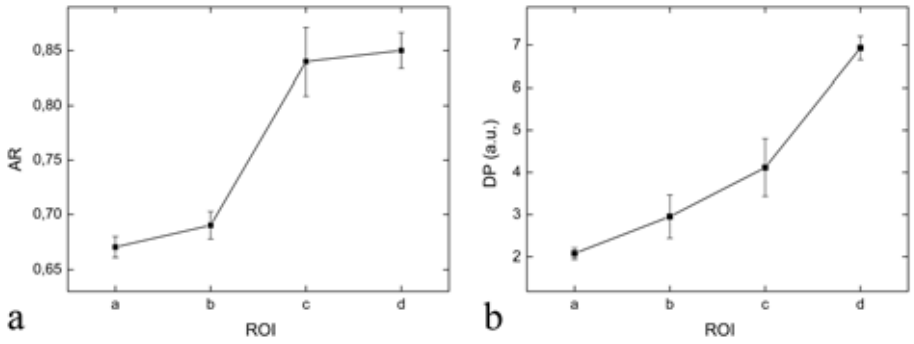


**Fig. 3.10** Plot of the mean value (± SD) of: (a) the Aspect Ratio (AR) of the ellipse approximating the DFT magnitude and (b) the Disorganization Parameter (DP) of 4 different ROIs as represented in Fig. 3.9. Each data point is the average over values from different regions of the same sample.

The increase of the corresponding AR is evident when moving from the periphery to the center of the spot as shown in **Fig. 3.10a**. The wavy behavior of the collagen lamellae is interpreted as the reason why the AR values never go below 0.6, even in control untreated regions. The DP also increases when moving toward regions of higher tissue randomization (**Fig. 3.10b**). It is noteworthy to underline the higher capacity of the AR to reveal transitions from normal or rather-structured (ROIs a,b) to more disorganized patterns (ROIs c,d). In contrast the DP parameter is more sensitive to discriminate between patterns of higher disorder (compare ROIs c and d).

In order to gain further insight into the induced stromal arrangement, an analysis of the sub-lamellar assembly was carried out. Although the resolution of our SHG microscope is not enough to detect individual corneal fibrils (the fibrillar size is ~30 nm), it may still be effective to investigate the mutual organization of fibrils within each lamella (of the order of

the resolution of our set-up). Indeed the acquisition and analysis of polarization-modulated SHG signals has been shown to provide a very fine description of the local matrix anisotropy [7,19-22].

As a first step, by the analysis of the minima in the polarization profiles, we extracted the local orientation of the fibrillar lattice from representative areas (8×8 $\mu m^2$) (as depicted in **Fig. 3.11a,d,g**), taken at three different distances from the periphery toward the center of a laser-irradiated area. We built two dimensional maps of the values of $\alpha$, which denotes the local mean orientation of the collagen fibrils within each pixel (see **Fig. 3.11b,e,h**). Then we calculated the lateral correlation among these orientations, which represents the typical distance over which the regular sub-lamellar arrangement is preserved. Correlation lengths of around 2.9, 1.5 and 0.4 microns were found for the three areas examined (**Fig. 3.11c,f,i**). The calculated correlation length for the control area is compatible with the mean size of the individual stromal lamellae (typically from 0.5 to 2.5 μm thick, see e.g. [10]). On the other hand, the value associated to the center of the spot area is very close to the resolution of our microscope (see § 3.3.2), as expected in a highly disordered matrix. These results are in agreement with the aforementioned observations on a progressive loss of the lamellar domains when moving from the periphery toward the center of a laser-irradiated spot area.

The final step of our analysis was the investigation of the loss of anisotropy at sub-micron structural levels of the stromal architecture (i.e. about the minimum resolvable distance of our microscope). To this aim, we extracted and averaged the polarization profiles from single points (0.5 μm size, n = 1000) taken randomly from untreated (**Fig. 3.12a**) and irradiated (**Fig. 3.12d**) areas, as reported in **Fig. 3.12b** and **Fig. 3.12e** respectively. The random procedure is intended to evenly represent all the possible mean orientations of the collagen fibrils in the two samples (which may in general exhibit an out-of-plane component). In addition we performed a TEM analysis to validate our polarization-modulated SHG results on the sub-micron structure of our samples (see **Fig. 3.12c,f**). The SHG profile obtained from the control area exhibits a significant modulation which is believed to originate from a highly ordered interfibrillar arrangement, in agreement with the TEM analysis. Indeed the corresponding TEM micrographs display the alternation of regular lamellar domains, composed of well-aligned collagen fibrils. By contrast, the SHG-profile relative to the treated area is partially degraded. This result may be consistent with either of two different dynamics, i.e. the loss of regular alignment of the collagen fibrils already over the length scale of the available resolution, or the loss of integrity of the collagen fibrils (i.e. a degradation of the SHG-generators due to the thermal denaturation of the collagen molecules). The TEM analysis revealed the coexistence of sub-lamellar groups of differently oriented and interwoven fibrils, which however preserve their individual

integrity and never display the fingerprints of denaturation (fibril swelling which increases the fibrillar diameter, and loss of edge sharpness). Thus, we deduce that the fibrillar bundles observed in the SHG images of laser-irradiated areas may probably represent packets of native collagen fibrils, which still keep an average preferential orientation against an increasing degree of local disorder. This mild perturbation of the regular fibrillar arrangement is fully consistent with the expected temperature value at the center of the laser-irradiated spot area, i.e. ~65 °C (see **Fig. 3.6**), which has been previously shown to represent the threshold value below which the fibrillar collagen keeps undenatured [14].

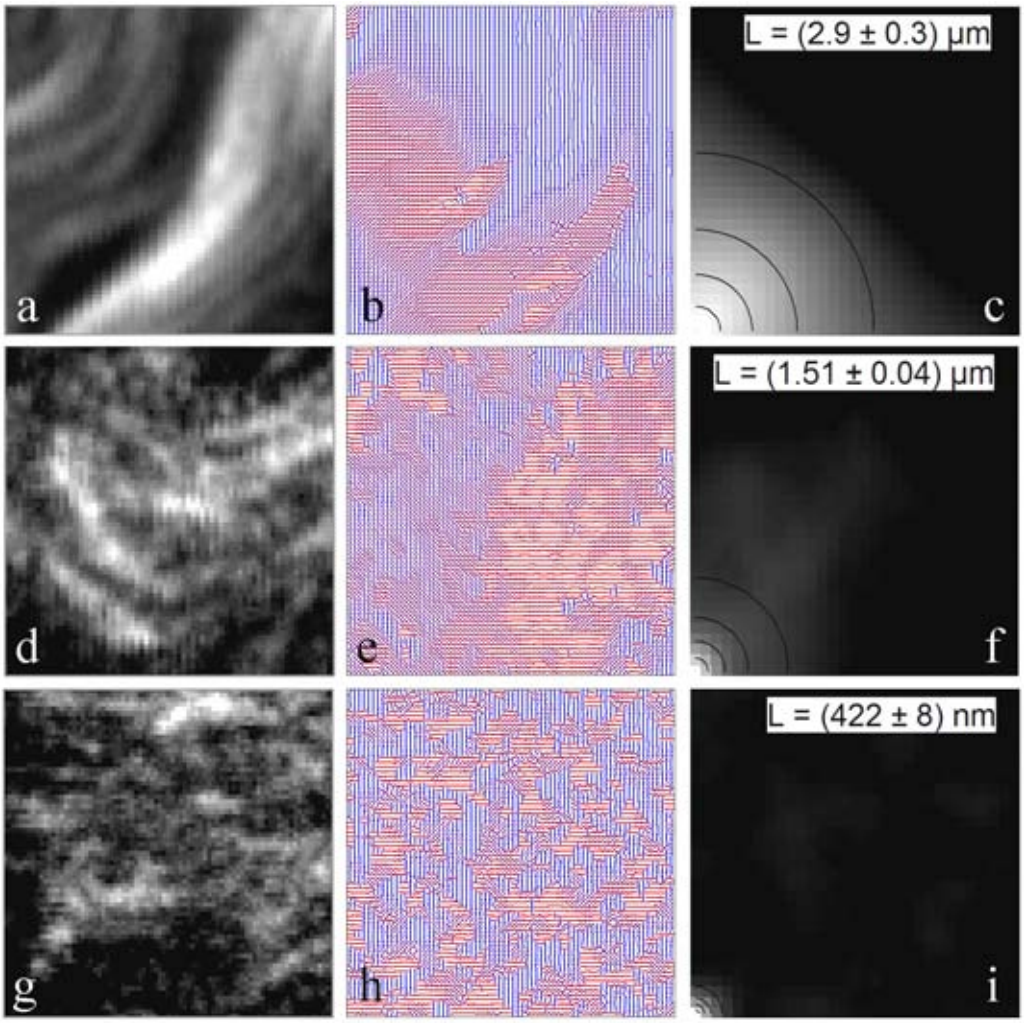


**Fig. 3.11** Analysis of the sub-lamellar arrangement. SHG images (8×8 $\mu m^2$) (a,d,g), maps of the orientations of the collagen fibrils (b,e,h), and auto-correlation matrices (c,f,i) taken at a distance of 600 µm (a,b,c); 300 µm (d,e,f); 0 µm (g,h,i) from the center of the laser-irradiated spot area. *L* is taken to represent the typical distance over which the regular sub-lamellar arrangement is preserved.

In order to quantify these observations, we carried out an FFT analysis of the polarization profiles, which are regarded as the superposition of three contributions, as explained before (see § 3.3.2). In particular, we considered the distribution of the values of

the noise-subtracted low frequency component normalized by the zero frequency component (*MP*). This parameter is readily accessible, proves sensitive to the local loss of anisotropy, and allows for the detection of even minor deviations from the normal reference profile. The limit value of zero represents the isotropic situation, and physically corresponds to the complete disorganization of the fibrillar distribution. Progressively higher values correspond to increasing degrees of order, i.e. of better alignment of the fibrils. Typical *MP* values extracted from the control areas are *MP* = (6.85 ± 0.10) %, which is taken as the highly ordered limit in the corneal stroma. In contrast, average values of *MP* = (2.39 ± 0.09) % (intermediate loss of anisotropy) are found in the laser-treated areas.

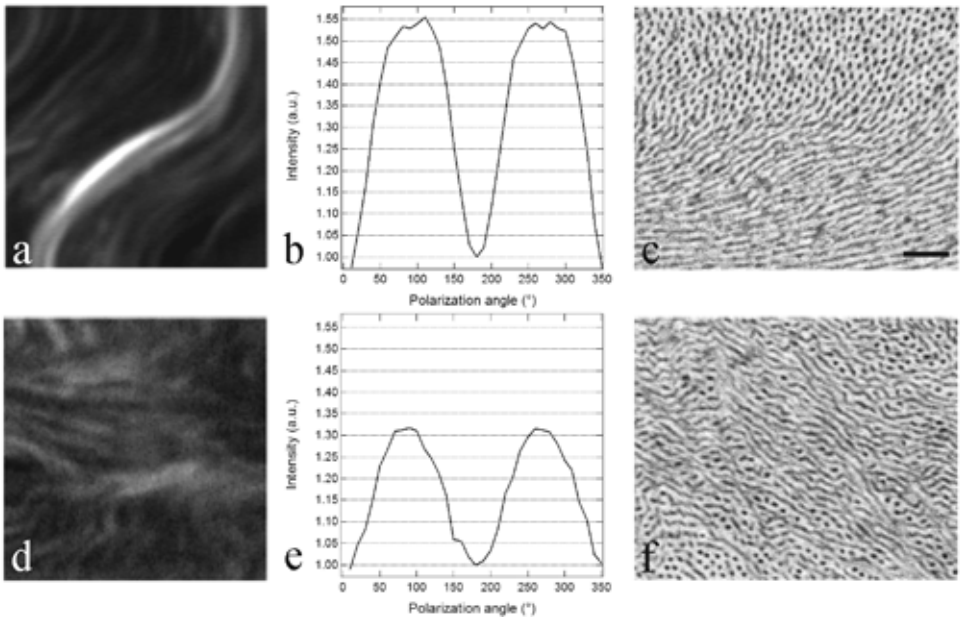


**Fig. 3.12** Polarized-SHG and TEM analyses of the interfibrillar alignment. Left: SHG images (12×12 μm$^2$) of a control (a) and a laser-irradiated (d) region taken at a radial distance of 600 and 0 μm from the center of a laser-irradiated spot area, respectively. Middle: (b,e) average polarization profiles of single points (0.5 μm size, n = 1000) taken randomly from control (a) and laser-irradiated (d) regions, respectively. Right: TEM micrographs (bar = 300 nm) showing the nanometric assembly of collagen fibrils in a control (c) and laser-irradiated (f) region.

### 3.3.4 Conclusions

We have introduced an empirical approach based on three complementary analytical methods to process the SHG signals and characterize the corneal stroma disorganization induced by photothermal effects following laser irradiation. This disorganization was probed at different hierarchical levels of the collagen assembly. The lamellar disorder was effectively quantified by the variation of the 2D DFT magnitude and of the image entropy of circularly-polarized SHG images. We then took advantage of the polarization dependence of the SHG intensities to extract maps of the local orientation of the collagen fibrils. These maps were used to retrieve the typical distance over which the regular sub-lamellar

arrangement is preserved when passing from the laser-untreated to the laser-treated areas. We finally probed the changes in the fibrillar packing at the sub-micron scale by a simple analysis of the modulation of the polarization profiles.

Similar analytical procedures may be applied to study several genetic, pathologic, accidental or surgical-induced disorder states of biological tissues. Moreover, on account of the emerging potential of SHG imaging to become an *in vivo* diagnostic tool, the proposed analytical methods may find future application in the clinical setting.

## References

1. W.R. Zipfel, R.M. Williams, et al.: Proc. Natl. Acad. Sci. USA 100, 7075 (2003)
2. P.J. Campagnola and L.M. Loew: Nat. Biotechnol. 21, 1356 (2003)
3. E. Brown, T. McKee, et al.: Nat. Med. 9, 796 (2003)
4. R. Cicchi, D. Massi, et al.: Opt. Express 15, 10135 (2007)
5. O. Nadiarnykh, S. Plotnikov, et al.: J. Biomed. Opt. 12, 051805 (2007)
6. S. Roth and I. Freund: J. Chem. Phys. 70, 1637 (1979)
7. P. Stoller, K.M. Reiser, et al.: Biophys. J. 82, 3330 (2002)
8. K.M. Reiser, C. Bratton, et al.: J. Biomed. Opt. 12, 064019 (2007)
9. R. Lacomb, O. Nadiarnykh, and P.J. Campagnola: Biophys. J. 94, 4504 (2008)
10. Y. Komai and T. Ushiki: Inv. Opht. Vis. Sci. 32, 2244 (1991)
11. F. Rossi, R. Pini, and L. Menabuoni: J. Biomed. Opt. 12, 014031 (2007)
12. F. Rossi, R. Pini, et al.: J. Biomed. Opt. 10, 024004 (2005)
13. R. Cicchi, S. Sestini, et al.: J. Biophotonics 1, 62 (2008)
14. F. Rossi, P. Matteini, et al.: Opt. Express 15, 11178 (2007)
15. R. Holota and S. Němeček: In Applied Electronics ed by J. Pinker (University of West Bohemia, Pilsen, 2002)
16. J. Kuczyński and P. Mikołajczak: Opto-Electron. Rev. 11, 253 (2003)
17. R. Gauderon, P.B. Lukins, and C.J. Sheppard: Micron 32, 691 (2001)
18. M. Han, G. Giese, and J.F. Bille: Optics Express 13, 5791 (2005)
19. S.W. Chu, S.Y. Chen, et al.: Biophys. J. 86, 3914 (2004)
20. F. Tiaho, G. Recher, and D. Rouède: Opt. Express 15, 12286 (2007)
21. P. Stoller, B.M. Kim, et al.: J. Biomed. Opt. 7, 205 (2002)
22. C.K. Chou, W.L. Chen, et al.: J. Biomed. Opt. 13, 014005 (2008)

## 3.4 - PERSPECTIVES

The imaging systems we proposed have been tested on *ex vivo* corneal samples. Future investigations should be focused on assessing their feasibility when applied to biological tissue *in vivo*. As just mentioned in the introduction to this chapter (see §3.1), DSC, histology and electron microscopy techniques are the gold standard to finely characterize the (photo)thermally-induced modifications of biological tissues *ex vivo*, including cornea, although they are definitely unsuitable for monitoring heat-induced changes *in vivo*. In addition to these techniques, we can also identify two other techniques, which are used for noninvasive *in vivo* corneal imaging. They are reflection confocal microscopy and optical coherent tomography (OCT), which, however, fail to characterize (photo)thermally induced changes, due to different reasons. While reflection confocal microscopy can achieve cellular imaging in the cornea, it cannot detect the main component of the stroma, i.e. type I collagen, whose structural changes are mainly responsible of the effects induced to the tissue by the therapeutic (photo)thermal treatments. In addition, this technique uses a visible light source, which causes more scattering through the media. OCT is based on the detection of backscattering photons from the ocular structures. The actual resolution of the commercially available OCT systems is typically limited to 10-15 µm, which is insufficient to resolve the thin posterior layers of the cornea (being human cornea 500 microns thick).

The imaging techniques we proposed to detect the structural changes in *ex vivo* corneal tissue have the potential to overcome many of the abovementioned problems. Speaking of fluorescence imaging, this chapter proved the high fluorescence contrast generated by type I collagen stained with an exogenous fluorophore (ICG). This was accomplished by using a blue excitation wavelength (436 nm), which was selected due to the optical components at our disposal. However, the blue wavelength can be definitely replaced with a more suitable wavelength, as a near infrared (NIR) one, which induces less scattering and is less absorbed by the tissues, thus being potentially less dangerous for *in vivo* applications. Furthermore, the utilization of a NIR source is a better choice due to the absorption properties of ICG in this spectral region (see **Fig. 3.2**), which can actually enhance the fluorescence signal of the imaged specimens. However, fluorescence imaging presents also some drawbacks.

A main disadvantage of using fluorescence as an imaging tool to detect collagen *in vivo* is ascribed to the photobleaching of the fluorophores (in our case, ICG). Experimentally this is observed as the loss of fluorescence signal of a stained specimen following continuous illumination with a ultraviolet and also with visible light, used as excitation sources. The basis of this phenomenon is the photochemical transformation of the fluorescent molecule into another molecule that is not fluorescent, probably mediated by the presence of oxygen.

Another main disadvantage concerns the out-of-focus contributions. In fact, in a "one-photon" (as the one used in this thesis, also referred to as "conventional") fluorescence microscope, thick specimens will produce an image that represents the sum of sharp image details from the in-focus region, combined with blurred images from all the out-of-focus regions. This contribution reduces the contrast of the in-focus image. This can be problematic when imaging thick samples like the whole cornea. (We have analyzed stromal slices to overcome this problem). A recent alternative to conventional fluorescence microscopy is two-photons fluorescence microscopy, which utilizes a tightly focused excitation beam so that the region outside the focus has much less chance to be excited, eliminating the out-of-focus fluorescence. This technique also reduce photobleaching, because only the region at the focal point can be excited. Future measurements will be devoted to assess the feasibility of this imaging technique on (photo)thermally treated cornea samples.

Large sensing depth and high resolution make SHG another outstanding tool for noninvasive imaging of the corneal structure. Although this technology is more complex and costly, it may represent a viable alternative to histological and conventional fluorescence analysis, since samples can be imaged in their natural state without fixation and labeling (and consequent photobleaching) and sectioning. In addition, SHG occurs only in non-centro-symmetric media, such as collagen. Thus SHG is a very well suited choice for corneal imaging, because of the significant amount of type I collagen content of the stroma. Furthermore SHG signal is only obtained at exactly half the wavelength of the laser beam excitation, thus allowing an easy discrimination against background autofluorescence or other nonspecific contributes.

In our experimental set-up we have used a forward-detection geometry for acquire SHG signals of corneal samples. Nonetheless, the backward-detection (or epi-detection) geometry is undoubtedly the only feasible method for imaging entire organs *in vivo*. Backward-detected SHG can arise from either direct backward coherent emission of from multiple scattering of initially forward-directed photons. The first scenario is highly dependent upon fibril diameters and packing. Fibrils in tissues much smaller than the SHG wavelength produce a symmetrical forward and backward emission distribution. When the dipoles of adjacent molecules form aligned structures comparable to or larger than the SHG wavelength (in the axial dimension), the emission become highly forward detected. This latter is the case of corneal stroma, where exists, under normal conditions (i.e. in native cornea), a very regular arrangement of collagen fibrils. So, a low backward coherent signal in stromal specimens is expected. Nonetheless, this signal is detectable, as proved by some authors and by us during a very preliminary set of measurements (see the figure below).

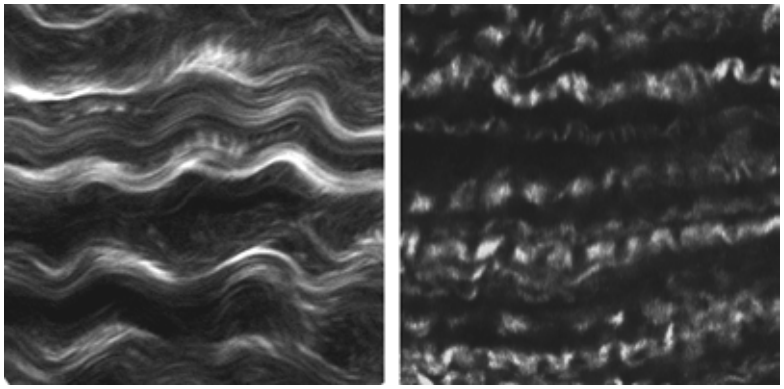

**Fig. 3.13** SHG images of corneal stroma in (left) forward and (right) backward directions.

Furthermore, during events of randomization (as those occurring upon a (photo)thermal process) the regular fibrils arrangement is lost (see §3.2.3 and §3.3.3) and the tissue becomes highly scattering. We thus expect to detect a consistent backward signal dominated by the back scattered component that arises from multiple scattering of the forward signal. The acquisition of an incoherent SHG signal can actually hamper the gaining of information on the directionality of collagen fibrils within the tissue, because, upon scattering, the polarization of the signal becomes randomized. Nevertheless, the analytical methods proposed to extract information on local collagen arrangement are applied also to unpolarized data (as those based on DFT and entropy algorithms, see §3.3.2) and will probably be successful. This scenario needs to be verified in the next future by measuring the backward SHG signal from (photo)thermally treated cornea specimens.

In conclusion, we feel confident that future implementations of fluorescence and of SHG technology could lead to carry out noninvasive *in vivo* imaging of the local anisotropy of corneal tissue, which could be extremely useful during surgical methodologies based on induced (photo)thermal effects.

# 4. OPTIMIZATION OF LASER WELDING (Part II)

## Investigation on the application of new nanoparticles as laser-activated chromophores

*As a further step toward the optimization of laser welding techniques, the efficiency of new nanochromophores as photothermal transducers was assessed. In particular, the attention was focused on colloidal gold nanorods. The physicochemical and morphological properties of colloidal solutions of these chromophores, along with their capability to generate laser-induced hyperthermia during applications of laser tissue welding, were studied.*

### 4.1 - BACKGROUND

*In this section a short presentation of the new nanochromophores that can be effective for biomedical applications is reported. In particular the attention is focused on gold nanoparticles.*

Laser welding of biological tissues has received substantial momentum from coupling with exogenous chromophores with enhanced absorbance in the near-infrared, applied topically at the edges of the wounds prior to irradiation. Suitable exogenous chromophores absorb efficiently and selectively the near-infrared light from a laser, which immediately translates

into well-localized hyperthermia and an overall decrease of the power thresholds required to achieve closure of wounds. (An exhaustive explanation of these concepts was reviewed in the first chapter of this thesis.) The ultimate exogenous chromophore should display high absorption coefficient in the near-infrared and enable high localization of power deposition, ideally down to the scale of individual biological structures. Further desirable features include good chemical and thermal stability and high photobleaching threshold.

Conventional chromophores of common use in laser-welding are organic molecules such as Indocyanine Green (ICG). These have given outstanding experimental and clinical achievements in a number of medical fields, and that in spite of relatively poor performances with respect to the aforementioned criteria [1,2]. The absorption efficiency and photostability of organic molecules are limited. Their optical properties depend strongly on biochemical environment and temperature, and generally deteriorate rapidly with time [3]. The range of chemical functionalities accessible is narrow, which is incompatible with flexible and selective targeting of distinct biological structures. Overcoming of these limitations would represent a real breakthrough in the practice of laser-welding, as well as in other biomedical applications.

Possible solutions are disclosed by the advent of nanotechnology, as a powerful platform to develop new functionalities, by manipulation of self-organization processes at the nanoscale. Here a new class of nanostructured chromophores that is attracting much attention in view of many applications is introduced.

### 4.1.1 Gold nanoparticles (nano-gold)

Whereas the optical response of organic molecules stems from electronic transitions between molecular states, light absorption and scattering in nano-gold originates from excitation of collective oscillations of mobile electrons, i.e. surface plasmon resonances [1]. This translates into molar extinction coefficients higher by 4 - 5 orders of magnitude with respect to those of organic chromophores, enhanced thermal stability and photobleaching threshold. As a traditional material for implants, gold is believed to ensure good biocompatibility [4], which is a critical prerequisite in front of clinical applications. The possibility of flexible conjugation of gold surfaces with biochemical functionalities opens a wealth of novel opportunities [5], such as selective targeting against desired and well-defined biological structures.

The utilization of nano-gold dates back to the ancient Romans, when employed for decorative purposes in the staining of glass artifacts (see e.g. the Lycurgus cup). Synthesis of stable aqueous colloidal preparations of nano-gold was first achieved by M. Faraday toward the 1850s by use of phosphorous to reduce a solution of gold chloride. Subsequent

developments led to a number of variants especially based on reduction of chloroauric acid in sodium citrate (Turkevich method) [6,7]. Conventional nano-gold is composed of spherical nanoparticles of variable and controllable radii [7]. The plasmon resonance of spherical nano-gold in aqueous environment is found within 500 - 600 nm, almost independent of geometrical volume [1].

Due to absorption in the visible, conventional nano-gold is not regarded as a candidate ideal chromophore for laser-welding of biological tissues. Localization of power deposition requires preferential use of near-infrared radiation. However, tuning of size and shape of these nanoparticles, allows for tuning of plasmon resonances [8]. By modification of existing procedures for spherical nano-gold, a number of non-spherical gold nanoparticles have been demonstrated, including dielectric core/metal-shell silica or gold-sulphide/gold nano-shells [9,10,11], complex hollow shells as gold nano-cages [12], or high aspect ratio gold nano-rods [13,14] (**Fig. 4.1**). In particular absorption within the near-infrared range of interest is becoming a mature achievement. Near-infrared-light irradiation of biological media dispersed with non-spherical nano-gold was proven to result in selective, controllable and significant heating [15,16].

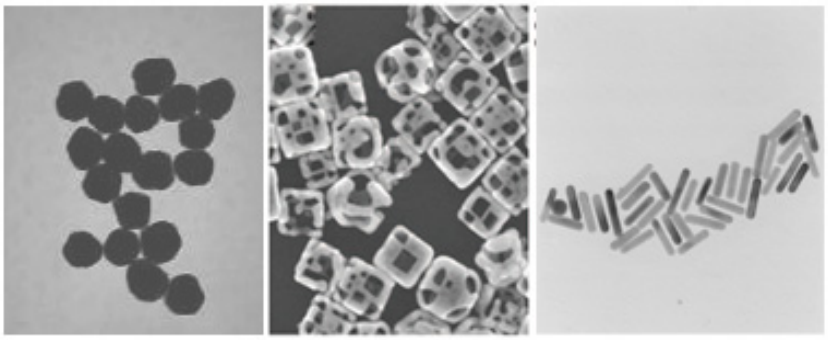

**Fig. 4.1.** Gold nano-speres, gold nano-cages, gold nano-rods imaged by electron microscopy. (from www.nanopartz.com, [20], our image, respectively).

Photo-activated non-spherical nano-gold holds the promise of manifold applications in the emerging field of nano-medicine. Proposals of extreme interest are e.g. in the treatment of tumors by selective ablation of individual malignant cells [16,17,18]. In the context of laser welding, the potential of silica/gold nano-shells in the sealing of tissues has recently been demonstrated in combination with an albumin solder [19]. Absorption of 820 nm diode laser radiation by a low concentration of nano-shells was shown to induce successfully the coagulation of albumin and the ensuing soldering of muscles *ex vivo* and of skin *in vivo* (rat model). Up to this day, the latter is the only study dealing with laser suturing of biological tissues.

## References


1. P.K. Jain, K.S. Lee, I.H. El-Sayed, et al.: J. Phys. Chem. B 110, 7238 (2006)
2. F. Wang, W.B. Tan, Y. Zhang, et al.: Nanotechnology 17, R1 (2006)
3. V. Saxena, M. Sadoqi and J. Shao: Int. J. Pharm. 308, 200 (2006)
4. R. Shukla, V. Bansal, M. Chaudhary, et al.: Langmuir 21, 10644 (2005)
5. M.C. Daniel and D. Astruc: Chem. Rev. 104, 293 (2004)
6. L.M. Liz-Marzan: Materialstoday Feb. 2004, 26 (2004)
7. J. Kimling, M. Maier, B. Okenve, et al.: J. Phys. Chem. B 110, 15700 (2006)
8. M. Hu, J. Chen, Z.Y. Li, et al.: Chem. Soc. Rev. 35, 1084 (2006)
9. S. Kalele, S.W. Gosavi, J. Urban, et al.: Curr. Sci. 91, 1038 (2006)
10. H.S. Zhou, I. Honma, H. Komiyama, et al.: Phys. Rev. B 50, 12052 (1994)
11. L.R. Hirsch, A.M. Gobin, A.R. Lowery, et al.: Ann. Biomed. Eng. 34, 15 (2006)
12. Y. Sun and Y. Xia: Science 298, 2176 (2002)
13. J. Perez-Juste, I. Pastoriza-Santos, L.M. Liz-Marzan, et al.: Coord. Chem. Rev. 249, 1870 (2005)
14. N.R. Jana, L. Gearheart and C.J. Murphy: J. Phys. Chem. B 105, 4065 (2001)
15. C.H. Chou, C.D. Chen and C.R.C. Wang: J. Phys. Chem. B 109, 11135 (2005)
16. L.R. Hirsch, R.J. Stafford, J.A. Bankson, et al.: Proc. Natl. Acad. Sci. 100, 13549 (2003)
17. J.Y. Chen, F. Saeki, B.J. Wiley, et al.: Nano Lett. 5, 473 (2005)
18. X. Huang, I.H. El-Sayed, W. Qian, et al.: J. Am. Chem. Soc. 128, 2115 (2006)
19. A. M. Gobin, d. P. O'Neal, D. M. Watkins, et al.: Lasers Surg. Med. 37, 123 (2005)
20. S. E. Skrabalak1, L. Au1, X. and Y. Xia: Nature Protocols 2, 2182 (2007)
21. A.V. Kabanov, S.V. Vinogradov, Y.G. Suzdaltseva, et al. Bioconjug. Chem. 6, 639 (1995)
22. R. Savic, L. Luo, A. Eisenberg, et al. Science 300, 615 (2003)
23. G.S. Kwon Crit. Rev. Ther. Drug Carr. Syst. 20, 357 (2003)
24. V.P. Torchilin, A.N. Lukyanov, Z.Gao, et al.Proc. Natl. Acad. Sci. U. S. A. 100,6039 (2003)
25. D. Trentin, J. Hubbell, et al. H. Hall J. Control. Release 102, 263 (2005)
26. V. S. Bugrin, M. Y. Kozlov, I. I. Baskin, et al. Polymer Science 49, 463 (2007)
27. G. Nemethy and H. A. Scheraga J. chem.. Phys. 36, 3382 (1998)

## 4.2 - LASER WELDING WITH GOLD NANORODS

*In the following, a study of the application of laser-activated gold nanorods in the direct welding of connective tissues is reported. In particular, tissue samples of the eye's lens capsule obtained from ex-vivo porcine eyes were used. The nanochromophores consisted of gold nanorods with aspect ratio ~ 4, which were applied at the interface of sandwich composed of a patch of capsular tissue from a donor eye and the upper surface of the capsule of a recipient eye. The administration of laser pulses of 40 ms duration and 100 – 140 J/cm$^2$ energy density per pulse allowed the achievement of local denaturation of the endogenous (type IV) collagen filaments, suggesting the achievement of temperatures above 50 °C.*

*The synthesis of the nanoparticles was developed in collaboration with Dr. Fulvio Ratto of IFAC-CNR and with the group of Prof. Kulkarni of the University of Pune (India). Basically, colloidal solutions of gold nanorods were obtained in a seed-mediated approach derived from the protocol developed by Nikoobakht (see [20]), which was further optimized and customized to obtain nanoparticles suitable for their use in diode laser welding experiments.*

### 4.2.1 Introduction to gold nanorods

The combination of near infrared (NIR) radiation, which penetrates deep into the body, with corresponding exogenous chromophores, which selectively and locally transduce this NIR radiation into heat, allow the achievement of minimally invasive laser welding of connective tissues (see e.g. §1 and §2). Most used chromophores are organic dyes, which, in addition to laser welding, are currently employed to support a variety of surgical applications with a history of safety in humans. However they may suffer from severe drawbacks such as an inherently limited efficiency, poor stability and significant diffusivity in the biological environment, and very little chemical flexibility (necessary e.g. to envision strategies based on active targeting and drug delivery), which narrow their range of application.

A possible alternative to organic dyes is given by metal nanopaticles. When these nanostructures are embedded within a dielectric medium, they exhibit very strong localized plasmon resonances. These collective charge oscillations have characteristic frequencies which depend on experimentally accessible parameters, such as the individual and collective geometrical and chemical properties of the nanoparticles and their environment [1]. A special class of nanoparticles is formed by the nonspherical geometries such as nanorods,

which exhibit two absorption bands in their absorption spectrum (**Fig. 4.2**). The transverse absorption band is associated with electron oscillation along the short axis of the particle while the longitudinal band corresponds to the aspect ratio of the rod. The longitudinal absorption band of gold nanorods can be tuned from the visible to the infrared with subtle variations of factors such as their aspect ratio (length / diameter ratio) and overall volume [2], the refractive index of the embedding medium [3], and then on their charge and mutual spatial arrangement [4,5]. For instance, the synthesis of gold nanorods of e.g. ~ 60 nm average length and ~ 15 nm average diameter translates into a strong plasmon resonance at about 800 nm [1]. The excitation of these charge oscillations triggers a variety of valuable and functional processes, which range from the local field enhancement [6], to the Rayleigh scattering [7], to the light absorption and transduction into radiative (luminescence) [8,9] and non radiative (electron-phonon coupling) [10,11] channels. Most of these processes occur with efficiencies unparalleled by competitive organic dyes. As a reference, it is estimated experimentally that it takes less than 100 pM gold nanorods (each nanoparticle seen as an individual molecule) to achieve the same extinction at 810 nm as from 100 μM ICG in aqueous solution [2]. Moreover these nanoparticles are stable in the body [12,13], even at relatively high temperatures and irradiation levels, and may be conjugated with biochemical functionalities, e.g. for delivery purposes [13]. The probable biocompatibility of the gold nanoparticles is another factor which justifies the increasing interest in these new chromophores for biosensing, diagnostic and therapeutic applications [13,14], although this is still a matter of much debate [15,16].

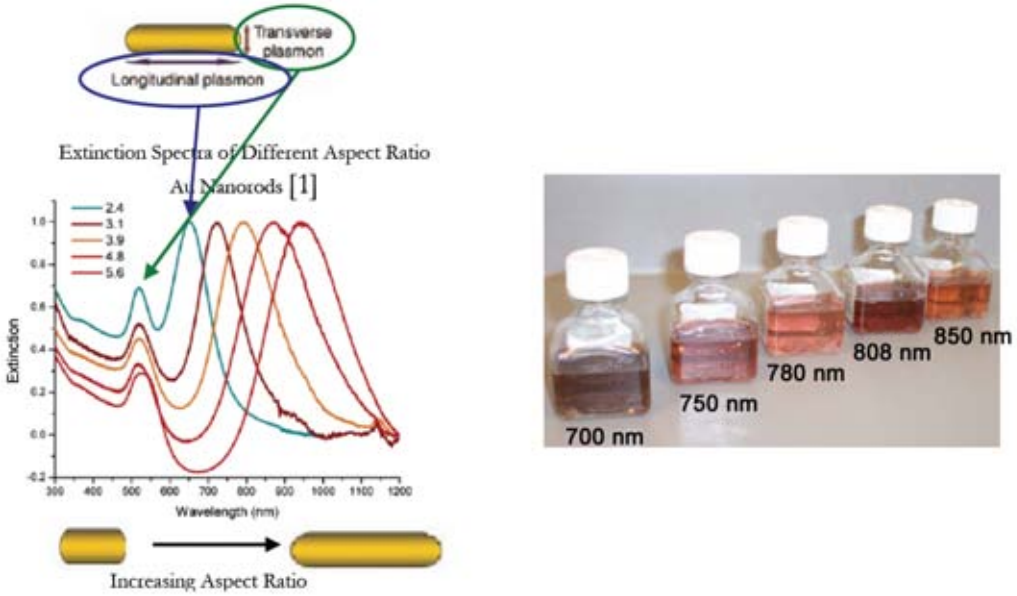


**Fig. 4.2.** (Left )Extinction spectrum of different aspect ratio gold nanorods and (right) their color variance by varying longitudinal plasmon resonance (from www.nanopartz.com).

In the following, the introduction of functional nanoparticles in the laser welding of connective tissues is investigated. The ability to induce conspicuous thermal effects, which lead to the local tissue fusion in porcine lens capsules excised *ex vivo*, from excitation of an interfacial distribution of gold nanorods is proved. This model of connective tissue is chosen on account of several reasons, including its significance in the realm of ophthalmic surgery (e.g. in challenging operations such as lens refilling [17], where the capsule needs to be incised, the lens is replaced with a proper polymer, and then the capsule bag has to be closed again) [18,19], and its remarkable structural cleanness (a transparent and homogeneous tissue with no blood vessels nor cells), which is crucial for the reproducibility of these preliminary tests.

### 4.2.2 Experimental procedure

#### 4.2.2.1 Synthesis of the nanoparticles

*(See Appendix B for details)*

Colloidal gold nanorods were synthesized in a seed-mediated approach derived from the process developed by Nikoobakht et al [20,21]. Briefly, in a first step gold seed nanoparticles were prepared by reduction of gold ions from $HAuCl_4$ with $NaBH_4$ in the presence of the surfactant cetyltrimethylammonium bromide (CTAB). In a second step, an aliquot of these seeds was added as a catalyst to a growth solution of $HAuCl_4$, $AgNO_3$, CTAB and ascorbic acid, which is the reducing agent in this reaction. The relative molarities of all these reagents determine the density and average geometry of the gold nanorods, which in turn governs the optical response of the colloid (in a given medium). The molarities were optimized to achieve densities of the nanoparticles of the order of 100 pM (i.e. some $10^{11}$ nanorods per ml) and aspect ratios of ~ 4, which gives enhanced absorption about 810 nm. These gold nanorods were characterized by transmission electron microscopy and by spectrophotometry.

#### 4.2.2.2 Surgical procedure

The surgical procedure simulates transplants of patches of anterior lens capsules from a donor eye to a recipient eye, assembled in a sandwich configuration. Fifty fresh porcine eyes were acquired at the local abattoir. These samples were kept in a humid environment at 4 °C until the experimental session, within 12 hours post mortem. Prior to the treatment, the eyes were allowed to thermalize at room temperature, and the entire operation was performed at 25 – 30 °C. The preparation of the exogenous chromophore was finalized immediately before the treatment. The gold nanorods were used as-grown and with no additional filtration [22], which is challenging and unnecessary. The suspensions of gold

nanorods initially at ~ 100 pM were concentrated up to ~ 10 nM by centrifugation (5000 g, 30 minutes) and redispersed into aqueous solutions with a minority content of collagen (~ 20 %), used as an excipient. The colloids of gold nanorods were taken from three separate batches, synthesized under nominally identical conditions.

Twenty of the fifty eyes were used for the optimization of the laser welding procedure, ten as donors and ten as recipients. A patch of the anterior capsule was excised from a donor eye lens, and its internal side was stained with a droplet of a colloid of gold nanorods. The droplet was let to dry in air to induce the deposition of the nanoparticles. After 5 – 10 minutes, the patch of capsule was rinsed and re-hydrated with abundant water, which left only a relatively faint rosy stain. Then it was laid with its internal (stained) side onto the external side of the anterior capsule bag of a recipient eye lens, in a sandwich configuration. In doing so, the original orientation of the donor capsule was maintained, thus matching the curvature of the recipient capsule and facilitating the adhesion at their interface. The sandwich was then irradiated by means of contiguous laser spots (no less than twenty per sample) emitted by a 300-μm-core-fiber, whose tip was gently brought into contact with the external side of the donor capsule (contact welding technique) to produce effective tissue fusion. The laser used in this procedure was an 810 nm diode laser (Mod WELD 800, El.En., Florence, Italy) [23]. Laser parameters able to induce functional photothermal effects were pulses with energies of 70 – 100 mJ (corresponding to fluencies of 100 – 140 J/cm$^2$) and durations of about 40 ms. The samples were kept well hydrated throughout the surgery.

#### 4.2.2.3 Characterization of the welded samples

**Resistance to mechanical load**

Preliminary evaluation of the mechanical load resistance of the welded samples was performed as described in the following. We used thirty anterior capsule flaps, out of which ten were cut in patches of 2 × 1 mm$^2$ and twenty in 2 × 2 mm$^2$. The latter were welded together by the procedure described above. The internal side of one stained patch was superimposed onto the external side of one unstained patch, so as to have 1 mm width overlaid. This area was then welded with three contiguous spots. The extremities of these samples were glued onto two glasses (leaving a 0.5 mm gap between the glasses). One end was fixed in a horizontal stand, while the other end was allowed to slide along a horizontal rail, by application of increasing tensile stress. The ultimate load required to tear the sample was recorded. Here we present the average and standard deviation of the ultimate loads from 10 control samples and 10 laser welded samples.

**Microscopical inspection of the treated samples**

*(See Appendix A for details)*

After excision, selected samples were subject to careful observation through a stereomicroscope and a polarization microscope operated with crossed nicols to probe the birefringence of the endogenous collagen network [24]. Others were immediately directed to the histological analysis using standard pathology laboratory procedures. In brief, laser welded specimens were fixed in 2.5 % glutaraldehyde in 0.1 M sodium buffer phosphate (pH 7.4) for 12 hours. These samples were then postfixed with 1 % osmium tetroxide at room temperature and, after sequential dehydration, infiltrated in epoxy resin. Semi-thin sections were attached to glass slides, stained with Toluidine Blue (to enhance the contrast between intact and denatured collagen) and viewed with a light microscope. The spatial extent of notable modifications induced by the laser treatment was recorder and analyzed statistically.

### 4.2.3. Results

**Keynotes on the nanoparticles**

The seed-mediated synthesis of the gold nanorods that was realized leads to aqueous colloids with a bright magenta color. The upper panel of **Fig. 4.3** shows a transmission electron micrograph of these nanoparticles, which reveals an average aspect ratio of ~ 4, with typical diameters in the (10 – 15) nm and lengths in the (40 – 60) nm. These dimensions are significantly larger than the diameters and separations involved in the collagen filaments found in the lens capsule, which are well below 10 nm [25]. The lower panel of **Fig. 4.3** displays the absorption spectrum of a typical (average quality) colloid of the gold nanorods synthesized over the region from the near ultraviolet to the near infrared (in the aqueous environment). Two main resonances are clearly seen as a weaker peak situated at 520 nm and a fairly stronger peak centered at about 810 nm. The origin of these two contributions is well documented in the literature [1,3,26], and relates to different plasmon oscillation modes, i.e. orthogonal and parallel to the long axis of the nanoparticles respectively.

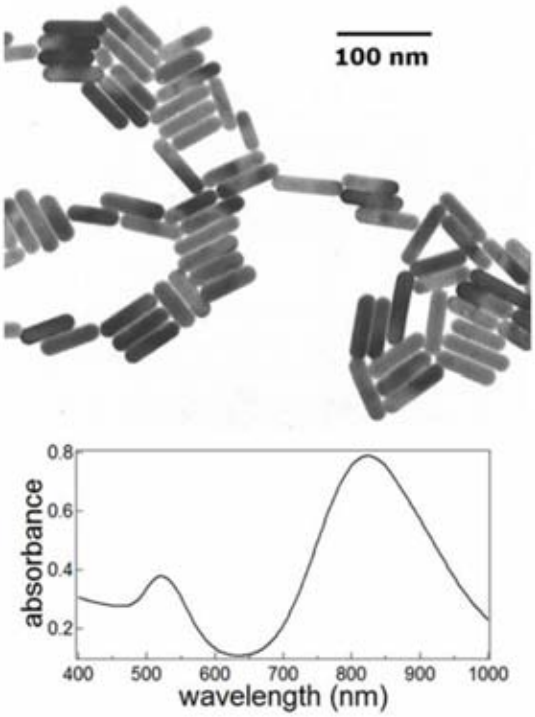


**Fig. 4.3** Transmission electron micrograph and ultraviolet-visible-NIR spectra of the gold nanorods used in the tests.

**Fig. 4.4** shows UV-VIS-NIR spectra of the nanorods, dispersed in the original aqueous solution of the reagents used in the synthesis. In a typical specimen, we present a comparison between one spectrum acquired immediately after growth and one spectrum taken two months later, which is about two to three weeks longer than the timeframe elapsed in the welding experiments below. In this period the nanorods were kept in the original growth solution at variable temperature (about 3 – 4 weeks at room temperature followed by 5 – 6 weeks storage at 4 °C). The spectra in **Fig. 4.4** are displayed at identical optical density about the 520 nm peak, which corresponds to charge oscillations in a transverse plane, common to most kinds of gold nanoparticles. Then the longitudinal plasmon band undergoes an evident blueshift of beyond 20 nm, accompanied by an overall degradation of the absorption properties: a loss of about 40% of the near infrared peak intensity and an increase of the background in the visible range between the transverse and the longitudinal peak of principal interest. Obviously the optimization of the proposed technique will require the utilization of fresher nanorods in the future.

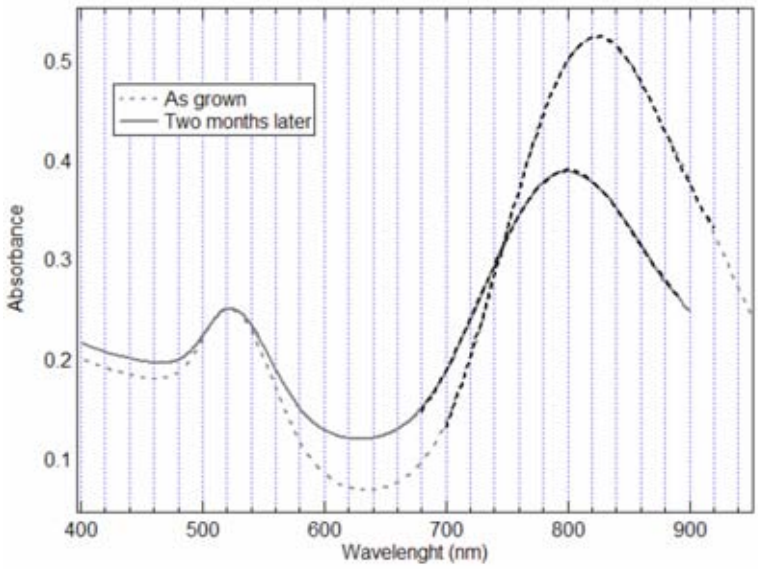


**Fig. 4.4** UV-VIS-NIR spectra of gold nanorod colloids kept in their growth solution. Grey dashed line: from the as-grown sample, i.e. taken about 24 hrs after seeding. Gray continuous line: taken two months later. Black dotted lines: Gaussian fits used to extract quantitative information.

The spectra displayed in **Fig. 4.4** were taken in the original aqueous solution, and may change in a different environment. In an attempt to verify the preservation of the main optical properties of these nanorods once in contact with the connective tissues, we have centrifuged the two months-aged samples and re-dispersed the resultant pellets in a phantom with about the same chemical composition as typical ocular tissues, i.e. 20 % (w/v) collagen in a physiological buffer. The estimated refractive index of this phantom was 1.40 ± 0.05, which compares well with the ~1.38 of typical ocular tissues such as the cornea. Also these measurements were performed about two months after the synthesis, i.e. two to three weeks after the welding tests hereafter had been terminated. **Fig. 4.5** shows the UV-VIS-NIR spectra of these phantoms stained with the nanorods, which is compared with corresponding spectra from the bare phantom without the nanorods and from the original aqueous colloid of the nanorods at the same nanoparticle content (about $10^{-4}$ M atomic gold, which roughly corresponds to about $10^{-8}$ M nanorods according to transmission electron micrographs which reveal typical nanorod dimensions in the 40 nm length × 10 nm width, see **Fig. 4.3**). The main observed feature is a redshift in the longitudinal plasmon band by about 14 nm, which is attributed mainly to an increase of the refractive index in this 20% collagen phantom as compared to the refractive index in the original aqueous solution. It can be speculated that the slight alteration revealed also represents the trend of the gold nanorods once in intimate contact with the lens capsules. Owing to the rather large width of the absorption peaks of the gold nanorods used, one such variation does not pose an actual challenge to their efficiency as NIR photothermal transducers.

When the donor capsules were stained with these nanoparticles, no visible change in the hue of the colloid occurred, which hints at subcritical aggregation of the gold nanorods while drying [5,27]. This behavior is ascribed to the collagen added into the colloid, which effectively exerts valuable protection of the nanoparticles from the outer environment. It can be speculated that a small fraction of collagen inhibits their diffusion, and so hampers their segregation towards the edges of the droplet – as otherwise in a coffee stain [28]–, thus giving a more uniform and functional distribution of the chromophore.

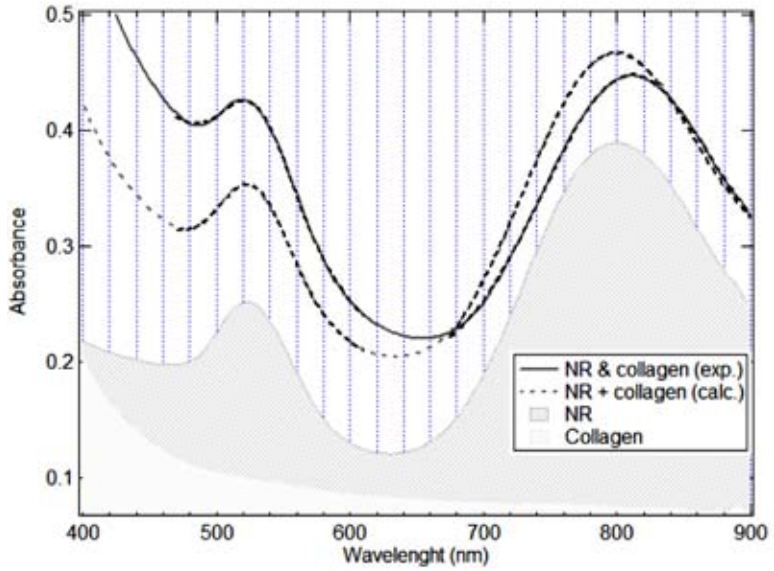


**Fig. 4.5** UV-VIS-NIR spectra of gold nanorod colloids aged two months and dispersed in different environments. Grey continuous line: in a 20% collagen aqueous solution. Grey dashed line: calculated sum of a spectrum from nanorods in their growth solution (light grey shadowed area in the bottom) plus a spectrum from a 20% collagen aqueous solution (grey shadowed area). This grey dashed spectrum is given as a reference. Black dotted bell-shaped lines: Gaussian fits.

**Characterization of the welded samples**

**Mechanical load resistance**

The welding operations carried out simulate transplants in a sandwich assembly, where a patch of anterior capsule of a donor is pasted onto the anterior capsule of a recipient. The interface between these tissues is stained with the chromophore of gold nanorods, and then single spots of laser irradiation are given through an optical fiber (300 μm diameter), as mentioned above. Under these conditions, reproducible welding effects with mechanical strength sufficient to withstand the excision and subsequent manipulation were achieved in the range of 70 – 100 mJ (100 – 140 J/cm$^2$ at the irradiated surface). Besides, it was verified that the range of energies applied is at least half too low to produce any detectible effect in lens capsules with no gold nanorods, which is unsurprising since the anterior lens capsule is essentially completely transparent about 800 nm. The laser welded sandwiches exhibited

resistance to traction (applied with surgical forceps) each time a transplant was simulated. These qualitative observations were substantiated by the tensile stress measurements. The tests revealed that the ultimate load before rupture was (27 ± 3) g for the native tissues (used as a control) and (22 ± 2) g for the laser welded sandwiches, which is highly satisfactory in view of clinical applications.

**Microscopical analysis of the weld sites**

The degree and spatial extent of the photothermal effects were evaluated by microscopic techniques. The upper panels of **Fig. 4.6** display micrographs of a typical sandwich of lens capsules after treatment with 70 mJ and then excision from the recipient eye. The rosy color comes from the residual chromophore stain at the interface. The weld sites appear as a concentric pattern of an inner area ((300 ± 40) μm diameter from ~ 50 weld sites) of uniform opacization, possibly due to the local disorganization of the collagen fibrils, and an outer area (up to (430 ± 40) μm diameter) of altered refractive behavior, which may be associated with a distorted planarity of the capsule surface.

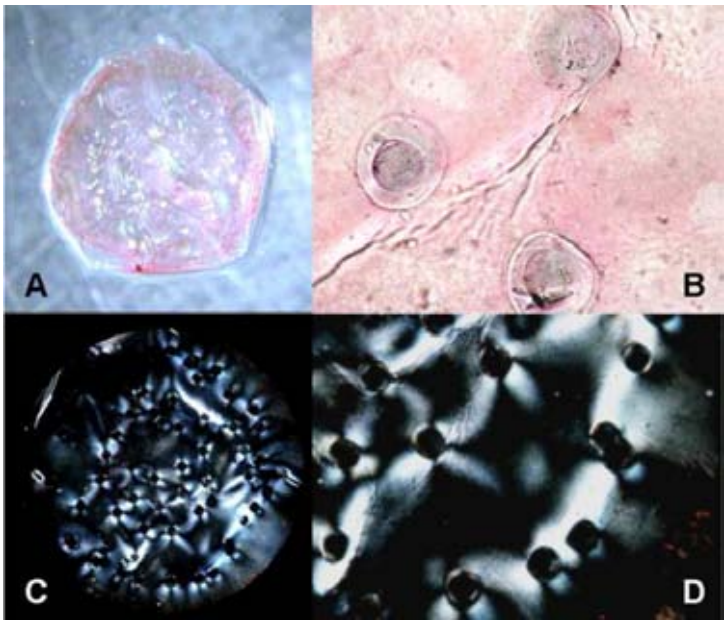


**Fig. 4.6** A and B conventional micrographs, C and D polarisation micrographs from a welded sandwich of anterior lens capsules. A ~ (1.1 × 1.1) $cm^2$; B ~ (0.18 × 0.14) $cm^2$; C ~ (0.7 × 0.7) $cm^2$; D ~ (0.3 × 0.2) $cm^2$.

The weld sites are well revealed in birefringence maps acquired with a polarization microscope operated in transmission with crossed nicols, as shown in the lower panels of **Fig. 4.6**. In these images the birefringence intensity is interpreted as due to the local order of the native collagen filaments. Then the very dark contrast in the weld sites, which extends over an area of (350 ± 50) μm diameter (as estimated from ~ 100 weld sites), may be due to their local denaturation, possibly through the whole thickness of the sandwich of capsules.

These dark spots are separately rimmed by very bright marks, which form a pattern aligned in the two orthogonal polarizations of the microscope. This effect can be understood as the interplay of strain fields radiating from the individual weld sites, possibly due to the shrinkage of the collagen fibrils, which is typically observed to accompany their denaturation [29].

| **Parameter measured** | **Radial distance from the center** | | |
|---|---|---|---|
| | **~ 0 – 150 µm** | **~ 150 – 220 µm** | **> 220 µm** |
| **Transparency and refractive behavior** | Opaque | Transparent; altered refractive behavior | Regular |
| **Birefringence** | Lost | Partially lost | Regular |
| **Molecular structure** | Denatured | Partially denatured | Integer |
| **Thickness (% of normal)** | ~ 50 % | Gradually recovering from 50 % to 100 % | 100 % |

**Table 4.1** Summary of the microscopical analysis

More direct evidence of these processes comes from the microscopical analysis of histological sections stained with Toluidine Blue, as given in **Fig. 4.7** (here irradiated at 90 mJ, i.e. ~ 130 J/cm$^2$). These micrographs clearly prove that the overall adhesion of the sandwich of capsules is well enough to stand all the sequence of steps for the preparation of these histological sections. Indeed the two opposite sides of the interface never display any visible indication of misalignment. The bright blue color all through the thickness of the weld spots comes from the accumulation of the Toluidine Blue, which is induced by the local denaturation of the collagen. This central area extends over a length of (300 ± 20) µm (from ~ 20 weld sites). Also, substantial shrinkage of the tissue along the vertical direction by as much as (53 ± 4) % of the original thickness (from the original ~ 60 µm per layer of anterior lens capsule to a final ~ 30 µm) is very evident. The regular thickness and integrity of the lens capsule becomes gradually recovered with the distance from the weld sites.

Overall the area affected by partial shrinkage and disorganization is evaluated as (410 ± 20) μm. A summary of the principal findings was reported in **Table 4.1**.

### 4.2.4 Discussion

The experimental results reported in the previous section demonstrate that the treatment developed with conspicuous denaturation of the native collagen filaments, at least through the whole thickness of the sandwich of capsules. In some cases, as revealed by the cross section in **Fig. 4.7**, the outer parts of the lens epithelium of the recipient eye were affected as well, which is witnessed by the material left just below the laser spot sites, after the sandwich of lens capsules was peeled off. This suggests that temperatures exceeding 50 °C were reached over a depth of at least ~ 120 μm [31], which is the thickness of a pristine sandwich of porcine lens capsules [30].

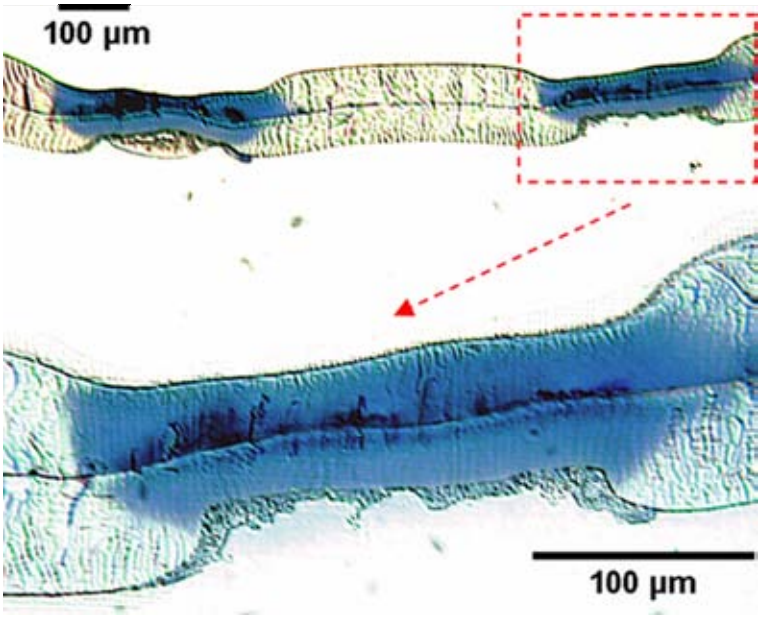


**Fig. 4.7** Histological section of a laser-welded sandwich of anterior lens capsules (Toluidine blue stain). The effects achieved are well reproducible from spot to spot.

The results coherently point to the achievement of a range of temperatures which is quite impressive. It is assumed that – at variance with the organic dyes in use [32] – the overall dimensions of the gold nanorods employed must significantly restrict their perfusion through the endogenous collagen filaments, whose typical separation is much less than the average diameter of the nanoparticles. Then all the heating produced (from samples originally kept at room temperature) originates from genuine heat diffusion from a very interfacial layer stained with the exogenous chromophore, which develops within a 40 ms timeframe.

With an eye to the clinical application, a mechanical load resistance at the weld sites comparable to the one of the native tissues was found, which is fully adequate to support surgeries such as lens refilling. As a downside, it can be noticed that the range of photothermal effects achieved include substantial local alterations of the functionality of the lens capsules. However these alterations are well restricted within ~ 200 – 220 μm from the center of the irradiated area. Since the laser irradiation is intended to be delivered in very peripheral portions of the lens capsule (e.g. to seal a capsulorrhexis), these alterations may not interfere significantly with the vision of the patient. Moreover, based on previous similar experiences [33,34], it is probable that the type of thermal damage observed is reversible in *vivo*, and typically can recover completely within a few weeks after surgery.

The laser energies delivered in these experiments are only slightly above the range in use in very similar surgeries where ICG is the exogenous chromophore (see [33,35,36] and previous §1 and §2). This is very encouraging, also because the effect produced is probably stronger than what may actually be needed in a minimally invasive surgical application. The denaturation of the endogenous collagen filaments is the usual result pursued in operations based on the application of discrete arrays of laser pulses [37]. This effect must take place and develop primarily about the region in immediate proximity of the interface, where the seal is to be accomplished. Further heating well away from the interface is in principle unnecessary (and in fact possibly undesired).

Here it has been demonstrated that the topical application of gold nanorods is suitable to mediate and sustain substantial and functional photothermal processes such as the laser fusion of the collagenous tissues. Significant advantages are expected from the introduction of the gold nanorods in the clinical practice. A better stability and flexibility of storage and manipulation over the competitive organic solutions (whose preparation must typically be done *in situ* during the surgery) may offer novel possibilities to standardize those welding procedures which are still at an experimental stage. A better localization, associated with a lower pore diffusivity through the endogenous fibrils (as due to steric effects), and possibly also by the design of target-specific functionalization procedures [14,38], may enhance the minimally invasive nature of the proposed approach. The possibility to achieve higher temperatures and gradients due to a higher stability and efficiency is expected to prove valuable in the extension of these results towards more complex applications, such as the laser welding of turbid tissues.

### 4.2.5 Conclusions

This preliminary experimental study provides the proof of the capacity of laser-activated gold nanorods to mediate substantial and functional photothermal effects in a model connective tissue (the porcine anterior lens capsule). The irradiated area underwent denaturation in the range of fluencies of 100 – 140 J/cm$^2$, which induced the fusion of patches of lens capsules. The photothermal effects were well localized within ~ 200 – 220 μm from the center of the irradiated area (150 μm in radius), beyond which the tissue appeared completely integer. Overall, gold nanorods were proved to behave as very efficient photothermal transducers, and thus can be suitably employed for laser tissue welding technique. Moreover, they can find application in many other medical methodologies involving the achievement of a photothermal effect.

## References


1 J. Pérez-Juste, I. Pastoriza-Santos, et al.: Coord. Chem. Rev.249, 1870 (2005)
2 P.K. Jain, K.S. Lee, et al.: J. Phys. Chem. B 110, 7238 (2006)
3 M.M. Miller and A.A. Lazarides: J. Phys. Chem. B 109, 21556 (2005)
4 P.K. Jain, S. Eustis S and M.A. El-Sayed: J. Phys.Chem. B 110, 18243 (2006)
5 X. C. Jiang and M.P. PileniMP: Coll. Surf. A, 295, 228 ( 2007)
6 E. Cubukcu, E.A. Kor, et al.: Appl. Phys. Lett. 89, 093120 (2006)
7 C.J. Orendorff, S.C. Baxter, et al.: Nanotechnology 16, 2601 (2005)
8 M.B. Mohamed, V. Volkov, et al.: Chem. Phys. Lett. 317, 517 (2000)
9 H. Wang, T.B. Huff, et al.: Proc. Nat. Acad. Sci. 102, 15752 (2005)
10 C.H. Chou, C.D. Chen and C.R.C. Wang: J. Phys. Chem. B 109, 11135 (2005)
11 M. Eghtedari, A. Oraevsky, et al.: Nano Letters 7, 1914 (2007)
12 T. Niidome, M. Yamagata, et al.: J. Control. Release 114, 343 (2006)
13 V.P. Zharov, E.N. Galitovskaya, et al.: Nanomedicine 1, 326 (2005)
14 M. C. Daniel and D. Astruc: Chem. Rev.104, 293 (2004)
15 N. Lewinski, V. Colvin, and R. Drezek: Small 4, 26 (2008)
16 H. Takahashi, T. Niidome, et al.: Chem. Lett. 35, 500 (2006)
17 E. Haefliger and J.M. Parel: Refract Corneal Surg. 10, 550 (1994)
18 K.M. McNally: Laser tissue welding: In: Vo-Dinh T, ed. Biomedical photonics handbook. CRC Press, Boca Raton; 2003, p. (39)1–(39)45
19 R. Pini, F. Rossi, et al.: Ophthalmic Surg. Lasers Imaging 39, 260 (2008)
20 B. Nikoobakht and M.A. El-Sayed: Chem. Mater. 15, 1957 (2003)
21 N. Tiwari, S. Kalele and S.K. Kulkarni: Plasmonics 2, 231 (2007)
22 K. Park: K. Chapter IV shape and size separation gold nanorods: In: Synthesis, characterization, and self–assembly of size tunable gold nanorods. Atlanta: Georgia Institute of Technology; 2006, 78–106
23 L. Menabuoni, R. Pini, et al.: J. Cataract Refract. Surg. 33, 1608 (2007)
24 S.L. Thomsen, W.F. Cheong and J.A. Pearce: Proc. SPIE 1422, 34 (1991)
25 R.F. Fisher and B.P. Hayes: J. Physiol. 293, 229 (1979)
26 S.A. Kalele, N.R. Tiwari, et al.:J. Nanophoton. 1, 012501 (2007)
27 B.N. Khlebtsov, V.P. Zharov, et al.: Nanotech. 17, 5167 (2006)
28 P. Ball: Nature 389, 788 (1997)
29 S.J. Lin, W. Lo, et al.: J. Biomed. Opt., 11, 03402 (2006)
30 S. Krag and T.T. Andreassen: Exp. Eye Res. 62, 253 (1996)
31 S. Krag, C.C. Danielsen and T.T. Andreassen: Curr. Eye Res. 17, 470 (1998)
32 P. Matteini, F. Rossi, et al.: Proc. SPIE 6426, 642614 (2007)
33 F. Rossi, R. Pini, et al.: J. Biomed. Opt. 10, 02004 (2005)
34 R. Brinkmann, B. Radt, et al.: J. Cataract Refract. Surg. 26, 744 (2000)
35 F. Rossi, R. Pini and L. Menabuoni: J. Biomed. Opt. 12, 014031 (2007)
36 R. Pini, F. Rossi, et al.: Proc. SPIE 6138, 307 (2006)

37 R. Pini, F. Rossi et al.: Laser tissue welding in minimally invasive surgery and microsurgery: In: Pavesi L, Fauchet PM, editors. Biophotonics. Springer Verlag Series inMedical Physics; 2007, p. 269
38 X. Huang, P.K. Jain, et al.: Lasers Med. Sci. 23, 217 (2008)

## 4.3 - PERSPECTIVES

The preliminary results presented in this chapter are encouraging towards the use of gold nanorods in laser welding procedures. We estimate that future applications will take a special advantage of the adaptable functionalization of gold nanopartcles. This may e.g. enable the selective targeting of individual biological structures.

Currently, the replacement of traditional organic molecules with nanostructured chromophores is an inspiring possibility, which is yet far from the clinical application. Forthcoming developments of our investigation of gold nanorods will progressively aim at the exploitation of these nanoparticles in a wider range of laser welding operations, which will raise a number of critical issues and require substantial effort in different directions. These include a detailed study of the cytotoxic behavior of the gold nanorods, and the use of *in vivo* models to investigate questions such as the overall recovery and metabolization dynamics of the nanoparticles.

A primary question regards the replacement of CTAB, which drives the growth of the nanorods, with a less toxic medium. A successful strategy involves the replacement of CTAB with polyethyleneglycol (PEG) after to the synthesis of the nanoparticles. We are currently testing a protocol that can efficiently provide the substitution of CTAB with methoxypoly(ethylene glycol)thiol (mPEG-SH) (see Appendix B for details), where the thiol group favors the substitution of CTAB on the nanorod surfaces due to the greater affinity for gold. Preliminary results are encouraging. A next step will involve the assessment of the substituted nanorods as photothermal transducers in applications of laser welding and the investigation of their cytotoxic behavior in comparison with non-substituted nanoparticles.

# CONCLUSIONS

A substantial improvement in some fundamental and technical questions regarding laser tissue welding, with particular application to ocular tissues, was provided in this thesis. The microscopy analyses we performed on laser-welded cornea samples and the chemical investigations we carried out on the model molecule hyaluronan furnished a clear picture of the matrix reorganization dynamics at the weld site, occurring upon laser irradiation. Therefore, we proposed a model describig the process of corneal welding at the typical operating temperatures reached during clinical applications in ophthalmic surgery, in which proteoglycans were supposed to play a primary role. With regard to the optimization of the laser welding technique, our work was aimed at pursuing two distinct objectives. The first dealt with the assessment of the feasibility of two imaging techniques, namely fluorescence and second-harmonic generation microscopy, to monitor photothermally- and thermally-induced changes in connective tissue. We proved the great potential of both of them to detect the loss of organization in the tissue matrix. The second objective was to test the effectiveness of new nanostructured chromophores, in particular gold nanorods, as photothermal transducers of laser light. The enhanced capability of these nanoparticles to generate consistent photothermal effects during laser welding of lens capsule was tested and demonstrated.

# APPENDIX A

## HISTOCHEMISTRY PROTOCOLS FOR LIGHT AND ELECTRON MICROSCOPY

### Chemicals

Paraformaldehyde, glutaraldehyde (25%), $OsO_4$, Epon 812 resin, 2-dodecenylsuccinicanhydride (DDSA), methylnadicanhydride (NMA), uranyl acetate, lead citrate, Toluidine Blue, Mayer's Hematoxylin, Eosin, Sirius Red F3B and picric acid were used as purchased (Sigma, St. Louis, MO). Copper grids coated with Formvar/carbon films were purchased from TAAB Laboratories Equipment Ltd (Berks, England).

### TRANSMISSION ELECTRON MICROSCOPY

### Buffer

Native buffers present in cellular and extracellular compartments, which maintain a constant pH in the presence of perturbing conditions, are not effective with the fixatives used in electron microcopy. For this reason external buffer solutions are employed to keep the fixative mixture in near isotonic conditions with tissue. Typical "vital" buffers used for biological microscopy include Phosphate Buffer Saline (PBS), Tris, Hepes, Pipes and Cacodylate.

## EXPERIMENTAL PROCEDURE

We used a 0.2 M PBS stock solution (pH 7-7.4) containing 0.15 M NaCl. PBS was the buffer employed for all the experiments of this thesis involving histology analyses.

**Primary fixation**

Primary fixation was performed for stabilizing biological systems with minimal distortion to their morphology and chemical properties. Biological electron microscopy employs two methods for obtaining such results, i.e. chemical or physical fixation. Physical fixation utilizes extremely low temperatures, applied to very small samples, to provide fixation rapidly. However, chemical fixation remains the most common method for specimen preservation. The objective of chemical fixation is to preserve tissue constituents and cells in as close a life-like state as possible and to allow them to undergo further preparative procedures without changes. Fixation arrests autolysis and bacterial decomposition and stabilizes cellular and tissue constituents, so that they can withstand the subsequent stages of tissue processing. Most common reagents used as primary fixatives in electron microscopy are formaldehyde and glutaraldehyde. These aldehydes are thought to form cross-links between proteins, creating a gel which preserves the native organization of tissue constituents.

Formaldehyde is a gas soluble in water to a maximum extent of 37-40 % in weight and it is commercialized under the name of formaldehyde (37-40 %) or formalin (a colorless liquid with 15 % methanol added to inhibit polymerization). It is also obtainable in a stable solid form composed of polymers of high molecular weight, known as paraformaldehyde. Formalin contains many impurities, so formaldehyde for the use in electron microscopy is normally prepared from dissolution, heating and alkalinization of powdered paraformaldehyde. Heated paraformaldehyde generates pure gaseous formaldehyde, which, when dissolved in water, reverts mostly to the monomeric form. Since this solution contains no inhibitors, it has a shelf life of only a few weeks. Aqueous formaldehyde exists principally in the form of its monohydrate, methylene glycol $CH_2(OH)_2$, and as low molecular weight polymeric hydrates or polyoxymethylene glycols. It has been suggested that the hydrated form, methylene glycol, is the reactive component of formaldehyde. Formaldehyde is considered a good choice for fixing cells because it readily passes through the membranes and reacts with intracellular components. However it is almost unsatisfactory in preserving ultrastructural details and, for this reason, is often used in mixtures with glutaraldehyde for electron microscopy.

Glutaraldehyde (or glutaric acid dialdehyde) is a five carbon chain with two aldehyde groups; it is the most widely applied fixative in both scanning and transmission electron

microscopy (TEM). In TEM, buffered glutaraldehyde is recognized as the best fixative to preserve the ultrastructural preservation in a large variety of tissue types. Commercial grade glutaraldehyde is usually a 25 or 50 % aqueous solution with a pH between 3 and 6, containing various impurities such as ethanol, methanol, glutaric acid and various polymers and oxidation products. These products can exert a considerable influence on the fixation process. For this reason high quality distilled glutaraldehyde sealed in glass ampoules under inert gas is recommended for electron microscopy. An aqueous solution of glutaraldehyde is a complex mixture consisting of approximately 4% free aldehyde, 16% monohydrate, 9% dihydrate and 70 % hemiacetal. Free glutaraldehyde may form polymers, or a monohydrate and a dehydrate, which may cyclize to give a hemiacetal which in turn may also polymerize. The wide use of glutaraldehyde as a cross-linking agent is also due to the large range of differential molecules present simultaneously in the fixation solution.

EXPERIMENTAL PROCEDURE

In our experiments, tissues were chemically fixed by immersion either in a mixture of 2 % glutaraldehyde and 2 % paraformaldehyde (modified Karnowsky procedure) or in 2.5 % glutaraldehyde alone in 0.1 M PBS (pH 7.4) for a minimum of 5 hrs at 4 °C. We used the formaldehyde-glutaraldehyde fixative for porcine cornea due to its greater thickness (i.e. about 800-1000 μm) and glutaraldehyde alone for porcine lens capsule (which is only about 60 μm). In fact, formaldehyde penetrates faster than the glutaraldehyde and temporarily stabilizes structures which are subsequently more permanently stabilized in glutaraldehyde, thus well preserving their original morphology. In practice, structures are rapidly stabilized with formaldehyde and then crosslinked with glutaraldehyde. Because of the slow level of penetration of the glutaraldehyde, the specimens were kept at 4 °C in order to better preserve the tissue.

The two fixation procedures followed in our experiments are reported below.

*Modified Karnowsky procedure.* 1 g of paraformaldehyde was dissolved in 21 ml of distilled water, heated at 60-70 °C and stirred. Then 1-3 drops of 1N NaOH were added while stirring until solution cleared. The solution was cooled and 4 ml of 25 % glutaraldehyde were added. The volume was brought to 50 ml with 0.2 M PBS.

*Glutaraldehyde fixation*. 4 ml of 25 % glutaraldehyde plus 16 ml of distilled water were brought to 40 ml with 0.2 M PBS.

All the prefixed corneas and lens capsules were then sliced in 1-2 $mm^3$ samples and then washed two times for 15 min in 0.1 M PBS at 4 °C. The next step was the post fixation.

**Post fixation**

The most commonly employed post fixative is osmium tetroxide ($OsO_4$). It is commercially available as a coarse yellow crystalline material (aqueous solutions are also available) packaged in glass ampoules sealed under inert gas. It presents a limited rate of penetration and for this reason is usually used as a secondary post fixative rather than as a primary one. The electron dense osmium atoms also serve as an electron stain to label the specimen. It mainly reacts with double bonds. For this reason post osmium fixing is essential whether preserving membranes and lipids containing bodies is needed. Osmium tetroxide is also useful for the stabilization of proteins by producing cross-links and protein gels. Due to its extreme toxicity, low vapor pressure and strong oxidation power, precautions are necessary for its handling.

EXPERIMENTAL PROCEDURE

We carried out post fixation of biological tissues by using a 1% $OsO_4$ solution in 0.1 M PBS for 2 h at room temperature. Then we removed the fixative solution and replaced it with 0.1 M PBS.

**Dehydration**

The water within the sample must be removed by bringing the sample through a graded series of either ethanol or acetone. Since the shrinkage problems that often accompany dehydration are more pronounced with sudden changes in the solvent concentration, it is preferable to perform a number of short exposures at gradually increasing concentrations of the solvent. Generally one of two procedures are carried out before infiltration and embedment with epoxy resins. The first one consists in bringing the sample through a graded ethanol series up to 100 %, followed by two changes in 100 % propylene oxide. Propylene oxide (PO) is useful for several reasons. First, most epoxy resins are more soluble in PO then they are in pure ethanol. Second, PO contains a free epoxy radical and thus will not separate from the epoxy resin, even if small amounts are left following infiltration. A drawback is the fact that PO is very effective in extracting lipids from cells, even those previously fixed by osmium tetroxide. Moreover the epoxy group of PO can react with the epoxy group of the resin and inhibit polymerization. This can adversely affect hardness and cutting properties of the block. An alternative dehydration method uses acetone from 30 to 100 %. There is some evidence that acetone causes less specimen shrinkage and lipid extraction than ethanol does. It is also non-reactive with osmium tetroxide and do not interfere with epoxy resin polymerization.

EXPERIMENTAL PROCEDURE

We used acetone for sample dehydration using the procedure reported below.

| | |
|---|---|
| Acetone 30 % | 10 min |
| Acetone 60 % | 10 min |
| Acetone 90 % | 10 min |
| Acetone 100 % 3 changes | 10 min each |

**Infiltration in resin**

Infiltration is the replacement of the solvent with the embedding medium. An optimal embedding medium permits thin sectioning with the least damage during the preparation and gives the least interference during microscopy. It supports and holds together the tissue while remaining non-reactive with the electron beam of the microscope. This means that it should be non-volatile when hit by the beam and non-interfering with the passage of electrons.

The most widely used class of embedding media is the group known as epoxy resins. The term epoxy refers to the epoxy group present in these resins. These resins are substances which are capable of polymerization to form a rigid three-dimensional structure with cross-linking by molecular chains. Once formed, the structure is no more reversible. Epoxy resins have high mechanical strengths, are easily polymerized and produce little shrinkage. Unlike polyesters and methacrylates, which react by means of free radicals groups forming very specific bonds, the epoxy rings react with virtually any available hydrogen. For this reason epoxy resins not only establish cross links with the other resin molecules, but also with the tissue itself and even the containers in which the tissue has been placed. Epoxies usually require large quantities of a second non epoxy molecule, referred to as the “hardener”, with which they may condense. The most used hardener in embedding protocols is 2-dodecenylsuccinicanhydride or DDSA. Another one is methylnadicanhydride (NMA). Sometimes these two are added in different concentrations as to control the relative hardness of the polymerized blocks. In addition to epoxy resin and hardeners, an accelerator may also be employed to self-catalyze the reaction.

Polyester and epoxy resins offer several advantages over methacrylates. The most significant advantage is that they largely prevent from tissue swelling upon polymerization. One disadvantage is that many polyesters and epoxy resins are significantly more viscous than methacrylates, thus their ability to penetrate in the tissue is reduced. This disadvantage can be partially overcome by prolonging infiltration time and/or using other techniques such

as vacuum infiltration. Another disadvantage of using highly viscous media is that the various ingredients do not mix well together, so great care must be taken to insure that the components are completely combined before proceeding with infiltration and embedment. With respect to electron beam stability, epoxy resins are superior to both methacrylates and polyester resins in their ability to resist from damaging under electron radiation. Thus epoxy resins do not lose a significant amount of their mass when exposed to the beam.

Another issue that should be considered when using embedding media is the relative toxicity of the compounds. In general the epoxy resins are the most toxic and carcinogenic of all the embedding media and for this reason should be handled with the utmost care. Some of the more common epoxy resin mixtures include Spurr's resin, Araldite, and Epon 812.

EXPERIMENTAL PROCEDURE

We used Epon 812 as the embedding medium because of its ability to be undamaged by the electron beam during the microscopy observations. In fact, considering that typical operations to look for the weld site in our cornea samples were quite time-consuming, non-epoxy resins could break down and interfere with the measurements.

We first prepared two mixtures, A and B as described in the following table. The mixtures were stirred for about 30 min before use.

| Mixture A | | Mixture B | |
|---|---|---|---|
| Epoxy resin | 5 ml | Epoxy resin | 8 ml |
| DDSA | 8 ml | NMA | 7 ml |

Immediately before their use, the two mixtures were blended (obtaining the final epoxy mixture), and the accelerator [2,4,6-Tris(dimethylaminomethyl)phenol], DPM-30, was added in the proportion of 1.5-2.0 % (about 16 drops).

After the last step of dehydration in acetone 100 %, we embedded the samples first in a 1:1 and then in a 1:2 mixtures of acetone + final epoxy mixture for 30 min. Then the samples were placed at the bottom of pre-dried gelatin capsules and fresh epoxy mixture was added before polymerizing. Resin polymerization was conducted at 45 °C for 12 hrs followed by 24 hrs at 60 °C in a thermostated oven.

**Specimen sectioning**

Conventional microtomes used in the preparation of slides for light microscopy are unsuitable for cutting ultrathin sections required for TEM. To this aim an ultramicrotome is employed. The polymerized block including the embedded tissue is mounted onto a mechanical arm; then this arm is lowered with micrometrical control keeping the block in contact with a stationary knife, composed of a sharpened diamond or a freshly cleaved glass edge.

EXPERIMENTAL PROCEDURE

Particular care was taken to block the samples to the ultramicrotome chuck with the right orientation; then ultrathin slices of 60-90 nm were produced.

**Grids - Support films**

The sections of thin epoxy resins are were placed in the TEM chamber by means of thin metallic support grids. The most common types are known as mesh grids, which are essentially small screens made from thin copper. Mesh sizes are available in sizes ranging from 50 to 1000 μm. Sections picked up on grids of 300 to 400 mesh size are supported by several small strips of metal. Such samples are generally robust enough to withstand TEM examination without the use of further support. However it is often critical that large open areas of the section are not be obscured by the grid bars. In this case it is essential that the grid be coated with some sort of support film on which to place the specimen.

Main requirements for an effective support film are: 1) to be mechanically strong enough to hold the specimen when exposed to the electron beam, 2) to be the most transparent as possible to electrons, 3) absence of irregularities, 4) high signal to noise ratio when compared to the specimen, and 5) easy of preparation should also be considered. To date only a few materials have proved to be satisfactory in meeting these criteria. They are carbon films, graphite oxide, and various plastics. They can be made very thin and are of relatively low atomic weight so as not to interfere with the electron beam. Of the plastics used as support films Collodion (nitrocellulose) and Formvar are the most common; they are both partially hydrophilic. Formvar is a reaction product of polyvinyl alcohol with formaldehye. It is more stable than Collodion and slightly more hydrophilic. All plastic films are subjected to decomposition by the electron beam. They are also prone to further cross-linking by the beam, which adds some strength, but in turn increases brittleness and shrinkage. One major problem due to the induced cross-linking is that the specimen may drift for quite a long time until the film reaches an equilibrium at a given illumination level. Plastic support films can be strengthened and stabilized by depositing a fine layer of carbon

over them. This has the advantage of making the film stronger and more resistant to drift, but has the disadvantage of making the film hydrophobic and more brittle. Plastic support films are usually made by floating off a fine layer of the film onto the surface of clean water. Commercial copper grids coated with plastic films are also available.

## EXPERIMENTAL PROCEDURE

We used 200 mesh copper grids coated with Formvar and carbon film for all our experiments. The sections sliced with the ultramicrotome were mounted on these grids and left to dry overnight on the bottom of a sealed Petri dish, covered with a filter paper. Once sections were firmly attached to the grids (i.e. after drying) they were subjected to staining as discussed in the following.

### Staining

In order to visualize a specimen in the TEM one must have regions of electron transparency and electron opacity. To be of use in a TEM, a stain must have the ability to stop or strongly deflect the electrons of the electron beam, so that they do not contribute to the final image. The most commonly used stains in electron microscopy are made up of heavy metal salts, which have atoms of high atomic weight, effective to deflect the electrons. Electron staining falls into one of two categories 1) positive staining (more common) in which contrast is imparted to the specimen itself and 2) negative staining in which increased electron opacity is produced in the area surrounding the specimen while the specimen itself remains more translucent.

The two most commonly used positive stains are uranyl acetate (MW = 422) and lead citrate (MW = 1054), the two heavy metals being uranium and lead respectively. Both stains are heavy metal salt and are categorized as general or non-specific stains. They are quite toxic and should be prepared and handled with a great care. Uranyl acetate ions are believed to react with phosphate and amino groups (found in nucleic acids and certain proteins) while lead ions are thought to bind to negatively charged molecules. Due to the ability to stain different cellular components uranyl acetate and lead citrate are often used together.

Sections that have been picked up and dried can be stained on their grids with uranyl acetate. The grids are then thoroughly rinsed, dried, and either stained with lead citrate or stored until they are examined in the TEM. Although grids can theoretically be stained any time after sectioning it is preferable to do it within 24 hours after sectioning. Grids that have been exposed to the energy of the electron beam will not absorb any stain. Some resins are particularly difficult to penetrate and therefore do not stain well. In these cases one could try

to either elevate the temperature of the stain or stain the specimens in a methanolic uranyl acetate solution.

Lead citrate is often used to stain grids after they have been stained in uranyl acetate. Being lead citrate very sensitive to $CO_2$ (it quickly reacts to form a precipitate that can destroy the section), effort must be made to eliminate this gas from the staining procedure. For this reason very clean glassware, $CO_2$-free water, and other precautions must be followed in preparing lead citrate for the use. After staining, grids are then blotted dry and stored until needed.

EXPERIMENTAL PROCEDURE

Grids were floated on a drop of 1% uranyl acetate for 30 minutes. The grids were then thoroughly rinsed and dried. Then they were floated on a drop of 0.1 % lead citrate for 3-5 minutes at room temperature. The drops were placed in a $CO_2$-free environment which had been previously prepared using a glass Petri dish in which several sodium hydroxide pellets had been deposited. (The NaOH actively scavenges $CO_2$ and after a few minutes the atmosphere inside the Petri dish is essentially $CO_2$ free.) After staining, the sections were rinsed in a 1M NaOH solution (to wash off the lead citrate) and then thoroughly rinsed in water (to rinse off the NaOH). The grids were finally dried and stored in a Petri until the time of measurements.

## LIGHT MICROSCOPY

### Resin removal

The negligible shrinkage artifacts produced in the specimen by the hardening of resin embedding media used in electron microscopy make them superior embedding materials for light microscopy as well. After sample fixation and embedding (in the same way as depicted above), semi-thin sections (0.5-2 μm) can be obtained by means of an ultramicrotome and than stained using standard histology techniques. A few methods exist for staining epoxy resin-embedded tissue without removal of the plastic from the sections, which never reach anyway the quality of plastic-free sections in terms of contrast and detail resolution. In fact, epoxy resins provide a barrier to dyes, markedly reducing the staining effect. Removal of this type of resin is therefore recommended before staining. Epoxy resins are easily degraded by alcoholic sodium hydroxide or potassium hydroxide, sodium methoxide or bromine vapour.

EXPERIMENTAL PROCEDURE

After cutting with the ultramicrotome, semi-thin sections were transferred to small drops of distilled water on a glass slide. Then the glass was gently heated until sections adhere to it. The glass was placed in a covered Coplin jar containing sodium hydroxide saturated in absolute methanol for 1 h. The slides were completely immersed in the solution. Then they were washed with three changes of absolute methanol, rinsed in 70 % methanol and washed in running tap water for 5 minutes.

**Staining**

Hematoxilyn/Eosin and Toulidine Blue are the most used histochemical stains for light microscopy examination of thermally damaged connective tissue. They are not specific stains for collagen, but can bind preferentially denatured tissue thus providing its identification from the native one. This is due to the opening of new functional sites that follow the breaking-up of the triple helix of collagen.

In unstained sections fibrillar collagen exhibits a weak birefringence, which hinder accurate measurements by optical micrometry. The use of common histological stains such Hematoxylin/Eosin do not improve this picture. On the other hand Sirius Red enhances the natural birefringence of collagen to the extent that histological measurements become possible. The structure of this dye is elongated; thus it is intrinsically anisotropic. When collagen fibrils are stained with Sirius Red in picric acid (also called Picrosirius Red), the dye molecules are bound parallel to the collagen molecules. The birefringence of the regularly-oriented collagen molecules in healthy tissue is thereby significantly enhanced. Staining with Picrosirius Red does not, however, confer birefringence to tissue components randomly oriented at the molecular level, as collagen molecules after thermal denaturation.

EXPERIMENTAL PROCEDURE

We used Hematoxylin/Eosin and Toluidine Blue as unspecific stains of ocular tissue. Picrosirius Red was employed to reveal the structural arrangement of collagen fibrils. In particular, when used in association with polarized light microscopy this dye furnished a specific and sensitive picture of the collagen randomization upon heating. In the following the methodologies employed for preparing and applying the stains are reported.

*Toluidine Blue*

1 part of distilled $H_2O$

1 part of 5 % Toluidine Blue

1 part of 2% sodium borate

These compounds were well mixed, filtered and stored at room temperature.

METHOD

The sections were covered with a drop of staining solution and heated for 1 minute. Then the excess of stain was drained off and the glass was washed in tap water.

*Hematoxylin/Eosin*

METHOD

The sections were covered with a drop of Hematoxylin for 5 minutes and then washed in tap water. A 1 % HCl solution in ethanol 70 % was added and then washed in tap water. The sections were then placed in 1 % Eosin (in distilled water) for 5 minutes and then washed in tap water.

*Picrosirius Red*

Solution A: 0.5 g of Sirius Red F3B were added to a saturated aqueous solution of picric acid (500 mL)

Solution B: 5 mL of acetic acid were added to 1 liter of distilled water.

METHOD

The sections were covered with a drop of Solution A for one hour and then washed in two changes of acidified water (Solution B). Then the excess of water was drained off and the glass was washed in tap water.

# APPENDIX B

## SYNTHESIS OF GOLD NANORODS

### Chemicals

$HAuCl_4 \cdot 3H_2O$ (99.9%), $NaBH_4$ (99%), ascorbic acid (99+%), cetyltrimethylammonium bromide (CTAB) (99%), and $AgNO_3$ (99+%) were used as purchased (Sigma, St Louis, MO). Ultrapure deionized (DI) water was used for all solution preparations and experiments. Glassware was cleaned by soaking in aqua regia and finally washing in DI water.

### Synthesis

Several methods have been described in the literature for the synthesis of gold nanoparticles (AuNPs) of various sizes and shapes. The most popular synthetic method is by chemical reduction of tetrachloroaurate ($HAuCl_4$) using citrate as the reducing agent. This method produces monodisperse spherical AuNPs in the 10-20 nm diameter range. However, production of larger AuNPs (40-120 nm) by this method proceeds in low yields, often resulting in polydisperse particles. An improved method to synthesize monodisperse AuNPs with diameters between 30 and 100 nm using a seeding approach is based on the use of the surface of AuNPs as a catalyst for the reduction of $Au^{3+}$ by hydroxylamine.

Similar seed-mediated methods are also employed to synthesize gold nanorods. These involve the reduction of gold using weak reducing agents onto small

nanospheres of gold as seed, in the presence of shape-directing surfactants usually cetyltrimethylammonium bromide (CTAB). These methods may be distinguished into those that use silver ion assistance in growth solutions and those that not.

Murphy and coworkers (J. Phys. Chem. B 2005, 109, 13857) described a three-step growth protocol, where medium to high aspect ratio nanorods could be synthesized without the use of silver nitrate. Seed particles are generated by reducing gold salt using sodium borohydride in the presence of sodium citrate. The spheres are coated with a layer of negatively charged citrate ions that maintain colloid stability against aggregation by electrostatic repulsion. These spheres seed a growth solution comprising gold salt, CTAB and ascorbic acid in three steps thereby slowing down reduction. The mechanism of nanorods formation by this method is not yet fully understood. Murphy et al. proposed that the polar $CTA^+$ head group of the surfactant binds with greater preference to certain crystallographic faces thereby passivating them to deposition of gold. The other faces, on the other hand, would be exposed for gold to be reduced on, thereby producing anisotropic growth into rods.

The methods using silver nitrate in the growth solutions were proposed by Jana at al. (Adv. Mater. 2001, 13, 1389) but modified by Nikoobakht & El-Sayed (Chem. Mater. 2003, 15, 1957) to achieve spectacular yields of nanorods with excellent monodispersity. Importantly they also showed that changing the quantity of $Ag^+$ ions in the growth solutions allows for fine-tuning of the aspect ratios of the nanorods. The mechanism at work in this protocol has been debated in the recent past. One mechanism postulated CTAB as a soft template which elongates on addition of $Ag^+$ ions which occupy regions between the $CTA^+$ head groups. A second mechanism involves the CTAB passivation concept with additional adsorption of silver bromide on facets slowing down reduction and producing rods shorter than those made without using $Ag^+$. A third mechanism which has appeared recently proposed the underpotential deposition of $Ag^0$ on certain faces, followed by CTAB binding, which serves to stabilize the faces, and allows gold reduction on other faces resulting in rod formation.

EXPERIMENTAL PROCEDURE

*Synthesis*

Gold nanorods were prepared slightly modifying the procedure described by Nikoobakht & El-Sayed (Chem. Mater. 2003, 15, 1957). In a typical procedure, 0.250 mL of an aqueous 0.01 M solution of $HAuCl_4 \cdot 3H_2O$ was added to 7.5 mL of a 0.10 M CTAB solution in a plastic tube. The solutions were gently mixed by inversion. The solution appeared bright brown-yellow in color. Then, 0.600 mL of an aqueous 0.01 M ice-cold $NaBH_4$ solution was added all at once, followed by a rapid inversion mixing for 2 min. The solution developed a pale brown-yellow color. The tube containing the seed solution was kept in a water bath maintained at 25 °C for future use. This seed solution was stable for several days.

The nanorod growth solution was prepared by adding the following reagents to a plastic tube in the following order and then gently mixing: 40 mL of 0.10 M CTAB, 1.7 mL of 10 mM $HAuCl_4 \cdot 3H_2O$, 0.250 mL of 10 mM $AgNO_3$. Next, 0.270 mL of 0.1 M ascorbic acid was added, which changed the solution from brown-yellow to colorless. To initiate nanorod growth, 0.420 mL of the seed solution was added to the growth solution, mixed gently, and left undisturbed at least 3 h.

*Characterization*

Absorption spectra of the solutions were acquired with a spectrophotometer (Jasco V-560, Jasco Europe, Italy). For transmission electron microscopy, nanorod solutions were dried on a copper grid and imaged at 100 kV (Philips CM-12, Philips Industries, The Nederlands). Absorption spectra and TEM images of synthesized nanorods are reported in §4.2.

**Gold Nanorod PEGylation (preliminary tests)**

The use of nanoparticles in most applications relies on the chemical modifications of the nanoparticle surface in order to link the nanoparticle to other biological molecules, substrates or other nanostructures. Because biological ligand-receptor recognition is used in nature to assemble highly complex nanostructures, stable and reliable biofunctionalization of inorganic nanoparticles is a desirable goal both for

biological labeling applications and as a powerful tool for nonbiological nanoparticle assemblies (nanosensors). In a standard functionalization procedure, the first step is to attach to the nanoparticle a stabilizing and protecting layer. Polyethylene glycol (PEG) is used to increase the biocompatibility and biostability of the nanoparticles. In fact, CTAB-capped gold nanorods have poor stability when they are dispersed in buffer solutions due to the aggregating effect of salt ions. Moreover CTAB solution are cytotoxic and may interfere with established protein-linking protocols. By capping the nanoparticle with PEG, the biocompatibility is greatly improved, and nanoparticle aggregation is prevented. PEGylated nanoparticles can readily be made by the conjugation of thiol-functionalized PEG with gold nanoparticles.

## EXPERIMENTAL PROCEDURE

### *Synthesis*

We used the commercially available thiol-terminated methoxypolyethyleneglycol (mPEG-SH) as a stabilizer for nanorods. The PEGylation was performed slightly modifying the procedure described by Liao & Hafner (Chem. Mater. 2005, 17, 4636) as reported in the following.

The raw nanorod solution was centrifuged at 10000 g for 20 min to pellet the nanorods, which were decanted and then resuspended to 1 mL of DI water to reduce the CTAB concentration. One hundred microliters of 2 mM potassium carbonate and 0.2 mL of 5 mM mPEG-SH were added to the nanorod solution. The mixture was stored overnight at room temperature, then was centrifuged, decanted, and resuspended in DI water several times to remove excess CTAB and mPEG-SH.

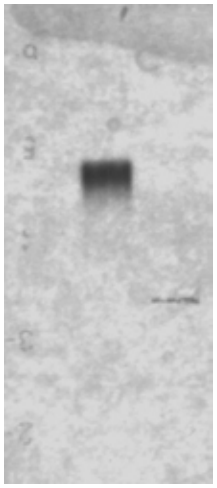

### *Characterization*

Electrophoretic mobility of in a 0.4% agarose gel was performed to characterize functionalized gold nanorods. Gel migration distance after 2h 30 min at 130 V/cm was studied. PEGylated nanorods were well differentiated by electrophoresis as shown on the left (left: PEGylated nanorods; right: CTAB-capped nanorods).

# Publications of the author:

1. *Matteini P, Rossi F, Menabuoni L, Pini R 'Microscopic characterization of collagen modifications induced by low-temperature diode laser welding of corneal tissue' Lasers Surg Med 39 597-604 (2007)*

2. *Rossi F, Matteini P, Bruno I, Nesi P, Pini R 'Monitoring thermally induced phase-transitions in corneal tissue by use of fluorescence micro-imaging analysis' Optic Express 15 11178-11184 (2007)*

3. *Rossi F, Matteini P, Ratto F, Menabuoni L, Lenzetti I, Pini R 'Laser tissue welding in ophthalmic surgery' J Biophotonics 1 331-342 (2008)*

4. *Matteini P, Sbrana F, Tiribilli B, Pini R 'AFM and TEM analyses on low temperature laser welding of the cornea' Lasers Med Sci (accepted) DOI: 10.1007/s10103-008-0617-4*

5. *Ratto F, Matteini P, Rossi F, Menabuoni L, Tiwari N, Kulkarni SK, Pini R 'Photothermal effects in connective tissues mediated by laser-activated gold nanorods' Nanomedicine (accepted) DOI: 10.1016/j.nano.2008.10.002*

6. *Matteini P, Ratto F, Rossi F, Cicchi R, Stringari C, Kapsokalyvas D, Pavone FS, Pini R 'Photothermally-induced disordered patterns of corneal collagen revealed by SHG imaging' Optics Express (accepted)*

7. *Matteini P, Dei L, Volpi N, Goti A, Pini R 'Structural behavior of highly concentrated hyaluronan' Biomacromolecules (submitted)*